NASA Technical Paper 2017

May 1983

Pressures Measured in Flight on the Aft Fuselage and External Nozzle of a Twin-Jet Fighter

Jack Nugent,
Thomas J. Plant,
Robert A. Davis,
and Norman V. Taillon

NASA

25th Anniversary
1958-1983

NASA
Technical
Paper
2017

1983

Pressures Measured in Flight on the Aft Fuselage and External Nozzle of a Twin-Jet Fighter

Jack Nugent,
Thomas J. Plant,
Robert A. Davis,
and Norman V. Taillon
Ames Research Center
Dryden Flight Research Facility
Edwards, California

NASA
National Aeronautics
and Space Administration

**Scientific and Technical
Information Branch**

INTRODUCTION

In recent multimission twin-jet fighter aircraft the propulsion system is highly integrated with the airframe, causing mutual flow interference. Flow interference may contribute to increased local drag in the inlet and nozzle regions and thus reduce overall aircraft performance. Because of flow complexity and configuration dependence, these interference effects are difficult to estimate, and therefore must be obtained from experimental programs.

To improve the technology base for future fighter aircraft and acquire a better understanding of propulsion system/airframe interference, the USAF and NASA are sponsoring an experimental program using the F-15 airplane. The program involves the correlation of wind tunnel and flight pressure measurements. Reference 1 is a preliminary correlation for the inlet/airframe region. References 2 to 4 present preliminary wind tunnel and flight test results for the nozzle/airframe region. This report completes the presentation of the flight test results for the nozzle/airframe region.

Data were obtained in stabilized level and maneuvering flight at Mach numbers from 0.60 to 2.00, with emphasis on Mach numbers from 0.60 to 1.20. Static pressures were measured on the surface of the fuselage and left nozzle, and boundary layer surveys were made on the upper nacelles. These data are presented and analyzed. The analysis was directed toward determining the effects of the propulsion system geometry, the flight variables, and flow interference on the test data.

SYMBOLS

A_J nozzle throat area, cm^2

A_n projected area in the axial direction assigned to a nozzle surface pressure, cm^2

BTL left nozzle boattail angle (fig. 5), deg

BTR right nozzle boattail angle (fig. 5), deg

C_a left nozzle axial force coefficient referenced to wing area, $C_a = \sum_{i=1}^{42} \frac{C_{p_n} A_n}{S_w}$

C_p pressure coefficient, $\frac{p_\ell - p_\infty}{q_\infty}$

C_{p_n} pressure coefficient on nozzle surface

C_p^* pressure coefficient at sonic speed, $\frac{0.7547\left(1 + 0.2M_\infty^2\right)^{3.5} - 1.4286}{M_\infty^2}$

H_p	pressure altitude, geopotential m
h	height measurement above fuselage surface, cm
L	distance from airplane nose to end of tail boom, 19.05 m
L_a	distance from tip of nose boom to aft boundary layer rake station at $X/L = 0.867$, 22.23 m
L_f	distance from tip of nose boom to forward boundary layer rake station at $X/L = 0.684$, 18.75 m
M_ℓ	Mach number within the boundary layer for either rake
M_{ref}	reference Mach number used in boundary layer calculations for either rake
M_δ	Mach number at edge of boundary layer for either rake
M_∞	free-stream Mach number
MIL	military power engine setting; nozzle is closed and nominal boattail angle is 18.1°
NPRL	nozzle pressure ratio for left engine, nozzle entrance pressure divided by p_∞
PCM	pulse code modulation
PTRAT	pitot pressure ratio in the boundary layer
p_i	pitot pressure measured within the boundary layer, forward or aft rake, N/cm^2
p_ℓ	local surface static pressure, N/cm^2
p_{ℓ_a}	local surface static pressure, aft rake, N/cm^2
p_{ℓ_f}	local surface static pressure, forward rake, N/cm^2
$p_{\ell_{rk}}$	surface static pressure at boundary layer rake station, N/cm^2
p_∞	free-stream static pressure, N/cm^2
p_{t_∞}	free-stream total pressure, N/cm^2
q_∞	free-stream dynamic pressure, N/cm^2

R_L	Reynolds number based on length L
R_{L_a}	Reynolds number based on length L_a
R_{L_f}	Reynolds number based on length L_f
r	local radius of curvature at boundary layer rake station, cm
S_w	wing reference area, 55.839 m^2
T_{t_∞}	free-stream total temperature, K
U_e	velocity at edge of boundary layer for either rake, m/sec
U_ℓ	local velocity within the boundary layer for either rake, m/sec
U_{ref}	reference velocity for the boundary layer for either rake, m/sec
$\frac{U}{U_e}$	velocity ratio in the boundary layer for either rake
X	distance from airplane nose, m
X/L	nondimensional distance from airplane nose
α	angle of attack, deg
β	angle of sideslip, deg
δ^*	boundary layer displacement thickness, cm
δ_a	boundary layer thickness at aft rake, cm
δ_f	boundary layer thickness at forward rake, cm
θ	boundary layer momentum thickness, cm
ρ	left inlet cowl angle, deg
φ	circumferential angle around nozzle measured clockwise from top of aircraft when viewed from the rear, deg

Subscripts:

a	aft
f	forward

DESCRIPTION OF AIRPLANE AND PROPULSION SYSTEM

The F-15 airplane (fig. 1) is a high performance fighter with a mission requirement for dash capabilities exceeding Mach 2. An additional mission requirement is the ability to cruise efficiently at transonic speeds. Distinguishing airplane features are a high-mounted sweptback wing, twin vertical stabilizers, and a large horizontal stabilator (fig. 2). The variable geometry inlets use horizontal ramps mounted at wing level (fig. 3(a)). The variable cowl angle and two-position bypass door are shown in figure 3(b). The variable geometry surfaces are positioned by an air-inlet controller. The test airplane is also equipped with a manual control to allow the pilot to make in-flight changes to the cowl and bypass door positions. Additional details on the inlet are given in reference 1.

The powerplants are two prototype Pratt & Whitney F100-PW-100 engines which are twin-spool afterburning turbofans in the 110,000-newton thrust class. Both the fan and the compressor are variable geometry for high performance and distortion attenuation. The nominal bypass ratio is about 0.7 for military (maximum nonaugmented) power at sea level standard day conditions. The engine controls consist of a hydromechanical unit and a supervisory digital control unit.

The afterbody configuration consists of closely spaced nozzles and widely spaced tail support booms (fig. 4). The development of this configuration is discussed in reference 5. The exhaust nozzles are variable geometry, have a convergent-divergent internal flow path, and are scheduled by the engine control to continuously provide the proper ratio between throat area and the ratio of exit area to throat area. The nozzle surfaces consist of variable position flaps, which slide in a circumferential direction to maintain a circular gas path at the throat and exit as the geometry is varied.

Details of the external nozzle geometry are shown in figure 5. The three-dimensional fuselage surface ends at $X/L = 0.886$. Aft of this station the exposed nozzle is axisymmetric. The nozzle is fixed geometry forward of $X/L = 0.900$, where the terminal angle is 13.2°. The nozzle geometry is variable downstream of $X/L = 0.900$. There is a discrete change in nozzle shape at the juncture of the fixed and variable components of the nozzle. The boattail angle varies from about 18.1° at military power to about 2° with full afterburning. In determining the boattail angle the variable flap surfaces are assumed to be straight lines so that the boattail angle is constant over the length of the variable part of the nozzle. The nozzle boattail angle changes with the pilot's throttle setting through the engine control. A wedge-shaped nozzle interfairing is located between the left and right nozzles (fig. 4). The wedge has a 20° included angle and terminates at the exit plane of the nozzles.

Vent air from the engine compartment was discharged upstream of the nozzle through an annular gap formed by segmented flexible fairings (fig. 6). The effect of this leakage flow on the nozzle pressures was determined during the flight tests.

INSTRUMENTATION

Pressure

Figures 7(a) and 7(b) show the locations of the 38 fuselage static pressure orifices and the two boundary layer rakes. A static pressure orifice was located on the fuselage surface immediately forward of each rake (figs. 7(a) and 8(a)). Each rake had 10 pitot tubes; the topmost tube was 38.43 centimeters from the fuselage surface.

The fuselage centerline and the left nacelle were the most heavily instrumented with static pressure orifices. One of the orifices on the lower left nacelle centerline (fig. 7(b)) was close to the left fuel dump vent (fig. 8(b)).

In addition to the instrumentation on the fuselage, 42 static pressure orifices were distributed over the external surface of the left nozzle. Figure 9 shows a rear view of the nozzle and the angular locations of these orifices. Except for the orifice row at 134°, the most upstream orifice in each row was located on the fixed part of the nozzle, and the other orifices were on the variable part of the nozzle. For the orifice row at 134°, all orifices were on the variable part of the nozzle. Table 1 shows the X/L locations for the nozzle orifices. These X/L values are the average values for the several boattail angles tested. The right nozzle was not instrumented.

The static and pitot pressures were measured with differential pressure transducers that were connected by tubing to each orifice or pitot tube. The reference pressure for each transducer was one of three reference pressures which were measured by absolute pressure transducers. All transducers were kept in environmentally controlled bays.

The transducers used for the fuselage and boundary layer pressures had ranges of either ± 2.8 N/cm^2 or ± 4.1 N/cm^2. The connecting tubing to the pressure source had an inside diameter of ± 0.318 centimeter and lengths ranging from 1.8 meters to 9.1 meters. For the nozzle, almost all of the transducers had ranges of ± 1.4 N/cm^2. The remainder had ranges of ± 2.8 N/cm^2. From the nozzle orifices the connecting tubing had an inside diameter of 0.110 centimeter and a length of 3.66 meters. This was followed by a shorter length of 0.318-centimeter tubing leading to the transducer.

Additional Instrumentation and Recording

Air data pressure parameters, angle of attack, angle of sideslip, and free-stream total temperature were sensed on a nose boom. Nose boom pitot pressure and static pressure were used to calculate p_∞, p_{t_∞}, M_∞, and q_∞. An in-flight airspeed calibration yielded corrections for position error. Vanes measured angle of attack and angle of sideslip, and a pair of shielded thermocouple temperature probes measured free-stream total temperature. Angle of attack was corrected for upwash, boom bending, and pitching velocity.

The deflections of the horizontal stabilator and rudders were measured, as were the inlet cowl and bypass door positions. Engine power settings, rotor speeds, and nozzle throat and exit areas were also measured. These were obtained from engine-mounted instrumentation supplied with the engine.

The analog electrical signals from the several airplane and engine sensors were conditioned and digitized by an onboard pulse code modulation (PCM) system with 8-bit resolution. To increase the resolution for the air data sensors and the reference pressure transducers, the incoming sensor signals were divided into high and low levels and recorded on two 8-bit PCM words. The measured flight data were recorded on an onboard magnetic tape and a ground magnetic tape via telemetry. Some of the telemetered data were also displayed in the ground control room to aid in conducting the flight tests.

TEST PROCEDURES

For each maneuver, it was necessary to simultaneously stabilize Mach number, altitude, angle of attack, and angle of sideslip before data were acquired. To aid the pilot in obtaining steady data during the windup turn and pushover-pullup maneuvers, standard cockpit instrumentation was supplemented with the trajectory guidance system discussed in reference 6. The system used the null technique between the desired and current test conditions on a special cockpit display. The results were satisfactory.

The Mach numbers tested ranged from 0.60 to 2.00. Three test altitudes, nominally 6100, 10,700, and 13,700 meters, were used to obtain a Reynolds number variation. The angle of attack range extended from about 0° to about 7°, and for most tests angle of sideslip was kept within ±0.5° of 0°. Several maneuvers were flown to find the effect of angle of sideslip on the pressure data.

The test Reynolds number range is shown plotted against Mach number in figure 10 for the nominal test altitudes. It extended from about 70×10^6 to about 290×10^6. Average stabilator position varied from 2.1° leading edge up to 3.2° leading edge down, and the average rudder trailing edge position varied from 2.5° trailing edge left to 1.4° trailing edge right.

The left nozzle boattail angle was determined in real time during each flight as follows. Before the test program the relationship between boattail angle and nozzle throat area was established from a ground calibration. During each flight the boattail angle was calculated by downlinking, via radio telemetry, the measured nozzle throat area from the airplane to a ground computer. The boattail angle was calculated and then uplinked via radio telemetry to the airplane and displayed on the pilot's cockpit console.

For the right engine a similar technique was used. For each test point the pilot set the left boattail angle, which had the test instrumentation, by adjusting the throttle; the pilot adjusted the right engine power setting, and thus its boattail angle, at the appropriate level to stabilize test conditions. Therefore, for some of the test points there was a mismatch between the nozzle geometry and jet exhaust temperatures of the left and right engines.

Some of the left nozzle boattail angles tested in flight are plotted against Mach number in figure 11. The four target values, which are identified by the horizontal lines, are MIL, 14.6°, 9.5°, and 7.7°. The last three values are afterburning conditions. The MIL and 14.6° values were tested throughout the entire Mach number range, but the 9.5° and 7.7° values were tested over only a portion of the Mach number range. The data indicate that in afterburning the pilot was able to set the boattail angles within ±0.5° of the target values most of the time.

The boattail angle setting designated MIL is a nonafterburning setting and is nominally 18.1°. The pilot was unable to maintain this value for the entire Mach number test range. The variation about 18.1° up to about $M_\infty = 1.40$ was about ±0.5°. Above $M_\infty = 1.40$, the engine control (that is, the military power lockup feature) would not permit the pilot to make throttle commands below military power. Therefore, the boattail angle showed a steady decrease from 18.1° to about 16° at $M_\infty = 2.00$. The variation of boattail angle about the target values for all power settings agrees with the errors estimated in the UNCERTAINTY section.

Nozzle pressure ratio is a test variable commonly varied in nozzle/afterbody investigations in the wind tunnel but could not be easily varied for systematic investigation in this study. It was generally fixed by the test conditions. Figure 12 shows the variation of nozzle pressure ratio for the left engine, NPRL, with M_∞ for a number of test conditions. The data represent several boattail angles and the three nominal test altitudes. For all of the afterburning cases and supersonic military power cases NPRL was a function of M_∞ only. For the subsonic military power conditions there was some NPRL variation. For the range of tests shown in figure 12, nozzle throat area ranged from 0.268 square meter to 0.420 square meter, and the ratio of exit area to throat area ranged from 1.06 to 1.42. Since the right-hand engine was used to stabilize on the test point, in some cases the nozzle pressure ratio for the right engine did not match that for the left engine.

Other variables tested were left inlet cowl angle and bypass door position, which were set manually in flight before each test. For most tests the left inlet cowl angle was set in the 0° position and the bypass door was set closed. The right inlet cowl angle and bypass door were in the automatic control mode, subjecting the upper fuselage flow field to slight geometric asymmetry. For some tests, however, the left inlet cowl angle was set at other angles, and the bypass door was set open to find any possible effects of these parameters on the fuselage, nozzle, and boundary layer pressures. Further, one-half of the annular gap formed by the segmented flexible fairings was sealed to determine any effects on the nozzle pressures. Figure 13 shows how this was done for the upper half. For other tests, the bottom half was sealed using a similar technique.

DATA REDUCTION AND ANALYSIS

Telemetered data were conditioned after each flight and reduced to engineering units. In this procedure, pre- and postflight zeros were applied to the calibrations for each measured quantity. The parameters analyzed were calculated as follows.

Surface Pressures

The surface static pressures are presented as pressure coefficients, C_p, where

$$C_p = \frac{p_\ell - p_\infty}{q_\infty} \tag{1}$$

Data were obtained over time intervals ranging from 1 to 5 seconds or more, and were averaged over the time interval. To determine the nozzle axial force, each of the 42 orifices was assigned an aft-facing projected area, which varied with nozzle boattail angle. The axial force was the summation of the pressure coefficient-area products and was divided by the wing area to yield an axial force coefficient, C_a:

$$C_a = \sum_{i=1}^{42} \frac{C_{p_n} A_n}{S_w} \tag{2}$$

Boundary Layer Parameters

The boundary layer pitot pressures, p_i, and the appropriate forward or aft rake surface static pressure, p_{ℓ_f} or p_{ℓ_a}, were used to calculate the following boundary layer parameters by adapting the equations in reference 7. The equations are written for the forward rake; similar equations apply for the aft rake.

Local Mach number, M_ℓ, was calculated for subsonic flow by the equation

$$M_{\ell_f} = \sqrt{\left[\left(\frac{p_i}{p_{\ell_f}}\right)^{0.2857} - 1\right]5} \tag{3}$$

and for supersonic flow by the equation

$$M_{\ell_f} = \frac{\left(\frac{p_i}{p_{\ell_f}}\right)^{0.5}}{12.92}\left(7 - \frac{1}{M_{\ell_f}^{0.5}}\right)^{1.25} \tag{4}$$

The criterion for supersonic flow was $\frac{p_i}{p_{\ell_f}} > 1.8929$. Equation (4) was solved iteratively.

A reference Mach number, M_{ref}, was calculated for the forward rake using p_{t_∞} and p_{ℓ_f} for subsonic flow by the equation

$$M_{\text{ref}_f} = \sqrt{\left[\left(\frac{p_{t_\infty}}{p_{\ell_f}}\right)^{0.2857} - 1\right]5} \tag{5}$$

and for supersonic flow by the equation

$$M_{\text{ref}_f} = \frac{\left(\frac{p_{t_\infty}}{p_{\ell_f}}\right)^{0.5}}{12.92}\left(7 - \frac{1}{M_{\text{ref}_f}^{0.5}}\right)^{1.25} \tag{6}$$

The velocity ratio through the boundary layer was calculated by the equation

$$\frac{U_{\ell_f}}{U_{\mathrm{ref}_f}} = \frac{M_{\ell_f}}{M_{\mathrm{ref}_f}} \left(\frac{5 + M_{\mathrm{ref}_f}^2}{5 + M_{\ell_f}^2} \right)^{0.5} \tag{7}$$

The reference velocity U_{ref_f} was calculated in meters per second for the forward rake by the equation

$$U_{\mathrm{ref}_f} = 20.05 \sqrt{\frac{T_{t_\infty}}{1 + 0.2M_{\mathrm{ref}_f}^2}}\, M_{\mathrm{ref}_f} \tag{8}$$

In order to determine the boundary layer thickness at the forward rake, δ_f, $\frac{U_{\ell_f}}{U_{\mathrm{ref}_f}}$ was plotted against the height above the fuselage surface, h. In some cases the velocity ratio reached a maximum at an intermediate value of h. As h increased further, the ratio decreased, indicating that the boundary layer height was exceeded. Therefore, δ_f had to be selected close to the maximum value of $\frac{U_{\ell_f}}{U_{\mathrm{ref}_f}}$. The value selected for δ_f was the value of h at the point where $\frac{U_{\ell_f}}{U_{\mathrm{ref}_f}}$ was equal to 0.995 of the maximum value of $\frac{U_{\ell_f}}{U_{\mathrm{ref}_f}}$ reached in the profile before the profile decreased.

The measured boundary layer thickness was compared to an incompressible flat plate value (ref. 8) given by the equation

$$\delta_f = \frac{0.0598}{\log R_{L_f} - 3.170} L_f \tag{9}$$

The Mach number at the edge of the boundary layer, M_{δ_f}, was obtained from a plot of M_{ℓ_f} as a function of h. The velocity at the edge of the boundary layer, U_e, was given by the equation

$$U_e = 20.05 \sqrt{\frac{T_{t_\infty}}{1 + 0.2M_{\delta_f}^2}}\, M_{\delta_f} \tag{10}$$

Velocity ratio profiles are presented as $\frac{U}{U_e}$ plotted against h. $\frac{U}{U_e}$ was obtained by the equation

$$\frac{U}{U_e} = \frac{U_{\ell_f}}{U_{\text{ref}_f}} \left(\frac{U_{\text{ref}_f}}{U_e} \right) \tag{11}$$

Displacement thickness δ^*_f and momentum thickness θ_f were calculated by adapting the equations of reference 9 as follows:

$$\delta^*_f = \int_0^{\delta_f} \left[1 - \frac{M_{\ell_f}}{M_{\delta_f}} \left(\frac{5 + M_{\ell_f}^2}{5 + M_{\delta_f}^2} \right) \right] \frac{r + h}{r} dh \tag{12}$$

$$\theta_f = \int_0^{\delta_f} \frac{M_{\ell_f}}{M_{\delta_f}} \left(\frac{5 + M_{\ell_f}^2}{5 + M_{\delta_f}^2} - \frac{M_{\ell_f}}{M_{\delta_f}} \right) \frac{r + h}{r} dh \tag{13}$$

For the forward boundary layer rake the factor $\frac{r + h}{r}$ was set equal to unity, since the upper surface of the airplane roughly resembled a flat plate. For the aft boundary layer rake the factor $\frac{r + h}{r}$ was greater than unity, since the boundary layer height was not small compared to the nacelle's radius of curvature.

The variation of pitot pressure in the boundary layer, p_i, was also of interest. These pressures were normalized by free-stream total pressure, p_{t_∞}, and the resulting ratio was called PTRAT:

$$\text{PTRAT} = \frac{p_i}{p_{t_\infty}} \tag{14}$$

Nozzle Pressure Ratio

The appropriate engine manufacturer's program to calculate F100-PW-100 engine parameters was used to obtain nozzle entrance pressure, the ratio of specific heats, and other engine parameters. The desired quantities were obtained as a function of Mach number, pressure altitude, and engine power setting. Left engine nozzle pressure ratio, NPRL, was calculated by using the nozzle entrance pressure from the engine program and the calculated value of p_∞ obtained from the nose boom measurements.

For some of the data at Mach numbers of 0.60, 0.80, 0.90, and 1.20, nozzle exit pressure was calculated by using the nozzle entrance presssure, the ratio of specific heats,

and the measured values of nozzle throat and exit areas. Isentropic flow was assumed. The nozzle exit pressure was compared to free-stream static pressure, p_∞. The comparisons showed that the nozzle exit pressure was generally within ± 0.7 N/cm^2 of p_∞, indicating operation near the design pressure ratio.

UNCERTAINTY

The estimated uncertainties for some of the measured and calculated quantities presented in this investigation are listed as follows.

Parameter	Uncertainties
M_∞—	
Subsonic	±0.006
Supersonic	±0.012
p_∞, N/cm^2—	
At $M_\infty = 0.90$, $h_p = 6630$ m	±0.059
At $M_\infty = 1.40$, $h_p = 10{,}700$ m	±0.084
q_∞, N/cm^2—	
At $M_\infty = 0.90$, $h_p = 6630$ m	±0.035
At $M_\infty = 1.40$, $h_p = 10{,}700$ m	±0.001
p_ℓ, N/cm^2	±0.025
p_i, N/cm^2	±0.031
α, deg	±0.25
β, deg	±0.25
BTL, deg—	
At BTL = 18.4°	±0.43
At BTL = 9.5°	±0.25
A_n, percent—	
At BTL = 18.4°	±1.4
At BTL = 9.5°	±1.6
A_J, cm^2	±52

The uncertainties listed include contributing uncertainties in instrumentation, encoding, and calculation. Where appropriate, the contributing uncertainties were combined using the root-sum-square method to obtain the uncertainty listed. Uncertainties in M_∞, p_∞, and q_∞ include position error uncertainties determined in flight using the tower flyby and radar tracking methods.

To obtain uncertainties in C_p and C_a, the perturbation method was used for the flight test conditions shown in table 2. These conditions cover a wide range of test conditions.

The uncertainty in C_p was obtained for one of the 42 nozzle orifices, and the uncertainty in C_a was obtained using equation (2). These quantities are plotted against q_∞ in figure 14. Both uncertainties show a strong dependence on q_∞. The highest uncertainty occurs at low q_∞, which corresponds to low M_∞ at the higher altitudes. Conversely, the lowest uncertainty occurs at high q_∞, which corresponds to flight at high M_∞ at the lower altitudes. For the latter conditions, the uncertainty in C_p approaches 0.01, while the uncertainty in C_a is less than 0.0001.

RESULTS AND DISCUSSION

The following discussion concerns the fuselage pressures, boundary layer profiles, boundary layer thickness, nozzle pressures, and nozzle axial force. The fuselage and nozzle pressure data and the nozzle axial force data were obtained with the boundary layer rakes removed. Where possible, the effects of the propulsion system variables, flight variables, and flow interference were separated, and it became clear which variables had the greatest effects on the data.

Aft Fuselage Pressures

Except as stated otherwise, the fuselage pressure data were obtained with the cowl angle set at 0° and the bypass door closed. The effect of altitude variation on these data was negligible, so data acquired at different altitudes are occasionally presented together.

The fuselage pressure data were used to identify the nature of the flow fields (compression or expansion) over the fuselage. Figure 15 shows these flow fields as well as the vehicle components that influenced the pressure data. For the upper fuselage region (fig. 15(a)), the expansion field is influenced by the forward portion of the wing. The compression field immediately downstream of this region for both the upper and the lower fuselage (fig. 15(b)) is influenced primarily by the contour change due to the engine nacelles and possibly also by wing shock waves. Farther downstream, in the nozzle/afterbody region, the flow field becomes the most complex and generally shows either an expansion-recompression or an expansion field. The presence of the vertical tail, boattailing due to the fuselage and nozzle interfairing, and variable nozzle geometry all combine to influence the flow in this region.

These flow fields are apparent in figure 16, where data are shown for $M_\infty = 0.90$ and $\alpha \approx 2°$ for a test altitude of 10,600 meters. For the upper fuselage centerline, the expansion due to the wing and compression due to the nacelle, followed by expansion-compression to near ambient pressure, are clearly shown. The upper left nacelle centerline data are similar downstream of $X/L = 0.53$ except that the data show steeper negative slopes, possibly because of the closeness of the expansion field of the vertical tail. The lower fuselage centerline data show expansion due to boattailing. No compression is shown for the aftmost pressures. Downstream of $X/L = 0.7$ the lower left nacelle centerline data are similar to the data for the upper left nacelle but with a smaller slope. The upper left tail boom pressures, which are closest to the tail, show a strong expansion to a very low pressure followed by a rapid compression to near ambient pressure for the aftmost orifice.

The rapid compression may be shock induced, since the reference C_p* value indicates that sonic flow was exceeded.

Effect of left nozzle boattail angle.—Figures 17(a) to 17(c) show the effects of changes in left nozzle boattail angle, BTL, on fuselage C_p at M_∞ = 0.61, 0.90, and 1.20, respectively, at 10,600 meters and 10,700 meters for several test angles of attack. At M_∞ = 0.61 (fig. 17(a)), decreasing BTL from 18.1° to 12.3° increases the aftmost pressure coefficients at the upper fuselage, lower fuselage, and lower left nacelle centerlines. At $M_\infty \approx 0.90$ (fig. 17(b)), decreasing BTL from 18.1° to 10.5° increases the aftmost pressure coefficients at all fuselage regions. The increase appears to be propagated upstream for all regions except for the upper left nacelle centerline. At $M_\infty \approx 1.20$ (fig. 17(c)), decreasing BTL from 18.1° to 9.3° increases the aftmost pressure coefficients at the upper and lower fuselage centerlines and the upper left tail boom.

Effect of right nozzle boattail angle.—During some of the tests it was necessary to vary the right nozzle boattail angle, BTR, to sustain the stabilized test point. These variations caused changes in the fuselage pressures similar to the changes caused by variations of the left nozzle boattail angle. Figure 18 illustrates the effects of decreasing BTR from 13.7° to 6.6° on fuselage C_p at M_∞ = 0.88 at 6200 meters and $\alpha \approx 6°$. The most notable effects are increases in the aftmost pressure coefficient for the upper fuselage centerline and in the distribution for the upper left tail boom.

Effect of Mach number.—Figures 19(a) to 19(e) show the effects on fuselage C_p of a Mach number variation from M_∞ = 0.64 to M_∞ = 2.00 with α nominally at 1° at test altitudes of 10,600 meters and 13,900 meters. On the upper fuselage centerline (fig. 19(a)) increasing M_∞ from 0.64 to 0.90 produces a slight reduction in the mid- and aft fuselage C_p values. The data at M_∞ = 0.90 show that sonic speed is reached, since the test data decrease below C_p*, while the data for both Mach numbers show that compression due to boattailing at the aft end reaches near atmospheric pressure. Further increase in M_∞ to 0.96 and 1.05 causes a sharp reduction in C_p level in the mid- and afterbody regions. The sudden increase and decrease in C_p aft of X/L = 0.8 for M_∞ = 1.05 is thought to be caused by a shock-expansion process due to a shock wave generated by the leading edge of the vertical tail. At M_∞ = 1.20 and 1.40, the data show the steepest profile gradients, but a stabilization of the aftmost C_p values at about -0.2. At M_∞ = 1.60 and 2.00, the mid- and aft fuselage gradients diminish, and the aftmost C_p values increase to about -0.1.

On the lower fuselage centerline (fig. 19(b)), Mach number dependence is most evident for data downstream of X/L = 0.8 up to a Mach number of 1.05. Positive values of C_p at the aft end of the fuselage due to boattailing exist only for M_∞ = 0.64; C_p decreases sharply as M_∞ increases above that value. The aftmost level of C_p approaches -1.0 at M_∞ = 1.20 and 1.40. There is evidence of a shock-expansion field for the data at M_∞ = 0.96 at X/L = 0.8. This may be due to a shock wave generated by the fuel dump vent.

The upper nacelle centerline data (fig. 19(c)) show that from $M_\infty = 0.64$ to $M_\infty = 1.05$ downstream of $X/L = 0.8$, steeper gradients occur than those for the upper fuselage (fig. 19(a)). This may be due to the closer proximity of the expansion field generated by the vertical tail. Sonic flow is reached for $M_\infty = 0.90$ and $M_\infty = 0.96$. C_p values from -0.3 to -0.4 are noted just ahead of the nozzle. At the higher Mach numbers, the afterbody C_p values at X/L greater than 0.8 become less negative, reaching values just under atmospheric at $M_\infty = 2.00$. The overall profile change with X/L diminishes with increasing Mach number above $M_\infty = 1.40$.

Figure 19(d) shows that the Mach number effects for the lower nacelle centerline are much weaker than those for the upper nacelle and lower fuselage. The aftmost C_p values decrease from -0.1 at $M_\infty = 0.64$ to -0.22 at $M_\infty = 1.05$. Further increase in M_∞ causes an increase in the aftmost C_p values to slightly under atmospheric pressure at $M_\infty = 2.00$. The profiles at $M_\infty = 1.60$ and $M_\infty = 2.00$ show little dependence on fuselage shape, suggesting a thickened boundary layer.

Figure 19(e) shows that the C_p levels for the upper left tail boom are negative and show steep gradients for all Mach numbers. At $M_\infty = 0.90$ and $M_\infty = 0.96$ the sharp compression shown at the aftmost station is probably due to a standing shock wave, since sonic flow is exceeded upstream of this location. This shock wave dissipates at $M_\infty = 1.05$ and is not present for the higher supersonic Mach numbers, where the flow field shows only a steep expansion gradient.

Effect of angle of attack.—The effect of angle of attack on fuselage pressures is shown in figures 20(a) to 20(c). Data are shown for $M_\infty \approx 0.60$, 0.90, and 1.20 at 10,500 meters to 10,900 meters; no data showing the effect of angle of attack were obtained for higher Mach numbers. For $M_\infty \approx 0.60$ and $M_\infty \approx 0.90$ (figs. 20(a) and 20(b), respectively), increasing angle of attack generally reduced pressures on the upper surfaces and increased pressures on the lower surfaces. For $M_\infty = 1.20$ (fig. 20(c)), the results are similar, except that the C_p changes are smaller, corresponding to a smaller range in the test angle of attack.

Effect of angle of sideslip.—The effect of sideslip change from nose left to nose right on fuselage C_p at $M_\infty = 0.80$ is shown in figure 21. Data were obtained at $\alpha = 5°$ at 13,800 meters. Nose-right sideslip causes an increase in C_p for both the top and bottom surfaces of the fuselage and nacelle for all values of X/L. This effect carries over to the first two orifices on the tail boom.

Other effects.—Several other variables were examined for their effects on the fuselage pressures. These included sealing off the segmented flexible fairings, varying the inlet cowl angle, opening the inlet bypass doors, and changing altitude. Systematic tests with variations in the segmented flexible fairings, inlet cowl angle, bypass door position, and altitude were made. These variables had slight or negligible effects on the fuselage pressures. For example, figure 22 illustrates the negligible effect of a cowl angle change from -4° to 11° on fuselage C_p. No systematic variations of horizontal tail and vertical tail were possible.

Boundary Layer Profiles

Boundary layer profile parameters are presented in tabular and graphic form for 12 test conditions. Table 3 shows the test conditions for these data, and table 4 shows the profile parameters PTRAT and $\frac{U}{U_e}$ for the various pitot tube heights on the forward and aft rakes. The data cover the Mach number range 0.60 to 1.20 for the three test altitudes. The left cowl was fixed at 0°.

Figures 23 to 25 show the effects of altitude, Mach number, and angle of attack on the forward and aft boundary layer profiles, respectively. The presence or absence of the forward rake was examined for its effect on the aft boundary layer profile. The data showed no effect of bypass door position.

Figure 23 shows the effect of altitude on the boundary layer profiles for an angle of attack range from 2.1° to 3.1° at Mach numbers of 0.80 and 0.90. The test altitudes are 6600 meters, 10,600 meters, and 13,900 meters. No altitude effects are apparent for the forward rake and for the aft rake at $M_\infty = 0.80$. For the aft rake at $M_\infty = 0.90$, reducing altitude from 10,600 meters to 6600 meters produces only a slight increase in $\frac{U}{U_e}$ below a height of about 16 centimeters.

Figure 24 shows the effect of Mach number on the boundary layer profiles from $M_\infty = 0.60$ to $M_\infty = 1.20$. Angle of attack ranged from 2.5° to 3.5° at 10,600 meters and 13,900 meters. Some of these data indicate that the maximum value of $\frac{U}{U_e}$ is reached at intermediate values of h, after which $\frac{U}{U_e}$ decreases with increasing h. The decrease in $\frac{U}{U_e}$ at the upper part of the rake is attributed to the fuselage flow field and not viscous effects in the boundary layer. Increasing M_∞ from 0.60 to 0.80 shows a negligible effect on $\frac{U}{U_e}$ near the bottom of the profile for the forward and aft rakes. Increasing M_∞ to 0.90 and 1.20 reduces $\frac{U}{U_e}$ slightly near the bottom of the profile for the forward rake. A similar effect is noted for the aft rake as M_∞ increases to 0.90, but the trend is reversed as M_∞ increases further to 1.20.

Figures 25(a) and 25(b) show the effect of angle of attack on the boundary layer profiles for both rakes for $M_\infty = 0.60$, 0.80, 0.90, and 1.20 at h_p = 10,600 meters and 13,900 meters. At $M_\infty = 0.60$ and 0.80, increasing the angle of attack increases $\frac{U}{U_e}$ moderately near the bottom of the profile for both rakes; the largest effect occurs at $M_\infty = 0.80$ at the forward rake. At Mach numbers of 0.90 and 1.20 the effect of angle of attack is reduced, but persists. At the higher values of h, increasing angle of attack reduces $\frac{U}{U_e}$. This is most evident at $M_\infty = 0.80$ for the forward rake and at $M_\infty = 0.60$, 0.80, and 0.90 for the aft rake. Figure 26 shows that the forward rake does not affect the aft rake boundary layer profile.

Boundary Layer Thickness

The boundary layer thickness parameters δ_a and δ_f were analyzed for the 12 test conditions shown in table 3 and 63 other test conditions. These data are presented in figures 27(a) and 27(b), for subsonic Mach numbers and $M_\infty = 1.20$, respectively, for the several test altitudes. The data are plotted against angle of attack.

As shown in figure 27(a), at 6100 meters the thickness of the boundary layer at the forward rake, δ_f, is constant at 24 centimeters for the angle of attack range from 1° to 4°. Further increase in angle of attack reduces δ_f sharply to about 11 centimeters at $\alpha = 7°$. At the higher altitudes the variation of δ_f with angle of attack is similar, except that at the lowest values of angle of attack, δ_f decreases slightly. For both altitude plots δ_f shows good agreement with the predicted flat plate boundary layer thickness at the lower angles of attack.

For the aft rake at 6100 meters, δ_a decreases slightly over the angle of attack range, with a value of about 12 centimeters for intermediate angle of attack values. At the higher altitudes the boundary layer thickens to about 18 centimeters at the lower angles of attack but thins more rapidly with increasing angle of attack than at the lower altitude.

At every altitude, δ_a is considerably smaller than the predicted flat plate boundary layer thickness. This result suggests that the flow near the aft rake is more three dimensional than that near the forward rake. Comparing δ_f and δ_a shows that the aft boundary layer is thinner at all test conditions. Removing the forward rake had no apparent effect on the thickness of the aft boundary layer.

The data for $M_\infty = 1.20$ (fig. 27(b)) are limited, but the trends are similar to those for the subsonic data (fig. 27(a)).

Nozzle Pressures

Figure 28 illustrates the C_p profiles that can occur on an isolated idealized nozzle afterbody. Curve 1 shows the expansion to a minimum value upstream of the fuselage/nozzle juncture. The subsequent pressure rise downstream of the juncture to a positive value of C_p illustrates good recompression and attached flow. Curve 2 is the same as curve 1 except for the downstream nozzle flow. The sharp decrease in slope and loss of compression indicates flow separation, with a corresponding lower pressure on the nozzle surface. Curve 3 illustrates a lower minimum pressure than curves 1 and 2, followed by a sharp instantaneous pressure jump. This sharp jump indicates a standing compression shock wave. Following the shock wave the flow may separate in a manner similar to curve 2. Note that the separation C_p level for curve 3 may lie below that for curve 2 because of the lower upstream value immediately ahead of the separation point.

Several factors affected the pressures measured on the left nozzle of the test airplane and caused changes in C_p from an idealized nozzle afterbody (fig. 29). These included nearby airframe components, such as the vertical tail, horizontal tail boom, and nozzle

interfairing; the surface discontinuity between the fixed and variable portions of the nozzle; variations in right and left nozzle geometry; and upstream flow variations due to changing cowl geometry and leakage flow.

An example of test data that resemble curve 1 in figure 28 is shown in figure 30. The data are from the same test as that illustrated in figure 16. All of the nozzle rows exhibit recompression to positive values of C_p beginning from negative values of C_p. No flow separation is apparent. The rows of static pressure orifices at angular locations of 350° and 182° show the greatest increase in C_p. These two rows are farthest from the influence of the tail on the left, and from the influence of the nozzle interfairing and right nozzle on the right. Although the increases in C_p for these rows are about the same (about 0.24), the row at 182° has a higher C_p at $X/L = 0.931$, since the recompression started at a higher C_p at $X/L = 0.897$. This result is in keeping with figure 16, which shows that the lower nacelle terminal pressure is greater than that for the upper nacelle. Thus, these data indicate that upstream pressure level affects the C_p level on the nozzle.

The data in figure 30 also show that the C_p values for $X/L = 0.931$ for the top rows (the rows at 278°, 302°, 350°, 62°, and 86°) are about the same. This indicates three-dimensional flow around the top of the nozzle, since the C_p values are all different at $X/L = 0.897$. The C_p values at $X/L = 0.931$ for all the bottom rows (the rows at 230°, 182°, and 134°) are about the same and exceed the corresponding values for the top rows. This difference suggests that the horizontal tail boom on the left and the nozzle interfairing on the right tend to separate the flow at the top of the nozzle from that at the bottom of the nozzle.

Effect of left nozzle boattail angle.—The effect of a reduction in left nozzle boattail angle, BTL, from 18.1° to lower values on nozzle C_p is shown in figure 31 for $M_\infty = 0.61$, 0.90, and 1.20. The overall effects for $M_\infty = 0.61$ (fig. 31(a)) are small. The initial C_p values at rows 182° and 230°, which are somewhat isolated from the tail and interfairing, are lower for the 18.1° boattail angle due to greater initial expansion over the steeper boattail angle. The bottom rows show higher terminal values of C_p than do the top rows for both values of BTL.

The data for $M_\infty = 0.90$ (fig. 31(b)) show stronger effects of the BTL change than for figure 31(a), particularly for the initial C_p levels at the bottom rows. This is probably due to the larger boattail angle reduction and the higher M_∞, which causes greater flow expansion from the fixed to the variable nozzle surfaces. Separated flow occurs on some of the rows for BTL = 18.1° for X/L greater than 0.91. Again, as for $M_\infty = 0.61$, the bottom rows show higher terminal C_p values than the top rows.

Figure 31(c) shows the effects at $M_\infty = 1.20$ of a BTL change from 18.1° to 9.3°. At this Mach number, flow is complex and separated flow is more prevalent. At BTL = 18.1° large initial flow expansion occurs for rows 302°, 350°, 182°, and 230°. The subsequent abrupt recompression is believed to be caused by standing shock waves.

The overall effect of decreasing left nozzle boattail angle is to increase the nozzle pressure coefficients for the three test Mach numbers. The data also show the nonuniformity of the pressure profiles for the several nozzle rows.

Effect of right nozzle boattail angle.—The effects of a change in right nozzle boattail angle, BTR, from 13.7° to 6.6° on left nozzle C_p are shown in figure 32. Data are for $M_\infty = 0.88$, BTL = 14.8°, and $\alpha = 6°$. The C_p profiles along each row are essentially parallel; the lower values correspond to the higher boattail angle. This result is explained as follows. As BTR increases at subsonic speeds, the total aft end closure (the ratio of aft end area to maximum cross-sectional area) is decreased, causing the flow approaching the nozzles to expand to a more negative pressure field. This negative field is propagated to the left nozzle due to the three-dimensional effects that exist in a subsonic field.

Effect of Mach number.—Mach number significantly affects nozzle C_p, as shown in figure 33 for the same tests as in figure 19. Figure 33(a) shows the data for Mach numbers of 0.64 and 0.90. The C_p level for all rows is generally reduced at $M_\infty = 0.90$. The row at 182° shows the highest recompression for both Mach numbers. The rows at 278°, 302°, 350°, 62°, and 86° show signs of separation at $M_\infty = 0.90$. For the rows at 302° and 350° the C_p values at $X/L = 0.897$ and 0.904 for $M_\infty = 0.64$ are lower than those for $M_\infty = 0.90$. This is attributed to flow interference from the vertical tail at $M_\infty = 0.64$ due to the tail inclination angle, or toe-in angle (refs. 3 and 4).

Increasing M_∞ from 0.90 to 0.96 (fig. 33(b)) causes only slight reductions in C_p along the nozzle rows except for the first orifice in the rows at 230° and 182°, where the reduction can be termed moderate. Further increase in M_∞ from 0.96 to 1.05 (fig. 33(c)), however, shows a large reduction in C_p for all rows. Flow expansion from the fuselage boattail to the nozzle reduces the initial C_p level for almost all of the rows. The rows at 350°, 230°, and 182° show flow expansion from the fixed to the variable nozzle surface at $M_\infty = 1.05$. The sharp C_p increases in the rows at 350° and 230° suggest standing compression shock waves. The C_p profiles for the rows at 302° and 62° show somewhat smaller increments, and these are also attributed to the shock waves. The row at 86° shows entirely separated flow at $M_\infty = 1.05$.

Increasing M_∞ from 1.05 to 1.20 (fig. 33(d)) increases the overall C_p level slightly on almost all rows with little or no change in profile shape. This trend reversal is attributed to the larger initial C_p value for almost all the rows. The flow at the rows at 62°, 86°, and 134° is entirely separated at $M_\infty = 1.20$. Further increases in M_∞ from 1.20 to 2.00 (figs. 33(e) and 33(f)) cause further increases in C_p. The nozzle flow becomes separated everywhere, and three-dimensional flows predominate. Note that at $M_\infty = 2.00$ the terminal C_p values for the top and bottom rows are nearly equal. The increasing pressure levels on the nozzle with increasing Mach number are believed to be due to upstream effects that are propagated almost unchanged along the nozzle surface.

Effect of angle of attack.—The effects of angle of attack on nozzle C_p are shown in figure 34 for the same tests as in figure 20. Only slight differences in C_p level are noted for some of the rows at each test Mach number as angle of attack increases.

Effect of angle of sideslip.—The effect of changing sideslip from 1° nose left to 1° nose right on nozzle C_p at $M_\infty = 0.80$ is shown in figure 35 for the same tests as in figure 21. The increase in fuselage C_p shown in figure 21 carries over to the nozzle. The C_p profiles most affected are those on the bottom. Overall, the angle of sideslip effects are small.

Effect of cowl angle.—Cowl angle variations, which showed slight effects on fuselage pressures, propagated farther downstream to the upper and side nozzle rows, and had a small effect on the pressure coefficients, as illustrated in figures 36(a) to 36(c). At $M_\infty = 0.59$ (fig. 36(a)) all the rows except the lower ones show C_p changes in the first two orifices. The trends in the left and right sides of the nozzle are opposite. At $M_\infty = 0.89$ (fig. 36(b)) the effect of the cowl is greatest in the rows at 62° and 86°. At $M_\infty = 1.20$ (fig. 36(c)) cowl angle variations had little effect.

Effect of sealed fairings.—The effects of sealing the segmented flexible fairings on nozzle C_p are shown in figure 37 and are small. Data are shown for $M_\infty = 0.90$ $\alpha = 1°$, and h_p = 6000 meters and 6400 meters with the top half of the annular gap sealed. The bottom half was unsealed. For the sealed condition, C_p decreases for the top rows (those at 302° and 350°) at the upstream nozzle stations. There is no change at the downstream stations at these rows. The row at 86° shows a positive increment along the entire nozzle row due to the increased vent flow. This effect is also noted in the rows at 134° and 182° to a lesser extent, and in the first two orifices in the row at 62°. By sealing the vent, the vent air that normally exits through the entire gap was forced to exit through the bottom only. The rows at 302° and 350° show a C_p decrement due to a loss in pressurization, while the row at 86° shows the greatest effect of the exiting vent air. The rise in C_p at the rows adjacent to the row at 86° is due to three-dimensional flow in the separated flow region.

Other effects.—As with the fuselage data, other variables were examined for their possible effects on nozzle C_p. These included altitude (for Reynolds number effects), inlet bypass door position, and horizontal and vertical tail settings. Systematic variation of altitude and the inlet bypass door position showed no effect on nozzle C_p. No systematic variations of the tail settings were possible. Although some variations in NPRL accompanied these test data, they are believed not to affect the results presented.

Nozzle Axial Force

Effect of left nozzle boattail angle and Mach number.—Figure 38 shows the variation of nozzle axial force coefficient C_a with Mach number and left nozzle boattail angle. Data were obtained during level flight maneuvers at the three test altitudes. Angle of attack ranged from 6° at $M_\infty = 0.60$ to 0° at $M_\infty = 2.00$, and right nozzle boattail angle ranged from the military power setting to as low as 2°. The data show C_a to be a strong function of

BTL and M_∞, as suggested by the data in figures 31 and 33. The largest scatter in C_a occurs at $M_\infty = 1.20$ at the higher boattail angles. This is attributed to the range in right nozzle boattail angle and the large sensitivity of C_a to M_∞ in this region. For any BTL the transonic force rise begins at a Mach number of approximately 0.80. At $M_\infty = 0.90$ for military power nozzle, C_a was 0.0013. Peak values of C_a are reached near $M_\infty = 1.00$, after which C_a decreases rapidly with Mach number. For all Mach numbers, the increments in C_a due to boattail angle are approximately constant. At high Mach numbers the curve for BTL = 18.1° approaches the curve for BTL = 14.6° because of the decrease in BTL caused by the engine military lockup feature.

Effect of right nozzle boattail angle.—Figure 39 presents the effect of BTR on the left nozzle axial force coefficient, C_a, for $M_\infty = 0.80$, 0.90, and 1.20 for three fixed values of BTL. Data were obtained at the two lower test altitudes. The data show large and steady increases in C_a with increasing BTR for all test conditions. These effects are not unlike those of figure 38 for the effect of BTL on C_a, but they are smaller.

Effect of angle of attack.—The effect of angle of attack on C_a is shown in figure 40. Data are presented for $M_\infty = 0.60$, 0.90, and 1.20 at 10,700 meters for several boattail angles. The data scatter precludes any interpretation at $M_\infty = 0.90$ and 1.20. There is a slight decrease in C_a at $M_\infty = 0.60$ as angle of attack increases from 1° to 6°.

CONCLUSIONS

Fuselage, boundary layer, and nozzle pressures were measured in flight for a twin-jet fighter over the Mach number range from 0.60 to 2.00 at test altitudes of 6100, 10,700, and 13,700 meters for angles of attack ranging from 0° to 7°. These data constitute the data base from which the following conclusions have been reached.

1. The aft fuselage flow field was complex and showed the influence of the vertical tail, nacelle contour, and the wing. As Mach number increased above 0.64, lower fuselage pressure coefficient decreased rapidly, approaching -1.0 at supersonic speeds. Changes in the boattail angle of either engine affected the upper fuselage and lower fuselage pressure coefficients upstream of the nozzle, and increasing angle of attack generally reduced upper fuselage pressure coefficient and increased lower fuselage pressure coefficient.

2. Profiles of boundary layer velocity ratio on the upper nacelles showed only small changes with Mach number. Increasing the angle of attack increased the profile near the bottom of the rake for all Mach numbers.

3. Boundary layer thickness for the forward nacelle rake agreed with a flat plate-predicted value at the lower angles of attack. Boundary layer thickness for the aft nacelle rake was less than the flat plate-predicted value. For both rakes the thickness of the boundary layer decreased as angle of attack increased above about 4°. The value of boundary layer thickness for the aft rake was always less than that for the forward rake.

4. Profiles of nozzle pressure coefficient were generally nonuniform and were influenced by the vertical tail, horizontal tail boom, and nozzle interfairing; the last two tended to separate flow over the top of the nozzle from flow over the bottom of the nozzle. The data also showed the effects of the oncoming fuselage flow, and indicated flow separation, standing shock waves, and three-dimensional flow. As Mach number increased above 0.60 the level of nozzle pressure coefficient generally decreased until a Mach number of 1.20 was reached and then increased as Mach number increased further to 2. Decreases in left and right nozzle boattail angle increased nozzle pressure coefficient, but the effects of angle of attack, angle of sideslip, cowl angle, and the leakage through the segmented flexible fairings were small.

5. The left nozzle axial force coefficient was most affected by Mach number and left nozzle boattail angle but was also affected by the right nozzle boattail angle. At a Mach number of 0.90 the nozzle axial force coefficient for the military power nozzle was 0.0013.

6. The overall effect of Reynolds number variation due to the test range in altitude on all data was small.

Ames Research Center
Dryden Flight Research Facility
National Aeronautics and Space Administration
Edwards, California, February 4, 1982

REFERENCES

1. Webb, Lannie D.; Whitmore, Stephen A.; and Janssen, Randall L.: Preliminary Flight and Wind Tunnel Comparisons of the Inlet/Airframe Interaction of the F-15 Airplane. AIAA Paper 79-0102, Jan. 1979.

2. Nugent, Jack; Taillon, Norman V.; and Pendergraft, Odis C., Jr.: Status of a Nozzle-Airframe Study of a Highly Maneuverable Fighter. AIAA Paper 78-990, July 1978.

3. Pendergraft, Odis C., Jr.: Fuselage and Nozzle Pressure Distributions on a 1/12-Scale F-15 Propulsion Model at Transonic Speeds. NASA TP-1521, 1979.

4. Plant, Thomas J.; Nugent, Jack; and Davis, Robert A.: Flight-Measured Effects of Boattail Angle and Mach Number on the Nozzle Afterbody Flow of a Twin-Jet Fighter. AIAA Paper 80-0110, Jan. 1980.

5. Martens, Richard E.: F-15 Nozzle/Afterbody Integration. AIAA Paper 74-1100, Oct. 1974.

6. Swann, M. R.; Duke, E. L.; Enevoldson, E. K.; and Wolf, T. D.: Experience With Flight Test Trajectory Guidance. AIAA Paper 81-2504, Nov. 1981.

7. Allen, Jerry M.; and Monta, William J.: Turbulent-Boundary-Layer Characteristics of Pointed Slender Bodies of Revolution at Supersonic Speeds. NASA TN D-4193, 1967.

8. Saltzman, Edwin J.; and Fisher, David F.: Some Turbulent Boundary-Layer Measurements Obtained From the Forebody of an Airplane at Mach Numbers up to 1.72. NASA TN D-5838, 1970.

9. Fisher, David F.; and Saltzman, Edwin J.: Local Skin Friction Coefficients and Boundary-Layer Profiles Obtained in Flight From the XB-70-1 Airplane at Mach Numbers up to 2.5. NASA TN D-7720, 1973.

TABLE 1.—LOCATIONS OF ORIFICES IN EACH NOZZLE ROW

Nozzle row, φ, deg	Location, X/L[a]							
	0.897[b]	0.904	0.911	0.919	0.924	0.928	0.931	0.934
62	x	x	x	x	x	---	x	---
86	x	---	x	---	x	---	x	---
134	---	---	x	x	x	---	x	---
182	x	x	x	x	x	---	x	---
230	x	---	x	---	x	---	x	---
278	x	---	x	---	x	---	x	---
302	x	x	x	x	x	x	x	x
350	x	x	x	x	x	---	x	---

[a]Average value for all boattail angles.

[b]Fixed portion of nozzle; all other X/L values are on variable portion of nozzle.

TABLE 2.—ESTIMATED UNCERTAINTIES IN NOZZLE PRESSURE COEFFICIENT AND AXIAL FORCE COEFFICIENT

M_∞	h_p, m	α, deg	R_L	BTL, deg	q_∞, N/cm^2	p_ℓ, N/cm^2	C_p	C_a
0.603	10,279	3.0	93×10^6	18.1	0.645	2.491	±0.043	$\pm 4.2 \times 10^{-4}$
0.604	6,303	5.0	137	18.2	1.157	4.433	±0.029	±2.4
0.608	6,103	3.3	140	18.2	1.203	4.557	±0.029	±2.3
0.791	13,180	3.0	83	17.8	0.703	1.533	±0.037	±3.9
0.792	13,594	7.1	78	17.8	0.661	1.458	±0.040	±4.1
0.795	13,626	5.1	78	17.8	0.661	1.431	±0.040	±4.1
0.801	6,151	5.2	184	18.0	2.075	4.532	±0.018	±1.3
0.807	10,660	5.0	119	18.1	1.088	2.289	±0.027	±2.5
0.815	10,642	2.8	121	18.1	1.114	2.324	±0.026	±2.5
0.891	10,663	3.1	131	18.1	1.325	2.264	±0.022	±2.1
0.898	13,666	3.6	88	17.9	0.838	1.409	±0.032	±3.3
0.901	13,678	4.9	88	17.9	0.843	1.420	±0.032	±3.2
0.903	6,103	3.5	208	18.1	2.470	4.422	±0.015	±1.0
0.903	6,628	3.0	211	9.6	2.470	4.102	±0.016	±0.8
0.904	13,713	1.4	88	17.9	0.844	1.419	±0.032	±3.2
1.190	5,809	2.0	296	9.9	4.804	3.787	±0.017	±0.4
1.197	10,691	1.3	181	11.8	2.384	1.799	±0.019	±0.9
1.198	13,525	1.2	116	11.6	1.528	1.289	±0.023	±1.3
1.203	10,697	1.1	173	14.4	2.403	1.828	±0.019	±0.9
1.401	10,701	0.3	211	16.9	3.257	1.800	±0.015	±0.8
2.001	13,859	0.8	189	16.3	4.043	1.156	±0.009	±0.5

TABLE 3.—TEST CONDITIONS FOR BOUNDARY LAYER PROFILES

[$\rho = 0°$]

Test point[a]	M_∞	h_p, m	α, deg	β, deg	R_L	Bypass door position	p_{t_∞}, N/cm^2	p_∞, N/cm^2	T_{t_∞}, K
1	0.577	10,952	5.6	-0.2	75.0×10^6	Closed	2.86	2.28	250
2	0.597	10,684	3.5	0.1	81.3	Closed	3.03	2.38	251
3	0.793	13,924	3.1	0.2	69.4	Closed	2.16	1.43	251
4	0.800	10,581	3.1	0.1	125.0	Closed	3.68	2.42	241
5	0.801	10,686	7.0	0.1	109.0	Closed	3.63	2.38	264
6	0.889	13,875	3.5	0	78.1	Closed	2.40	1.44	259
7	0.892	10,822	2.5	0.2	119.0	Closed	3.90	2.33	271
8	0.905	5,949	2.1	0.1	224.0	Closed	7.95	4.75	288
9	0.906	13,650	3.2	-0.4	85.0	Closed	2.54	1.49	254
10	0.909	10,743	6.1	0.1	123.0	Closed	4.02	2.36	272
11	1.203	13,987	0.9	0.5	108.0	Closed	3.44	1.41	282
12	1.205	13,884	2.5	0.2	109.0	Open	3.50	1.44	285

[a]The original number for test point 1 was 16; for 2, 14; 3, 36; 4, 29; 5, 33; 6, 74; 7, 66; 8, 56; 9, 72; 10, 68; 11, 82; and 12, 85.

Table 3.—Concluded

Test point[a]	Forward rake						Aft rake					
	$p_{\ell_{rk}}$, N/cm^2	R_{L_f}	U_e, m/sec	δ_f, cm	δ^*, cm	θ, cm	$p_{\ell_{rk}}$, N/cm^2	R_{L_a}	U_e, m/sec	δ_a, cm	δ^*, cm	θ, cm
1	2.30	51.3×10^6	174.2	20.52	1.09	0.84	2.20	65.0×10^6	188.9	11.18	0.69	0.53
2	2.65	55.6	180.1	23.13	1.83	1.40	2.52	70.4	195.8	17.52	0.98	0.74
3	1.45	47.5	233.2	22.90	2.17	1.51	1.36	60.1	247.3	13.14	0.99	0.67
4	2.48	85.5	227.1	22.00	2.05	1.41	2.31	108.4	244.0	16.13	0.94	0.65
5	2.41	74.8	238.7	13.34	1.09	0.76	2.26	94.8	253.0	7.03	0.51	0.35
6	1.46	53.4	263.8	25.21	3.38	2.09	1.41	67.7	269.5	19.87	1.80	1.18
7	2.39	81.7	266.6	24.36	2.98	1.89	2.28	103.0	276.2	18.87	1.63	1.07
8	4.86	153.0	274.3	25.48	3.01	1.93	4.69	195.0	281.6	12.10	0.98	0.65
9	1.47	(b)	(b)	(b)	(b)	(b)	1.46	73.7	267.7	17.35	1.61	1.04
10	2.31	85.0	279.5	18.37	2.45	1.50	2.36	107.0	273.3	12.75	1.05	0.70
11	1.74	73.9	312.4	21.56	2.82	1.63	1.55	93.6	333.8	19.94	1.43	0.79
12	1.72	74.6	320.1	20.52	2.90	1.64	1.51	94.5	339.7	12.36	1.26	0.71

[a]The original number for test point 1 was 16; for 2, 14; 3, 36; 4, 29; 5, 33; 6, 74; 7, 66; 8, 56; 9, 72; 10, 68; 11, 82; and 12, 85.

[b]Forward rake removed.

TABLE 4.—BOUNDARY LAYER PROFILES

Test point 1					
Forward rake			Aft rake		
h, cm	PTRAT	$\frac{U}{U_e}$	h, cm	PTRAT	$\frac{U}{U_e}$
0	0	0	0	0	0
0.76	0.916	0.771	0.76	0.903	0.797
1.40	0.923	0.792	1.40	0.929	0.861
3.99	0.960	0.898	3.94	0.967	0.945
7.87	0.986	0.963	7.77	0.991	0.993
13.46	1.002	0.998	13.41	0.997	1.005
19.18	1.002	0.998	19.18	0.992	0.994
24.64	1.005	1.005	24.89	0.983	0.976
29.41	1.003	1.001	29.11	0.974	0.959
33.93	1.004	1.002	33.83	0.969	0.950
38.43	1.000	0.994	38.43	0.966	0.947
Test point 2					
Forward rake			Aft rake		
h, cm	PTRAT	$\frac{U}{U_e}$	h, cm	PTRAT	$\frac{U}{U_e}$
0	0	0	0	0	0
0.76	0.903	0.744	0.76	0.887	0.772
1.40	0.911	0.770	1.40	0.914	0.839
3.99	0.942	0.856	3.94	0.950	0.916
7.87	0.968	0.920	7.77	0.981	0.976
13.46	0.986	0.962	13.41	0.990	0.993
19.18	0.997	0.987	19.18	0.996	1.003
24.64	1.006	1.005	24.89	0.997	1.005
29.41	1.005	1.001	29.11	0.995	1.002
33.93	1.007	1.007	33.83	0.991	0.995
38.43	0.998	0.987	38.43	0.987	0.986
Test point 3					
Forward rake			Aft rake		
h, cm	PTRAT	$\frac{U}{U_e}$	h, cm	PTRAT	$\frac{U}{U_e}$
0	0	0	0	0	0
0.76	0.821	0.717	0.76	0.801	0.741
1.40	0.836	0.748	1.40	0.844	0.813
3.99	0.887	0.839	3.94	0.923	0.924
7.87	0.929	0.903	7.77	0.972	0.981
13.46	0.971	0.961	13.41	0.991	1.001
19.18	0.994	0.989	19.18	0.995	1.005
24.64	1.007	1.005	24.89	0.993	1.003
29.41	1.006	1.004	29.11	0.975	0.984
33.93	1.004	1.001	33.83	0.978	0.987
38.43	0.996	0.992	38.43	0.973	0.982

TABLE 4.—Continued

Test point 4					
Forward rake			Aft rake		
h, cm	PTRAT	$\frac{U}{U_e}$	h, cm	PTRAT	$\frac{U}{U_e}$
0	0	0	0	0	0
0.76	0.826	0.734	0.76	0.818	0.774
1.40	0.831	0.744	1.40	0.847	0.820
3.99	0.879	0.832	3.94	0.929	0.932
7.87	0.928	0.909	7.77	0.970	0.978
13.46	0.975	0.973	13.41	0.990	0.999
19.18	0.995	0.998	19.18	0.992	1.001
24.64	0.999	1.003	24.89	0.996	1.005
29.41	1.001	1.005	29.11	0.987	0.996
33.93	0.999	1.002	33.83	0.977	0.986
38.43	0.991	0.993	38.43	0.969	0.977
Test point 5					
Forward rake			Aft rake		
h, cm	PTRAT	$\frac{U}{U_e}$	h, cm	PTRAT	$\frac{U}{U_e}$
0	0	0	0	0	0
0.76	0.835	0.769	0.76	0.829	0.804
1.40	0.856	0.808	1.40	0.868	0.864
3.99	0.914	0.902	3.94	0.958	0.978
7.87	0.962	0.969	7.77	0.983	1.005
13.46	0.988	1.001	13.41	0.978	1.000
19.18	0.992	1.005	19.18	0.965	0.986
24.64	0.991	1.003	24.89	0.951	0.970
29.41	0.983	0.994	29.11	0.940	0.958
33.93	0.975	0.984	33.83	0.935	0.951
38.43	0.962	0.968	38.43	0.929	0.944
Test point 6					
Forward rake			Aft rake		
h, cm	PTRAT	$\frac{U}{U_e}$	h, cm	PTRAT	$\frac{U}{U_e}$
0	0	0	0	0	0
0.76	0.747	0.659	0.76	0.749	0.699
1.40	0.758	0.680	1.40	0.791	0.769
3.99	0.810	0.770	3.94	0.875	0.882
7.87	0.861	0.844	7.77	0.930	0.943
13.46	0.933	0.931	13.41	0.964	0.976
19.18	0.978	0.977	19.18	0.990	0.999
24.64	1.002	0.999	24.89	0.996	1.005
29.41	1.008	1.005	29.11	0.977	0.987
33.93	1.007	1.005	33.83	0.977	0.988
38.43	0.994	0.985	38.43	0.963	0.975

TABLE 4.—Continued

Test point 7					
Forward rake			Aft rake		
h, cm	PTRAT	$\frac{U}{U_e}$	h, cm	PTRAT	$\frac{U}{U_e}$
0	0	0	0	0	0
0.76	0.762	0.683	0.76	0.759	0.716
1.40	0.778	0.712	1.40	0.793	0.771
3.99	0.820	0.784	3.94	0.877	0.883
7.87	0.870	0.855	7.77	0.936	0.947
13.46	0.940	0.941	13.41	0.978	0.988
19.18	0.985	0.987	19.18	0.993	1.001
24.64	0.999	1.000	24.89	0.998	1.005
29.41	1.003	1.005	29.11	0.992	1.000
33.93	1.004	1.005	33.83	0.988	0.997
38.43	0.998	1.000	38.43	0.985	0.994
Test point 8					
Forward rake			Aft rake		
h, cm	PTRAT	$\frac{U}{U_e}$	h, cm	PTRAT	$\frac{U}{U_e}$
0	0	0	0	0	0
0.76	0.768	0.696	0.76	0.773	0.736
1.40	0.781	0.722	1.40	0.804	0.784
3.99	0.824	0.793	3.94	0.894	0.903
7.87	0.869	0.857	7.77	0.951	0.963
13.46	0.937	0.940	13.41	0.990	1.000
19.18	0.980	0.984	19.18	0.995	1.005
24.64	0.997	1.001	24.89	0.991	0.997
29.41	1.001	1.005	29.11	0.987	0.997
33.93	0.999	1.003	33.83	0.984	0.995
38.43	0.997	1.001	38.43	0.987	0.997
Test point 9					
Forward rake			Aft rake		
h, cm	PTRAT	$\frac{U}{U_e}$	h, cm	PTRAT	$\frac{U}{U_e}$
0	(a)	(a)	0	0	0
0.76	↓	↓	0.76	0.741	0.706
1.40			1.40	0.779	0.769
3.99			3.94	0.864	0.885
7.87			7.77	0.923	0.949
13.46			13.41	0.965	0.989
19.18			19.18	0.982	1.005
24.64			24.89	0.976	1.000
29.41			29.11	0.970	0.994
33.93			33.83	0.956	0.982
38.43			38.43	0.940	0.966

[a]Forward rake removed for this test.

TABLE 4.—Concluded

Test point 10					
Forward rake			Aft rake		
h, cm	PTRAT	$\frac{U}{U_e}$	h, cm	PTRAT	$\frac{U}{U_e}$
0	0	0	0	0	0
0.76	0.721	0.660	0.76	0.777	0.751
1.40	0.738	0.693	1.40	0.814	0.810
3.99	0.807	0.803	3.94	0.898	0.915
7.87	0.889	0.904	7.77	0.950	0.970
13.46	0.967	0.982	13.41	0.980	1.000
19.18	0.990	1.003	19.18	0.987	1.005
24.64	0.993	1.005	24.89	0.981	1.000
29.41	0.991	1.004	29.11	0.967	0.987
33.93	0.987	1.000	33.83	0.953	0.973
38.43	0.982	0.995	38.43	0.939	0.959
Test point 11					
Forward rake			Aft rake		
h, cm	PTRAT	$\frac{U}{U_e}$	h, cm	PTRAT	$\frac{U}{U_e}$
0	0	0	0	0	0
0.76	0.672	0.670	0.76	0.620	0.662
1.40	0.691	0.701	1.40	0.663	0.724
3.99	0.765	0.801	3.94	0.818	0.890
7.87	0.835	0.878	7.77	0.923	0.967
13.46	0.926	0.957	13.41	0.963	0.994
19.18	0.979	0.997	19.18	0.973	0.998
24.64	0.990	1.005	24.89	0.976	1.000
29.41	0.989	1.004	29.11	0.979	1.002
33.93	0.992	1.006	33.83	0.981	1.004
38.43	0.982	0.999	38.43	0.982	1.005
Test point 12					
Forward rake			Aft rake		
h, cm	PTRAT	$\frac{U}{U_e}$	h, cm	PTRAT	$\frac{U}{U_e}$
0	0	0	0	0	0
0.76	0.647	0.650	0.76	0.622	0.700
1.40	0.662	0.676	1.40	0.660	0.753
3.99	0.738	0.783	3.94	0.819	0.911
7.87	0.824	0.877	7.77	0.923	0.984
13.46	0.930	0.965	13.41	0.955	1.003
19.18	0.978	0.999	19.18	0.956	1.004
24.64	0.984	1.004	24.89	0.958	1.005
29.41	0.985	1.004	29.11	0.955	1.003
33.93	0.987	1.004	33.83	0.956	1.004
38.43	0.985	1.004	38.43	0.954	1.003

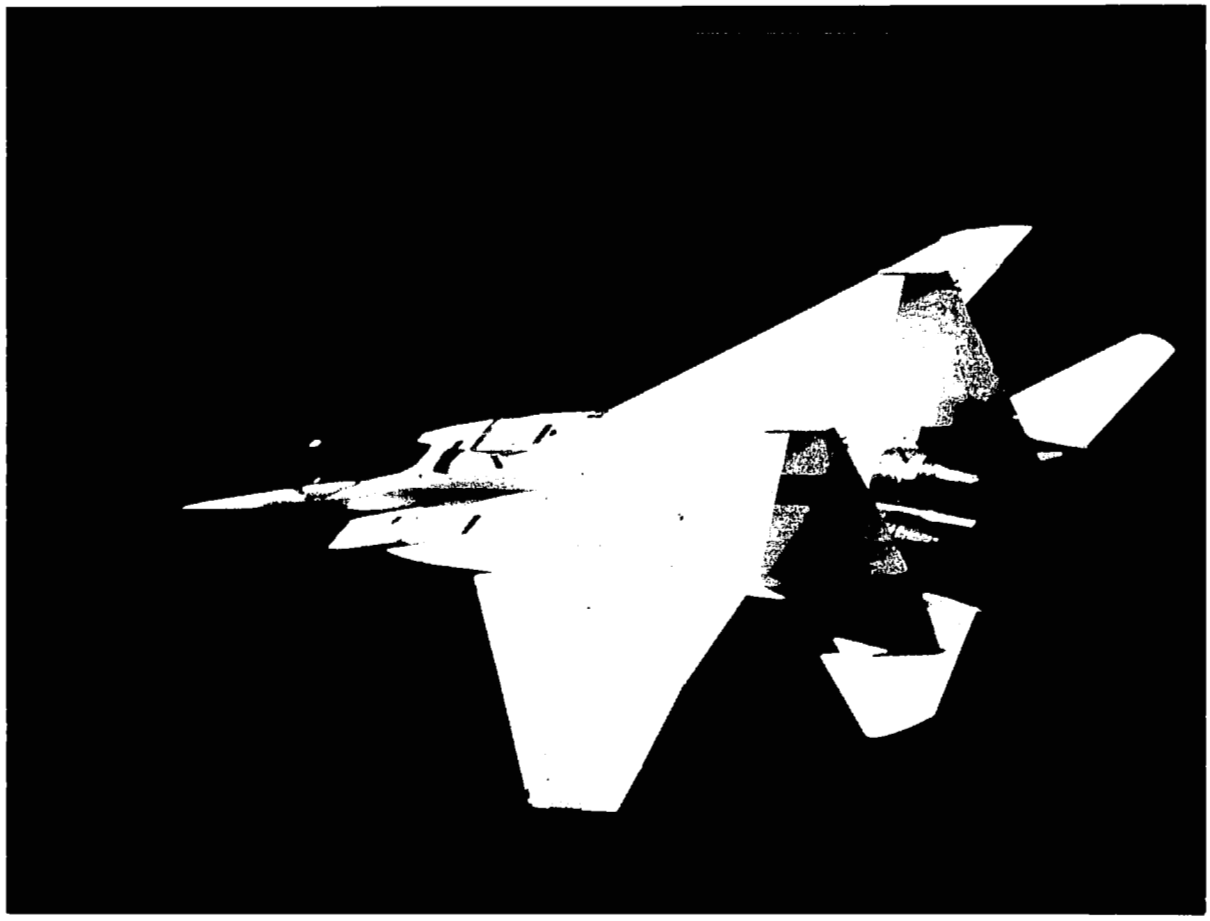

ECN 9325

Figure 1. F-15 airplane.

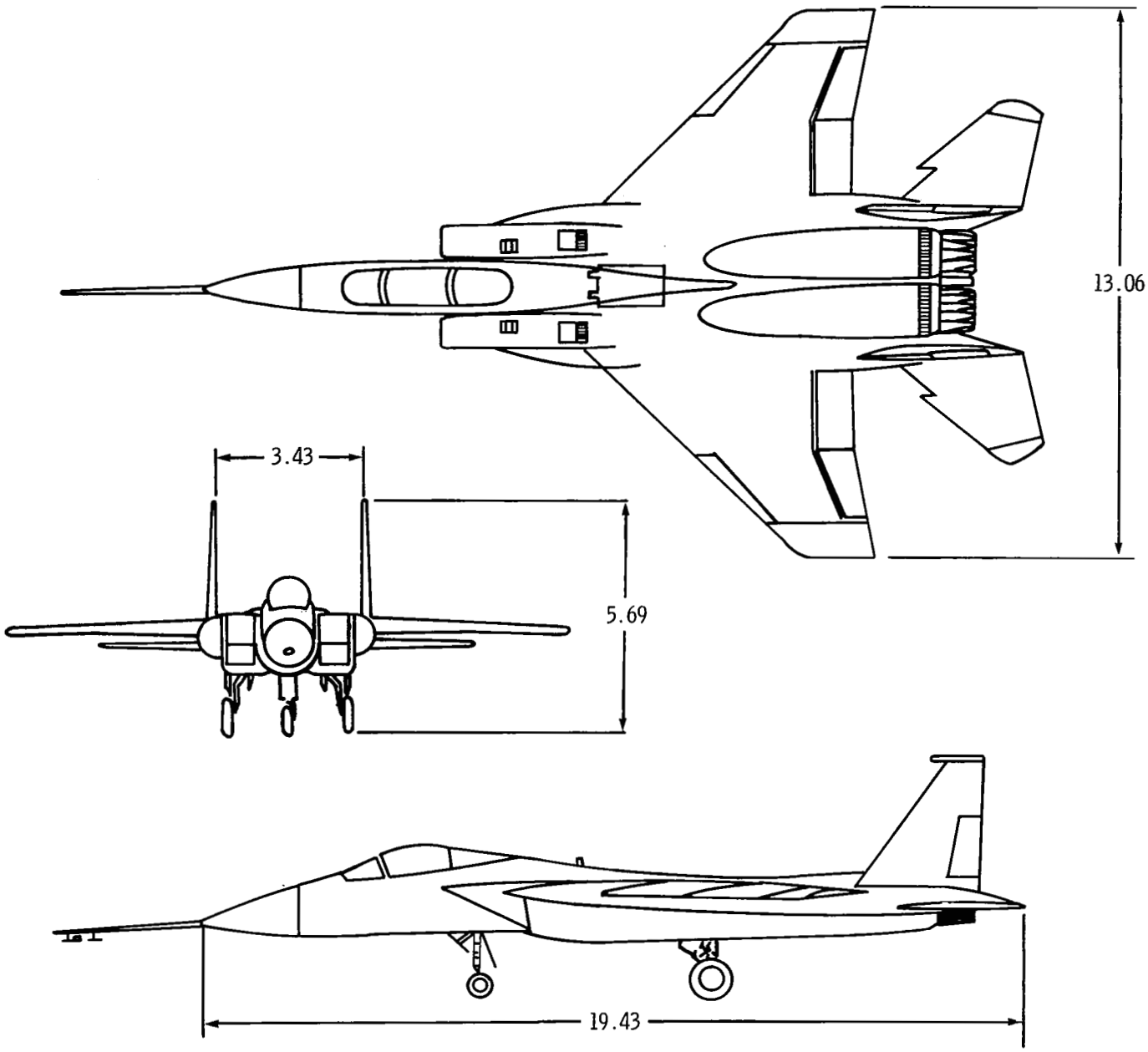

Figure 2. Three-view drawing of F-15 airplane. Dimensions in meters.

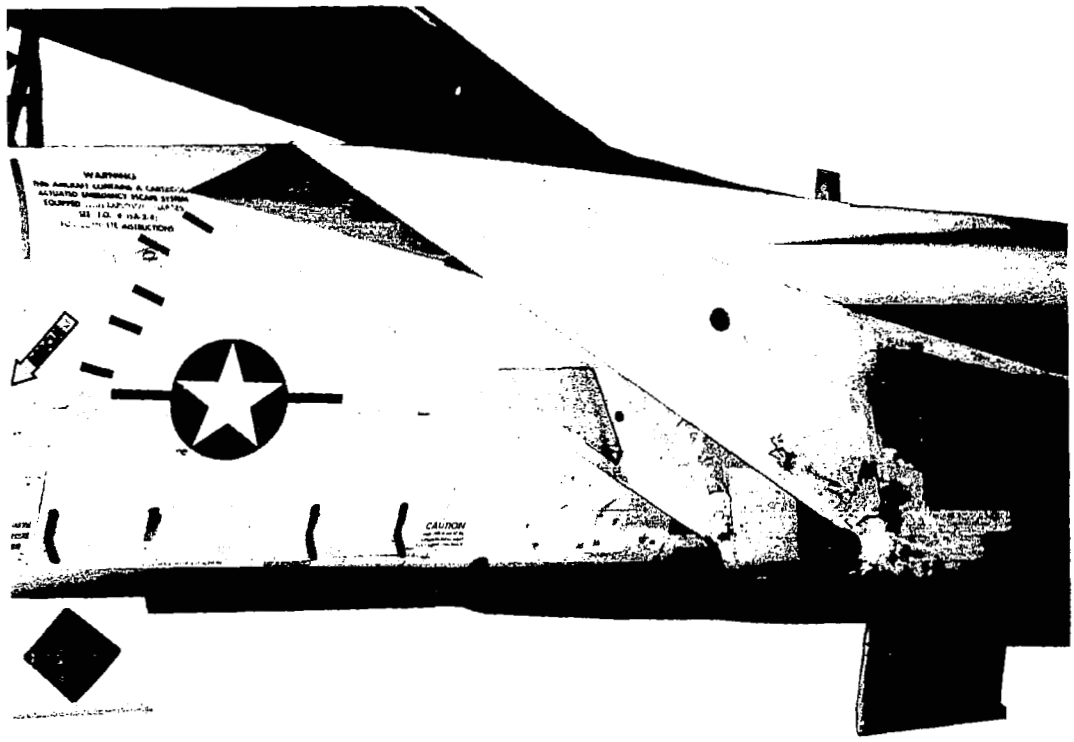

E 29406

(a) Photograph of inlet.

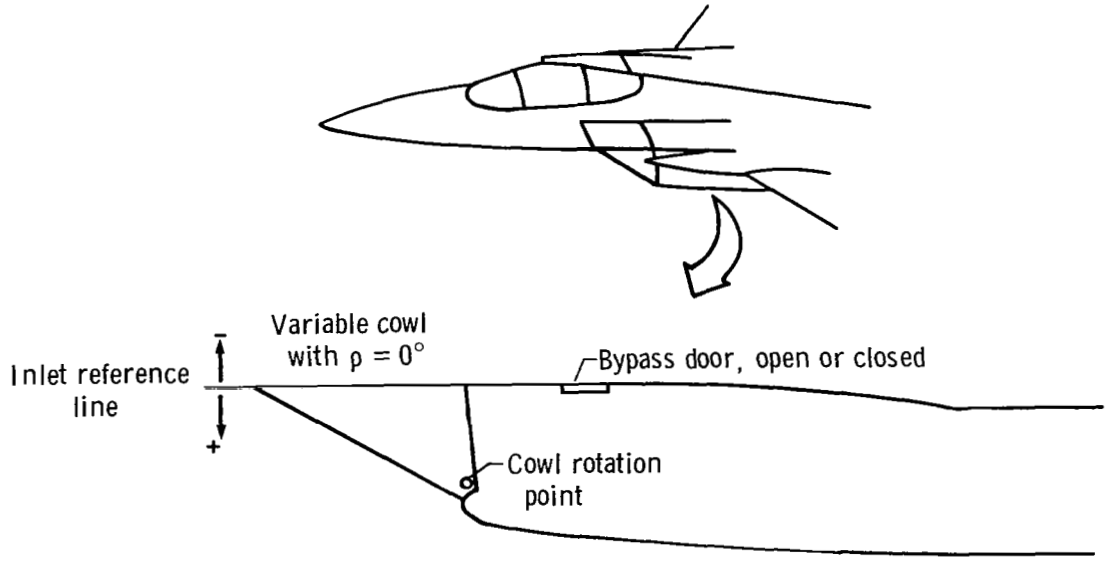

(b) Variable cowl motion and two-position bypass door.

Figure 3. Variable geometry inlet.

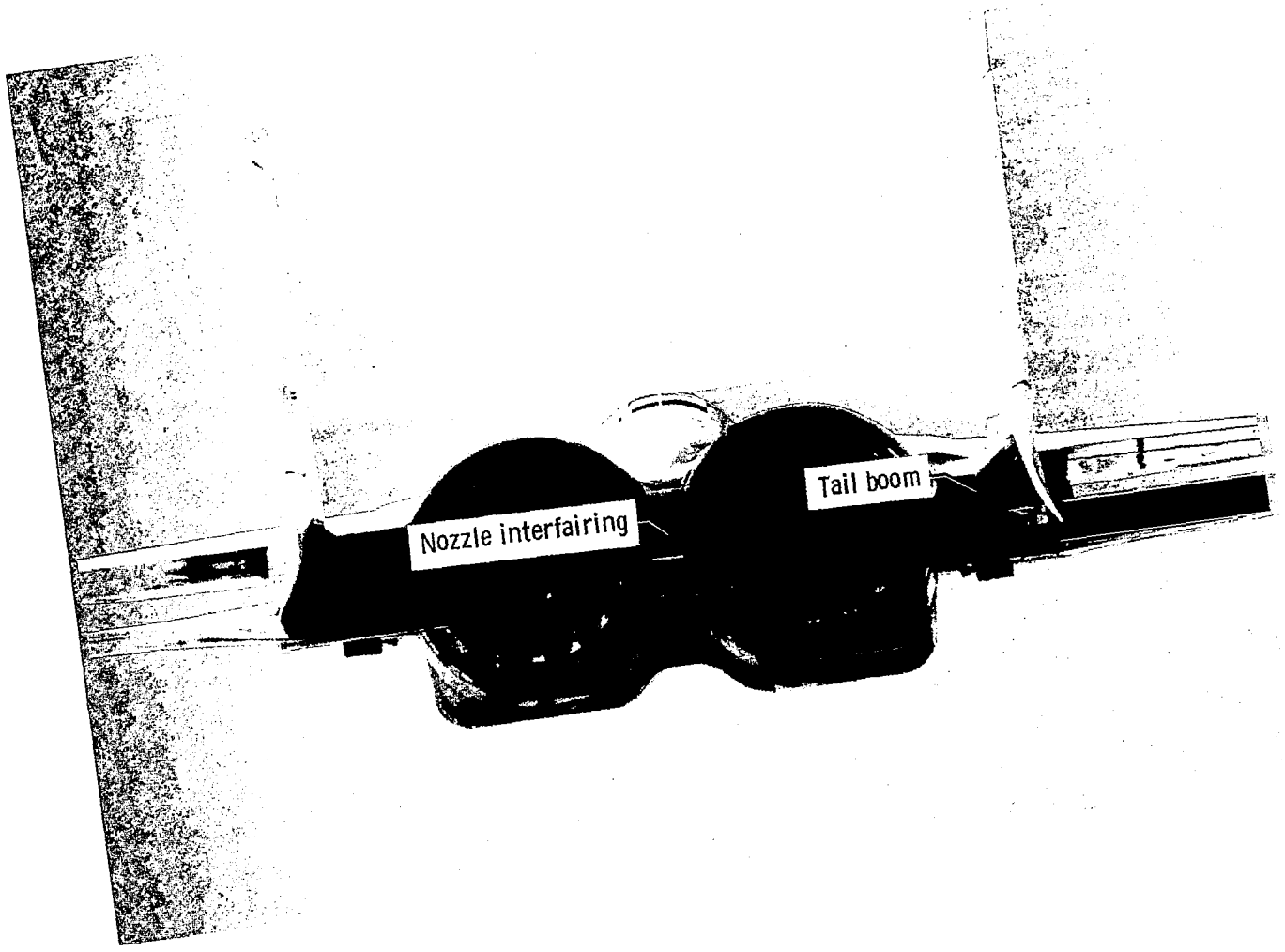

Figure 4. F-15 nozzle afterbody.

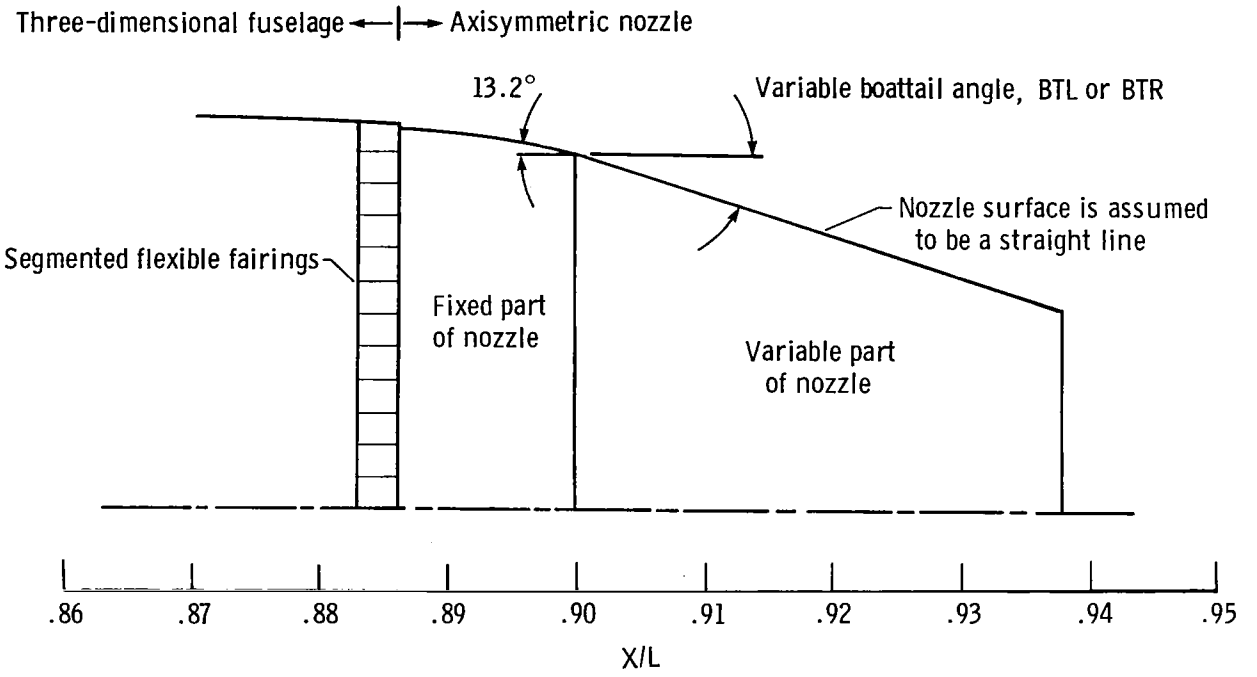

Figure 5. Nozzle afterbody geometry.

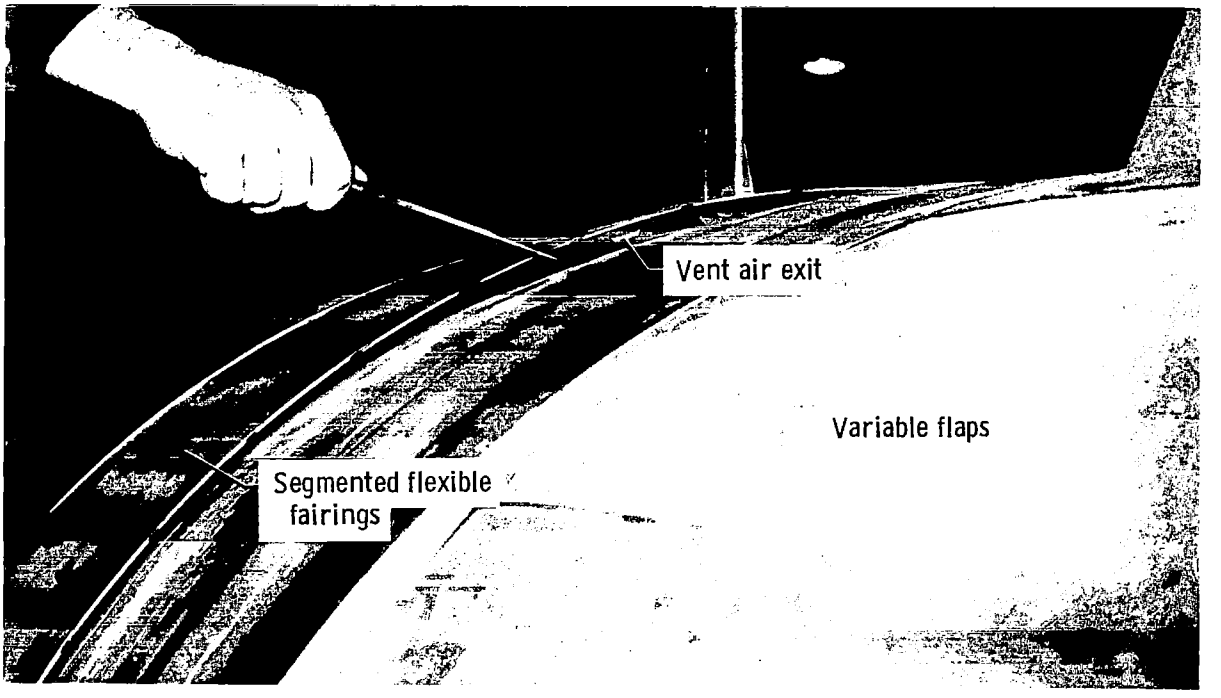

E 35115

Figure 6. Photograph of annular gap used to vent air from engine compartment. View looking forward.

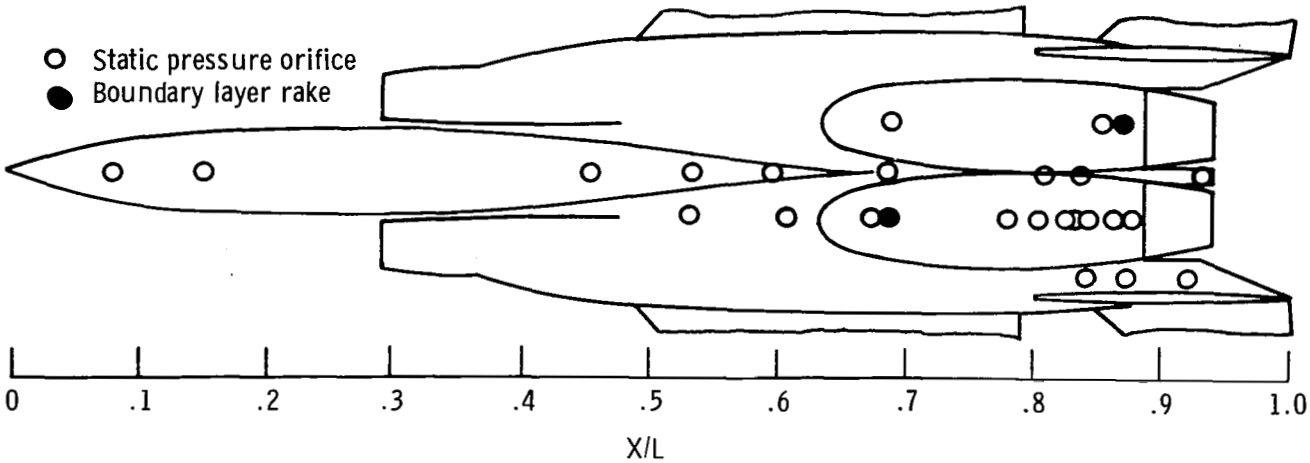

Static Pressure Orifices

Position along—	Orifice location, X/L
Fuselage centerline	0.079 0.154 0.455 0.533 0.597 0.684 0.810 0.840 0.929
Left tail boom	0.839 0.871 0.919

Position along—	Orifice location, X/L
Left nacelle centerline	0.533 0.609 0.677 0.781 0.808 0.829 0.845 0.857 0.872 0.882
Right nacelle centerline	0.684 0.867

Boundary Layer Rakes

Position along—	Rake location, X/L
Left nacelle centerline	0.684
Right nacelle centerline	0.867

(a) Instrumentation on upper surface of fuselage (24 orifices, 2 rakes).

Figure 7. Nondimensionalized locations of fuselage static pressure orifices and boundary layer rakes.

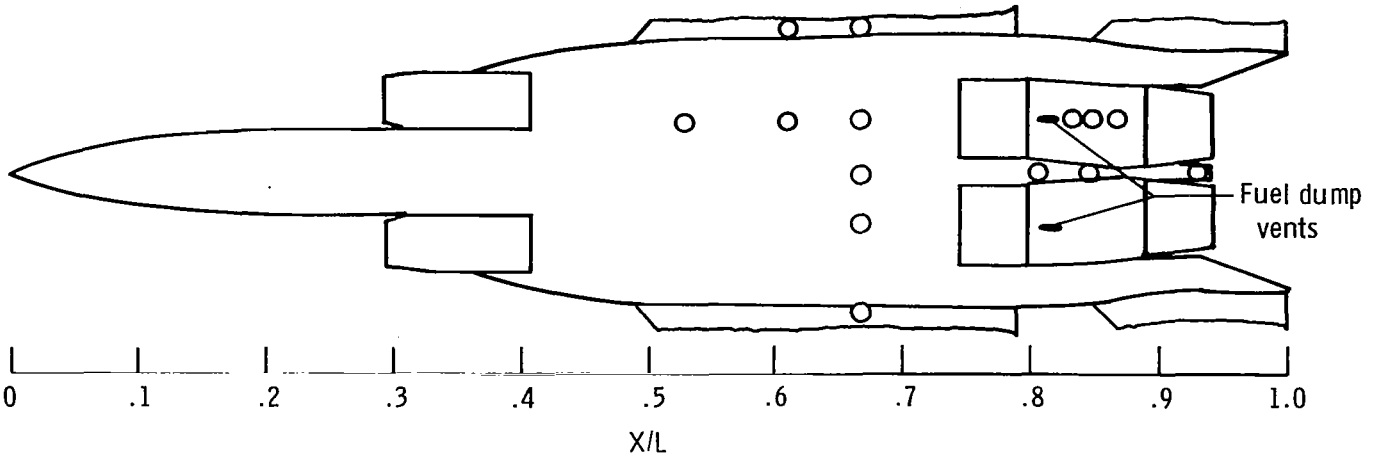

Static Pressure Orifices

Position along—	Orifice location, X/L
Fuselage centerline	0.684 0.804 0.844 0.930
Left nacelle centerline	0.531 0.611 0.684 0.836 0.849 0.870
Right nacelle centerline	0.684
Left side	0.611 0.684
Right side	0.684

(b) Instrumentation on lower and side surfaces of fuselage (14 orifices).

Figure 7. Concluded.

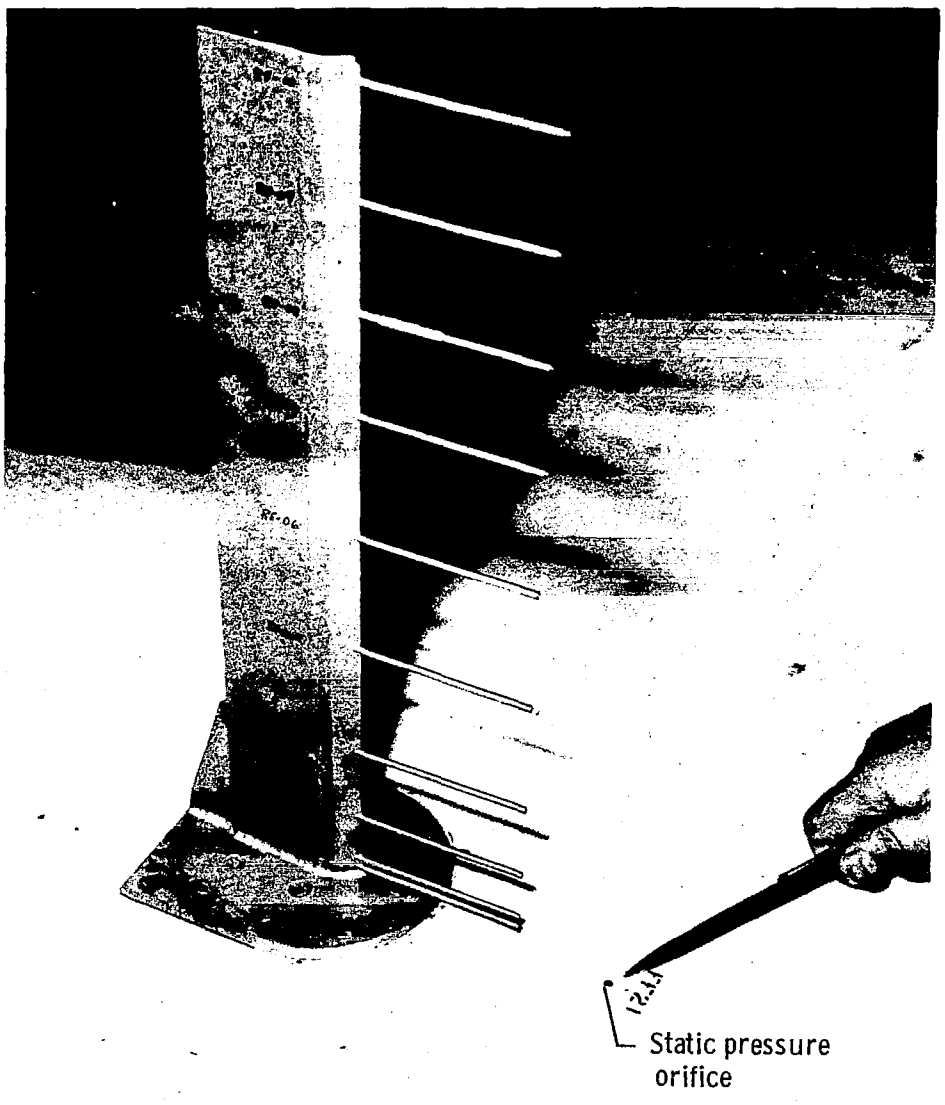

E 35112

(a) Forward boundary layer rake, X/L = 0.684.

Figure 8. Photographs of boundary layer rake and fuel dump vent.

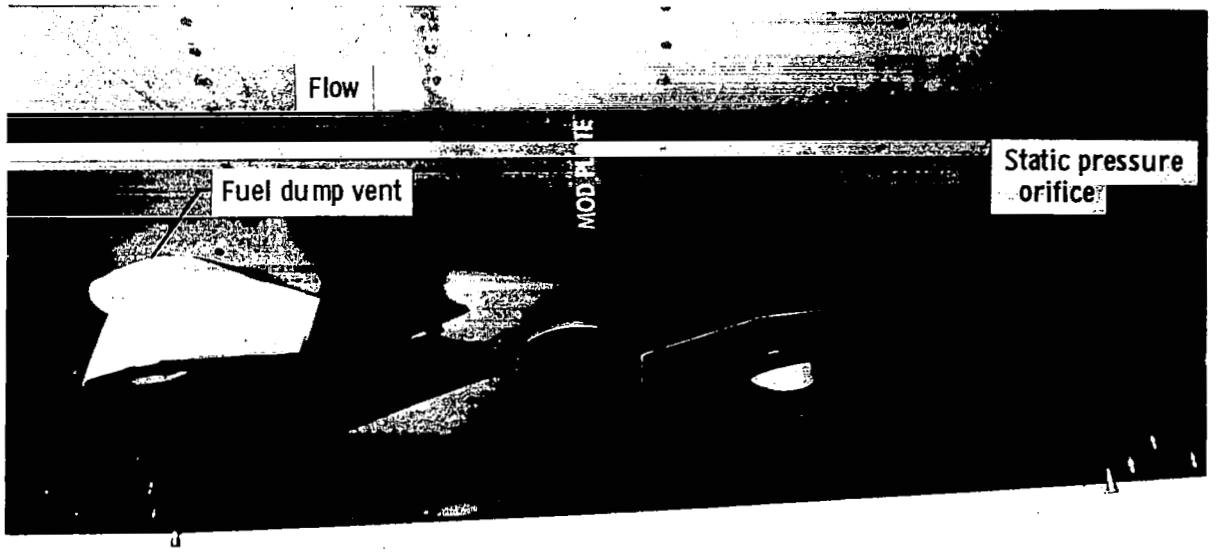

E 38972

(b) Fuel dump vent.

Figure 8. Concluded.

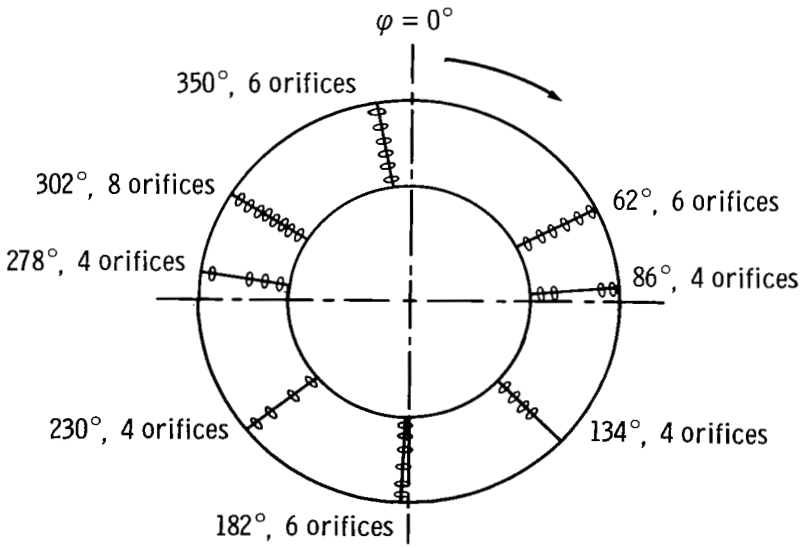

Figure 9. Angular locations of the 42 left nozzle orifices. View looking forward.

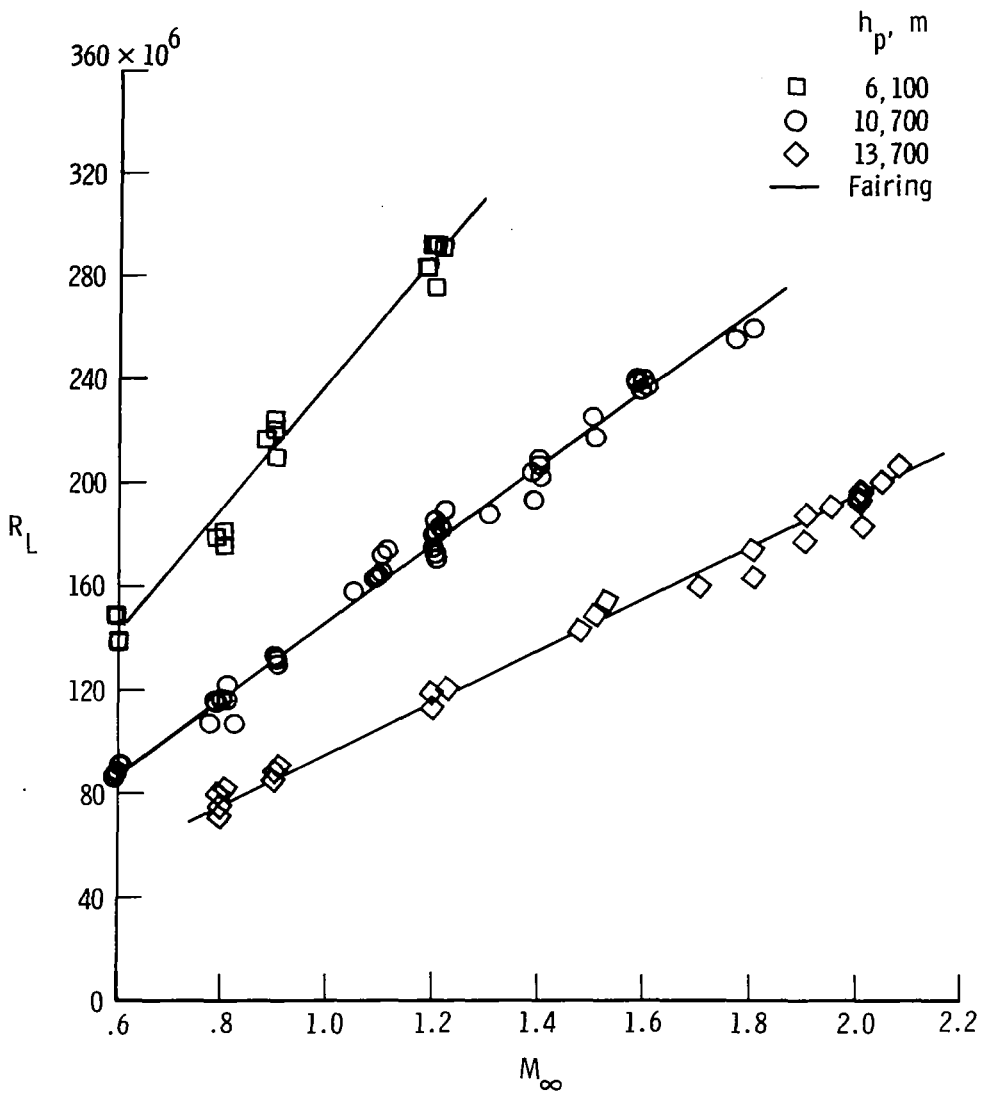

Figure 10. Variation of test Reynolds number with test Mach number.

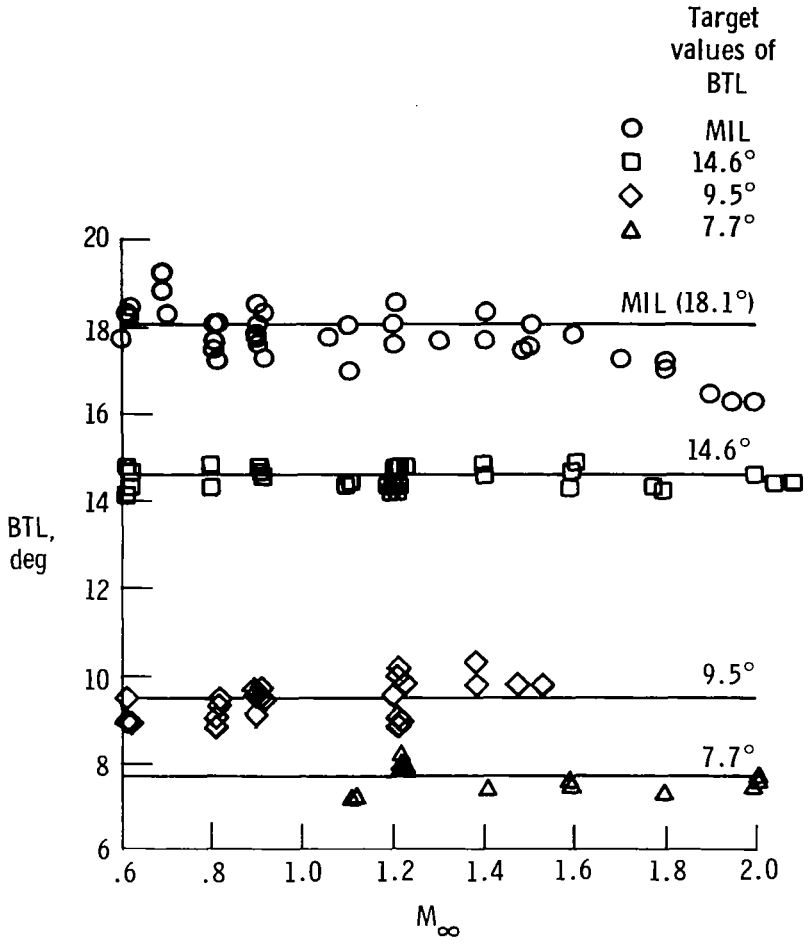

Figure 11. Left nozzle boattail angles tested.

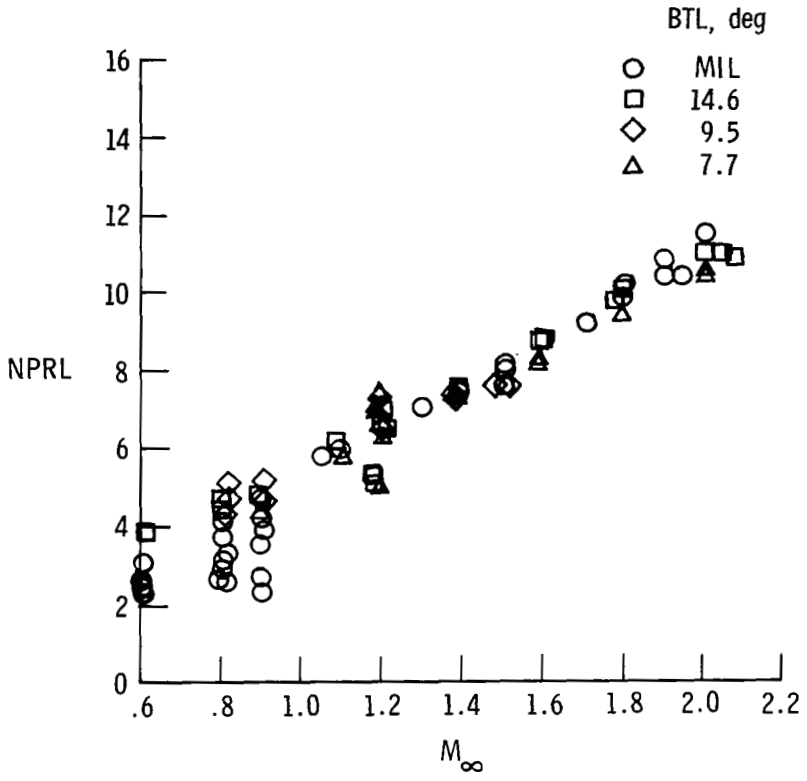

Figure 12. Variation of nozzle pressure ratio with test Mach number.

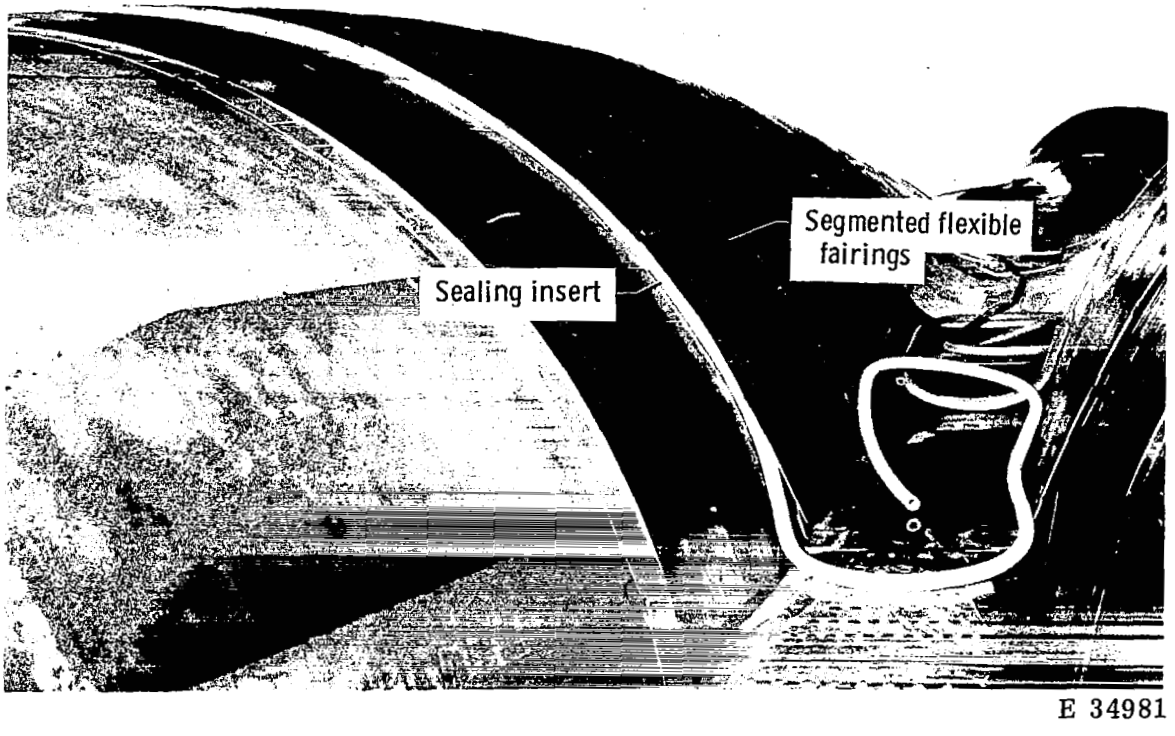

Figure 13. Photograph showing the technique for sealing the upper annular gap. View looking forward.

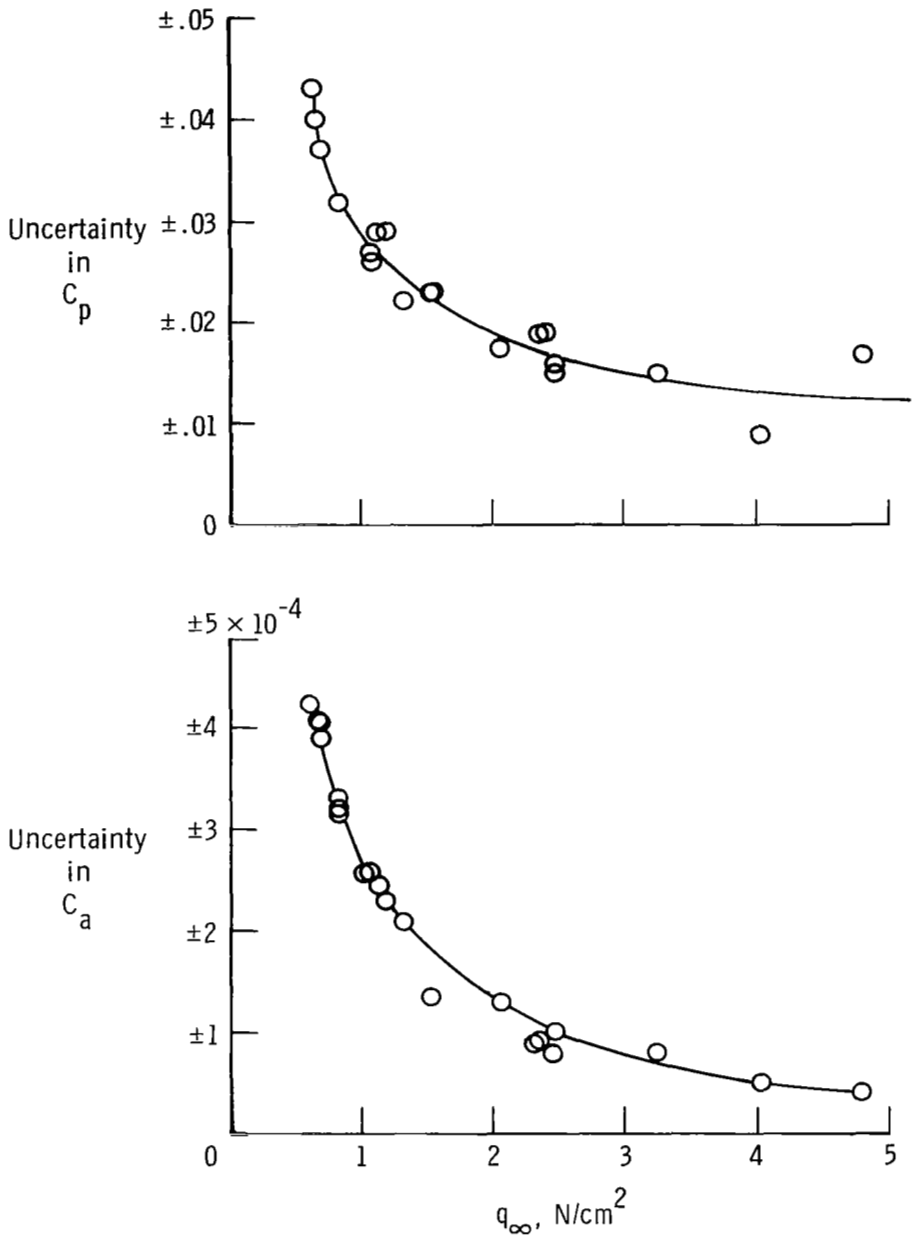

Figure 14. Variation of C_p and C_a uncertainties with free-stream dynamic pressure.

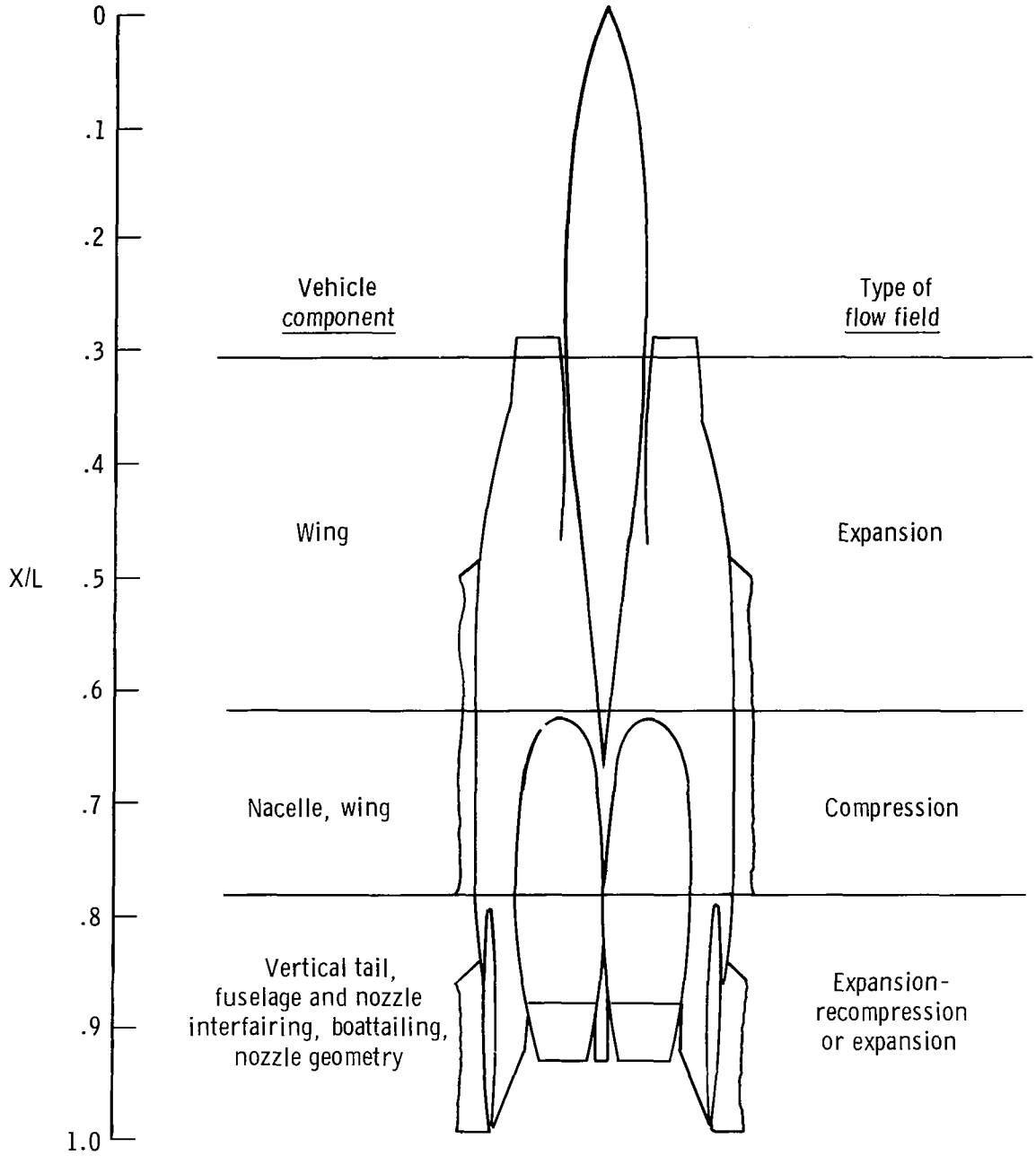

(a) Upper fuselage.

Figure 15. Influence of vehicle components on fuselage flow fields.

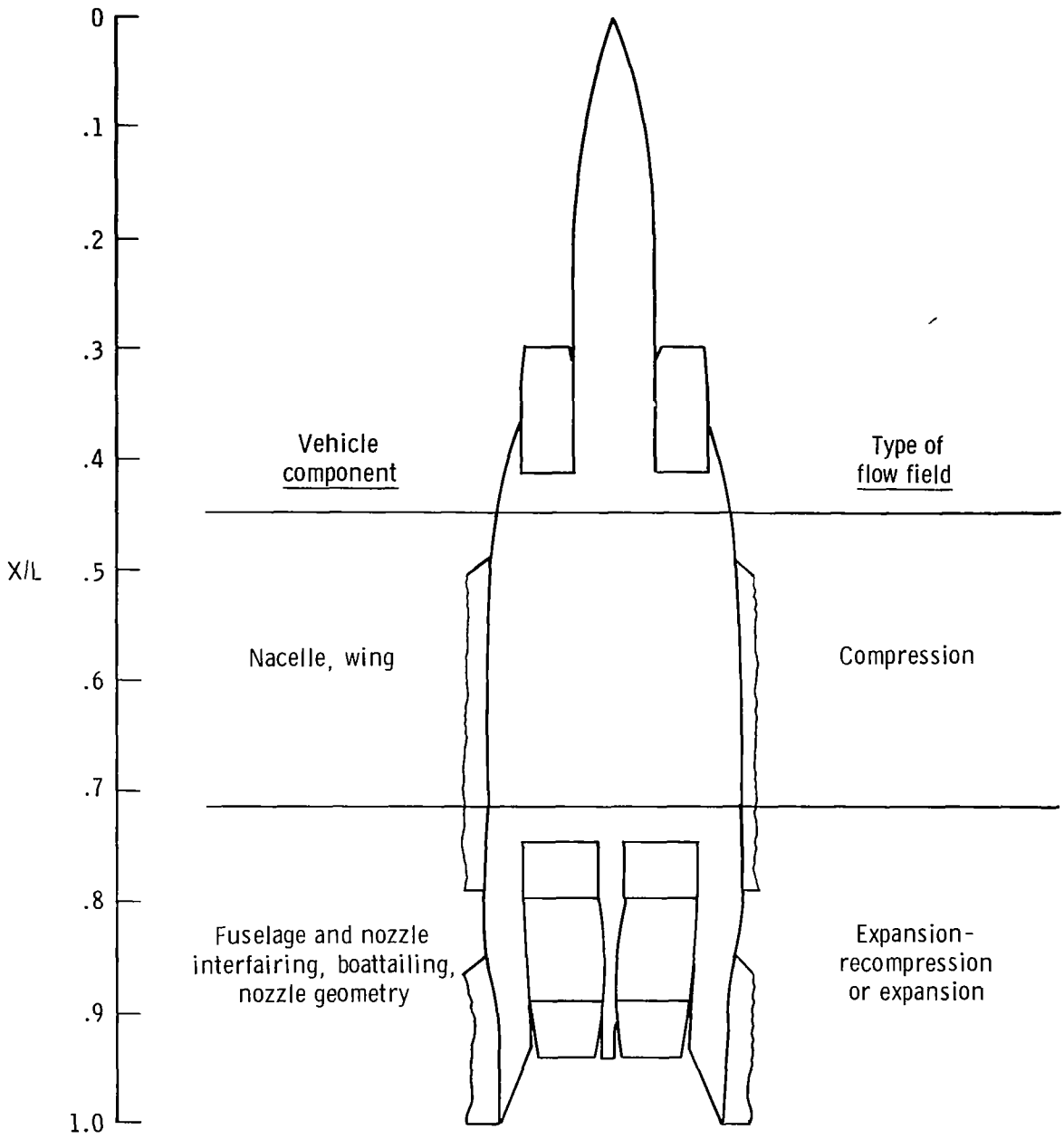

(b) Lower fuselage.

Figure 15. Concluded.

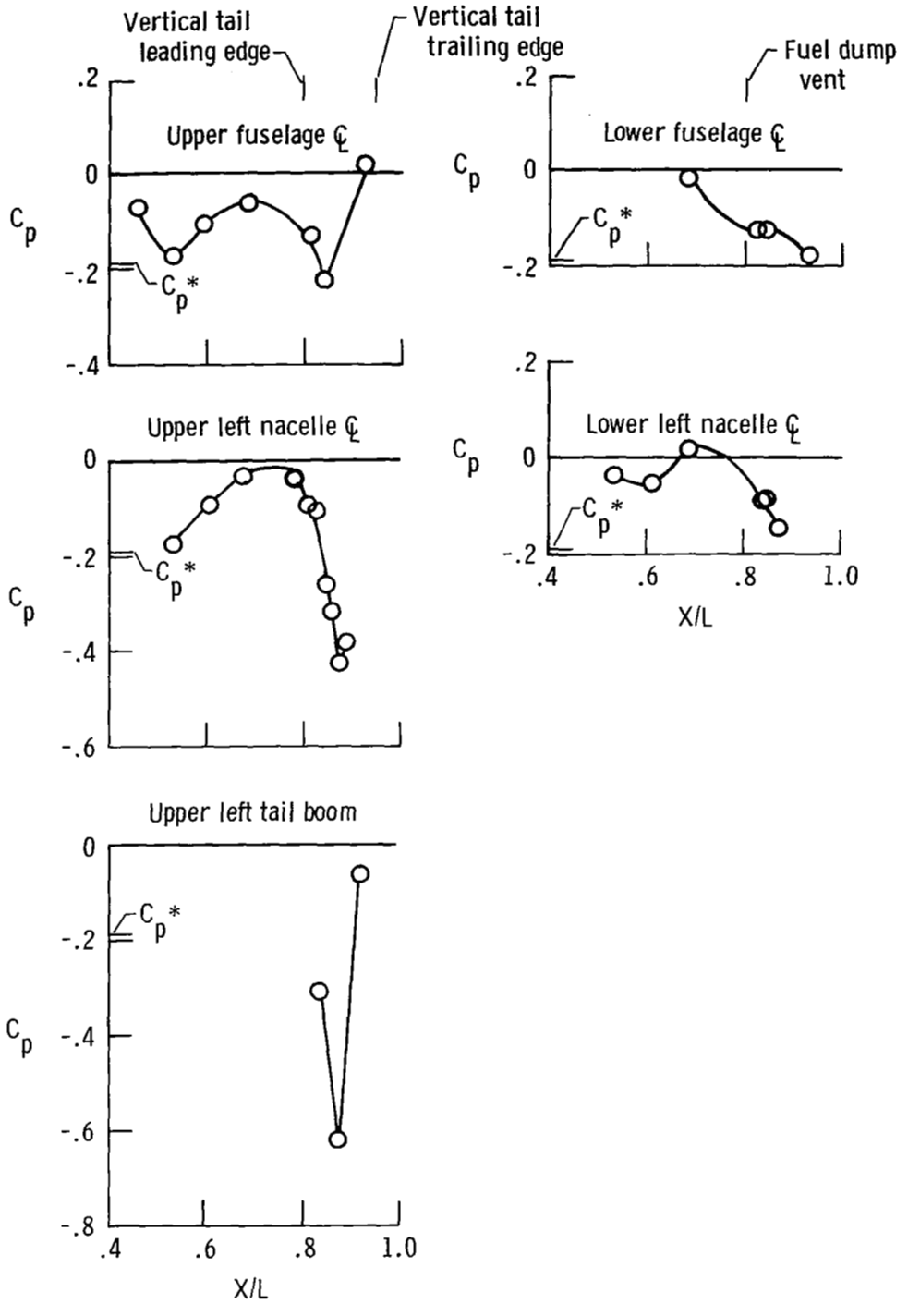

Figure 16. Aft fuselage pressure coefficients for $M_\infty = 0.90$. *BTL = 10.5°; BTR = MIL;* $h_p = 10,600$ *m;* $\alpha \approx 2°$; $\beta = -0.3°$; $\rho = 0°$; *bypass door closed.*

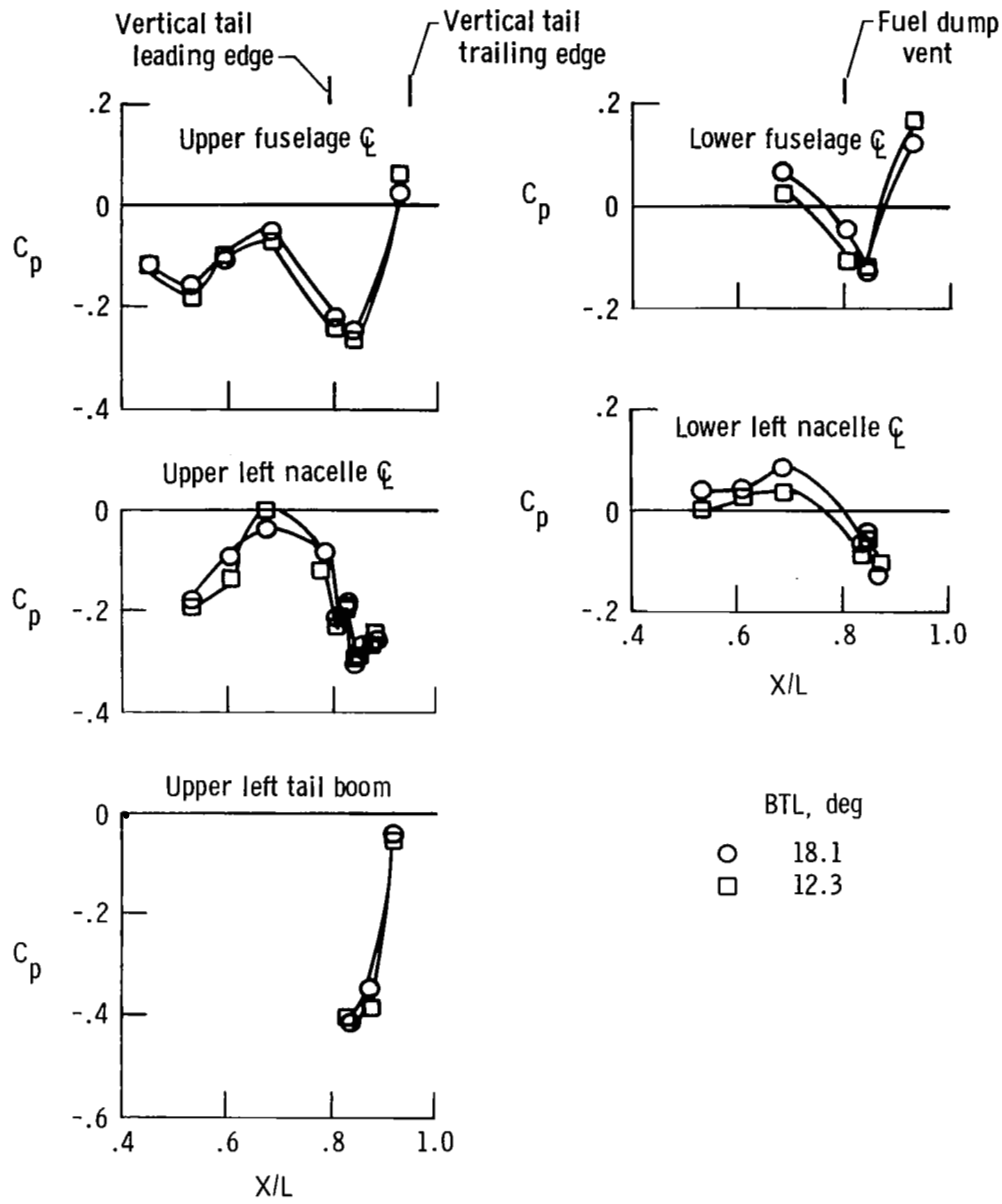

(a) BTL change from 18.1° to 12.3°. M_∞ = 0.61; BTR = MIL; $h_p \approx$ 10,600 m; $\alpha \approx 6°$; $\beta = -0.1°$; $\rho = 0°$; bypass door closed.

Figure 17. Effect of BTL on aft fuselage pressure coefficients.

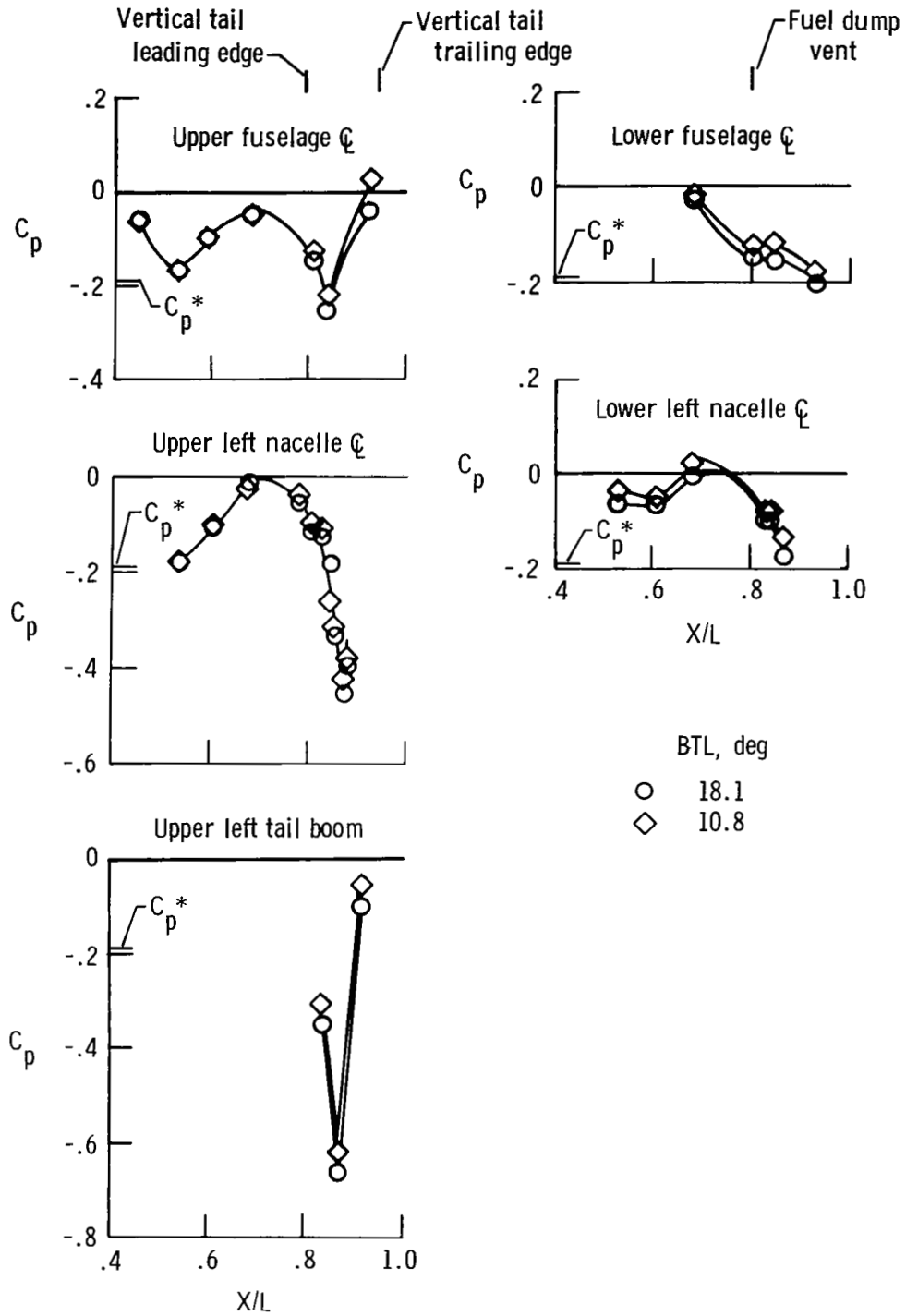

(b) BTL change from 18.1° to 10.5°. $M_\infty \approx 0.90$; BTR = MIL; h_p = 10,600 m; α = 2°; β = -0.3°; ρ = 0°; bypass door closed.

Figure 17. Continued.

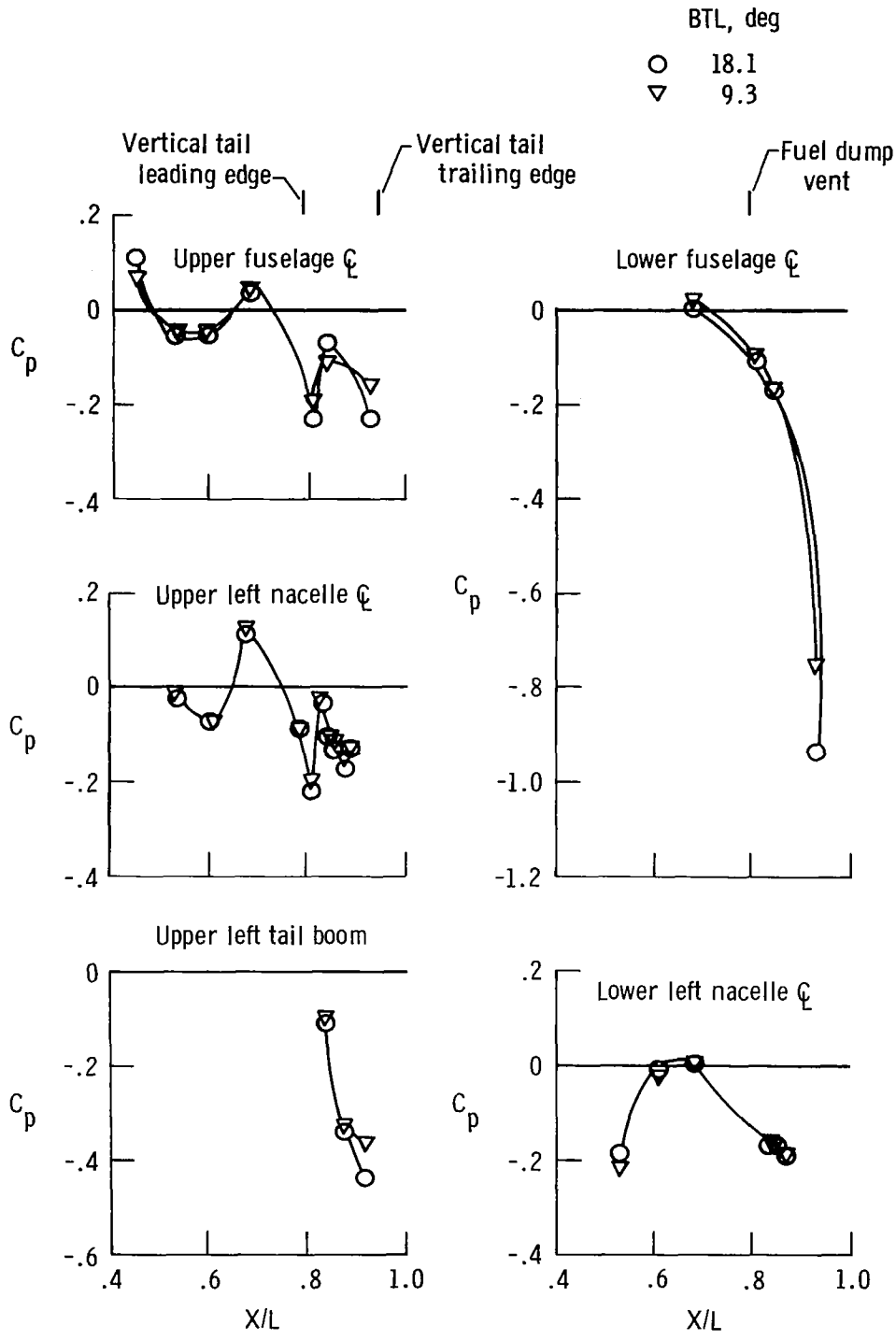

(c) BTL change from 18.1° to 9.3°. $M_\infty \approx 1.20$; BTR = MIL; $h_p \approx 10,700$ m; $\alpha = 1°$; $\beta = -0.4°$; $\rho = 0°$; bypass door closed.

Figure 17. Concluded.

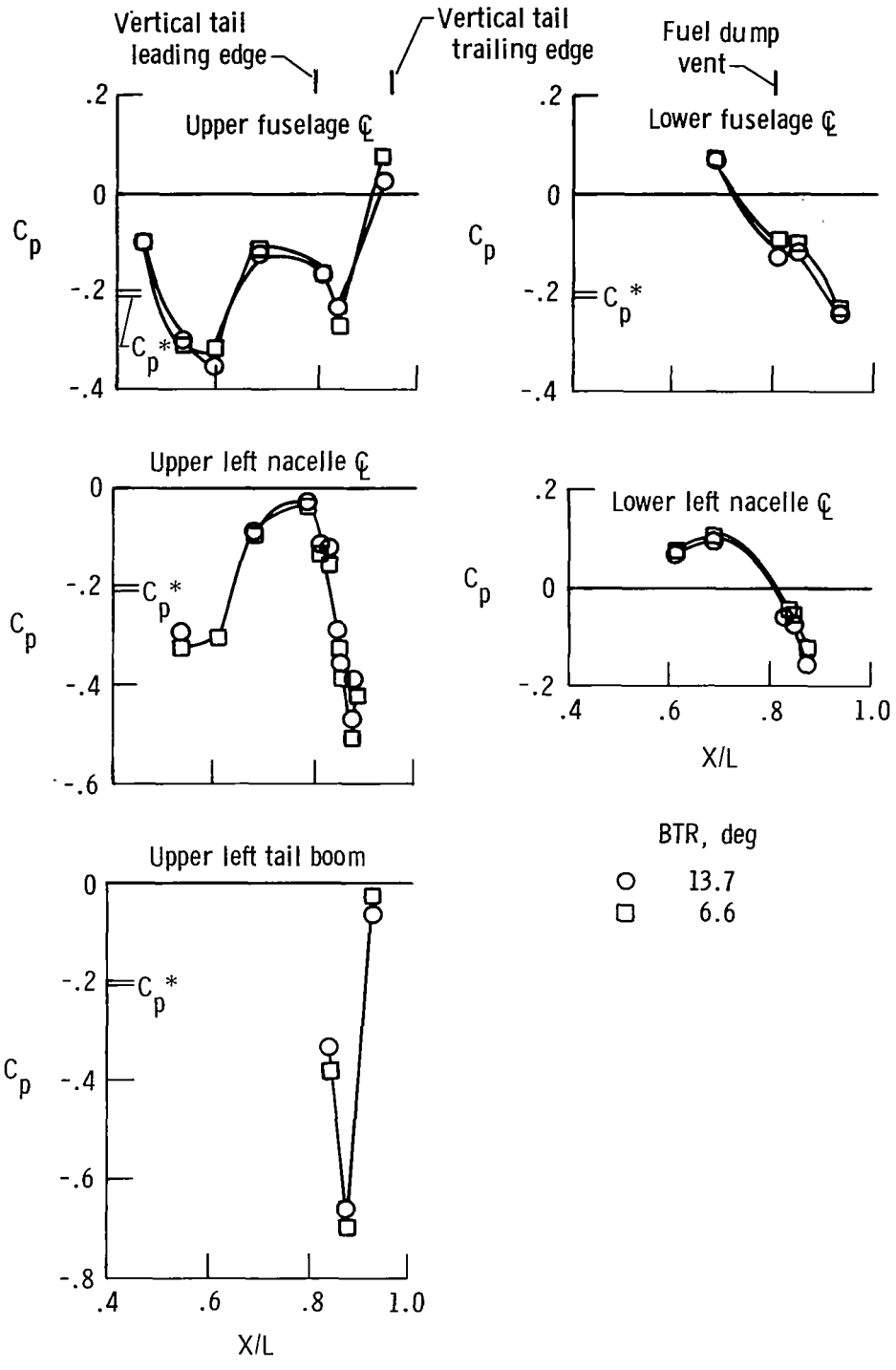

Figure 18. Effect of a BTR change from 13.7° to 6.6° on aft fuselage pressure coefficients. $M_\infty = 0.88$; *BTL* $\approx 14.8°$; $h_p = 6200$ *m;* $\alpha \approx 6°$; $\beta \approx -0.2°$; $\rho = 0°$; *bypass door closed.*

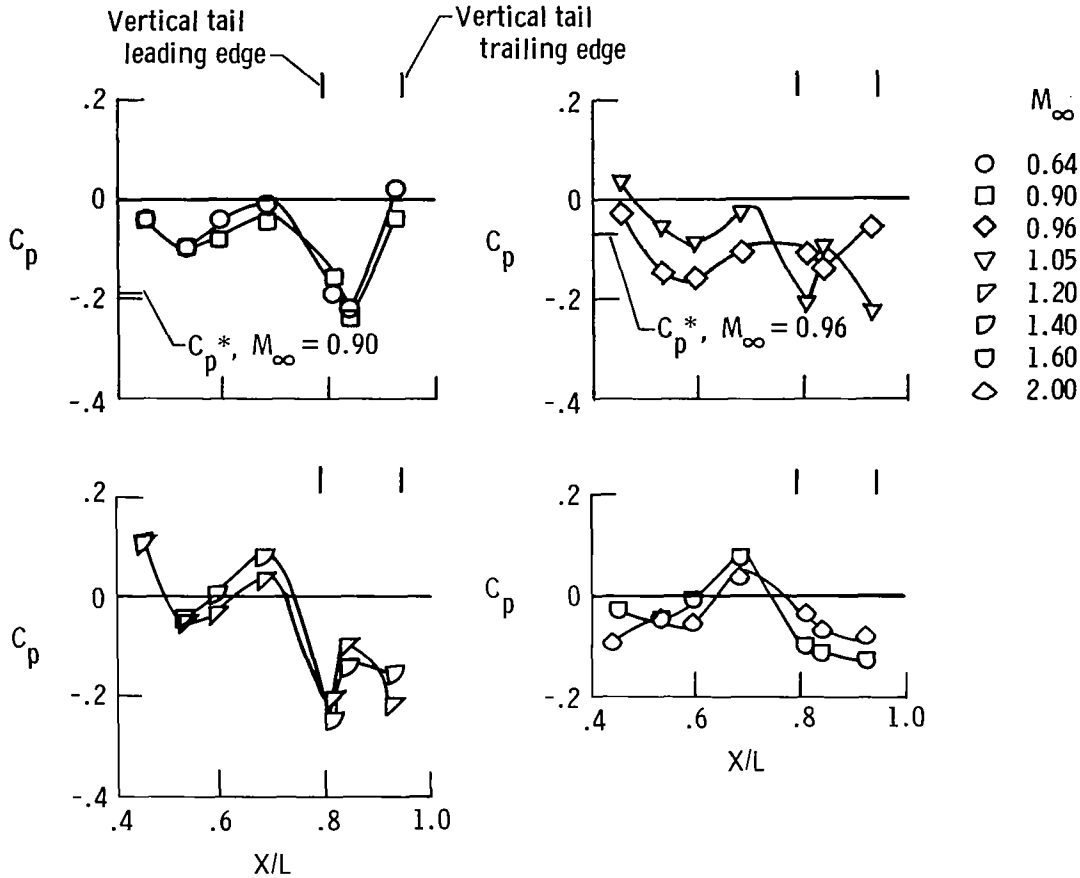

(a) Upper fuselage centerline.

Figure 19. Effect of Mach number on aft fuselage pressure coefficients. BTL = MIL; BTR = MIL and 15.0°; h_p = 10,600 m and 13,900 m; α ≈ 1°; β ≈ 0°; ρ = 0°; bypass door closed.

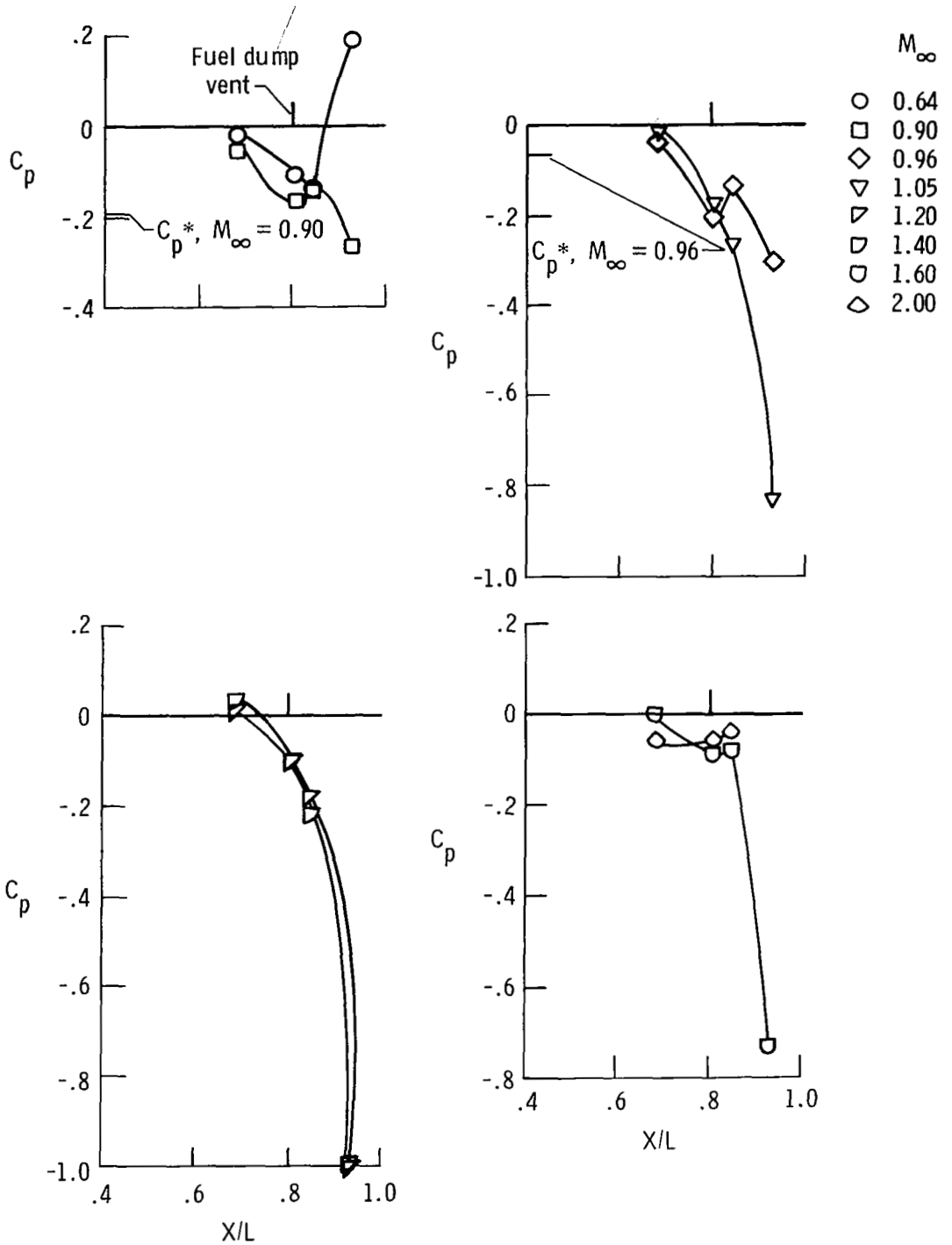

(b) Lower fuselage centerline.

Figure 19. Continued.

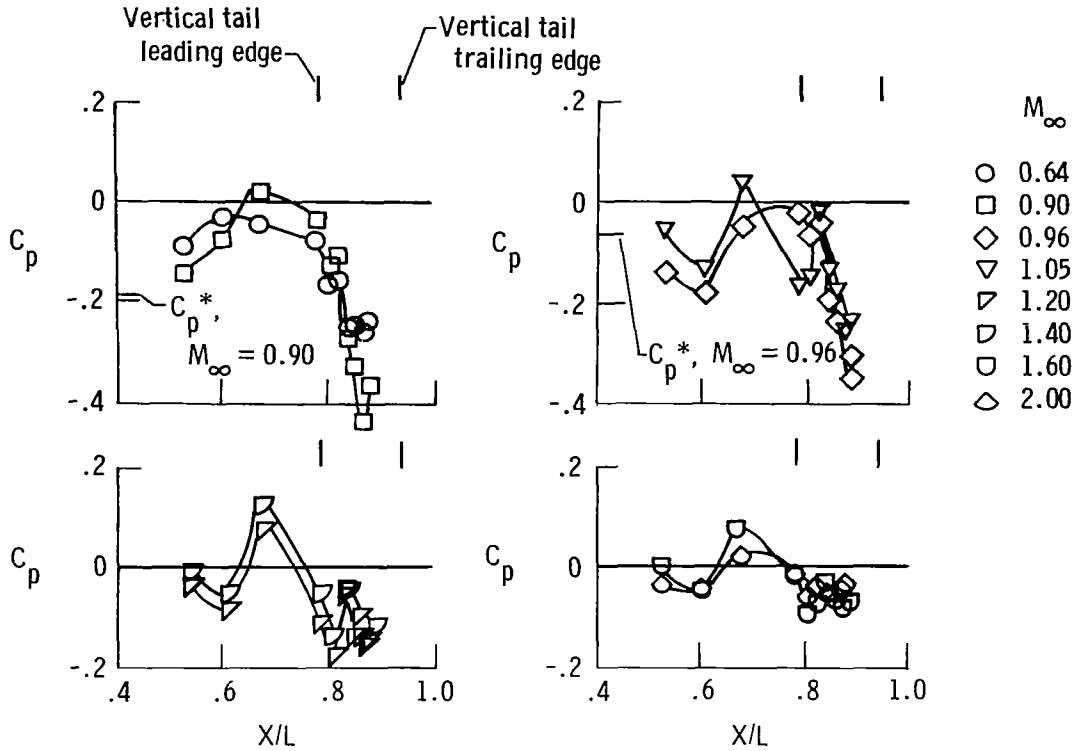

(c) Upper left nacelle centerline.

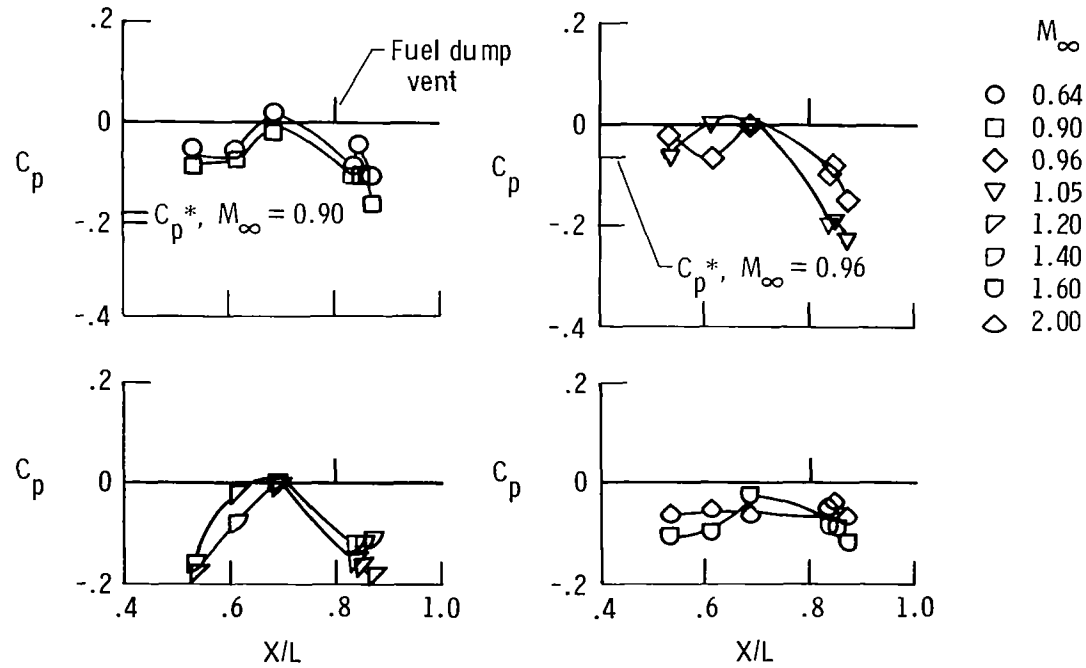

(d) Lower left nacelle centerline.

Figure 19. Continued.

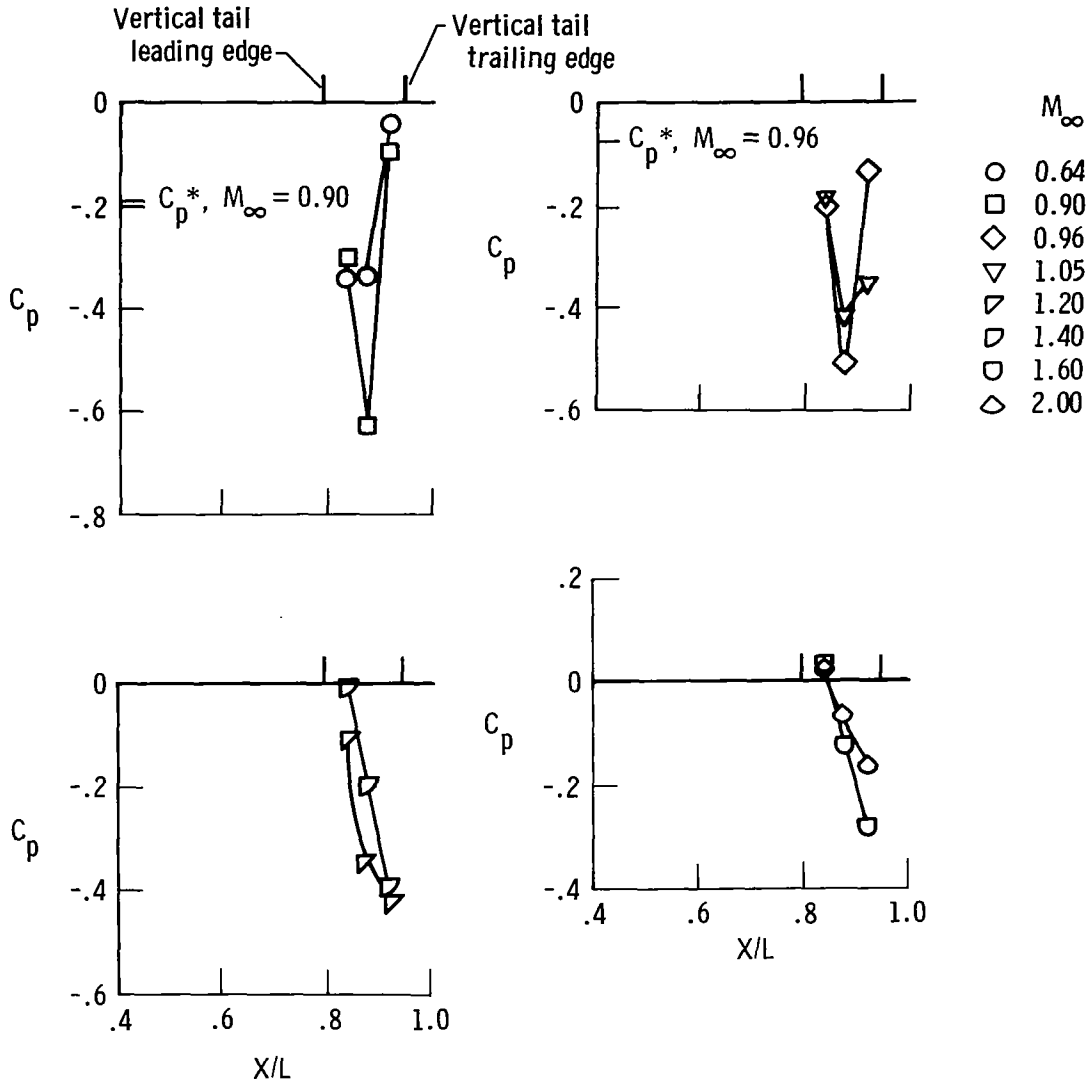

(e) Upper left tail boom.

Figure 19. Concluded.

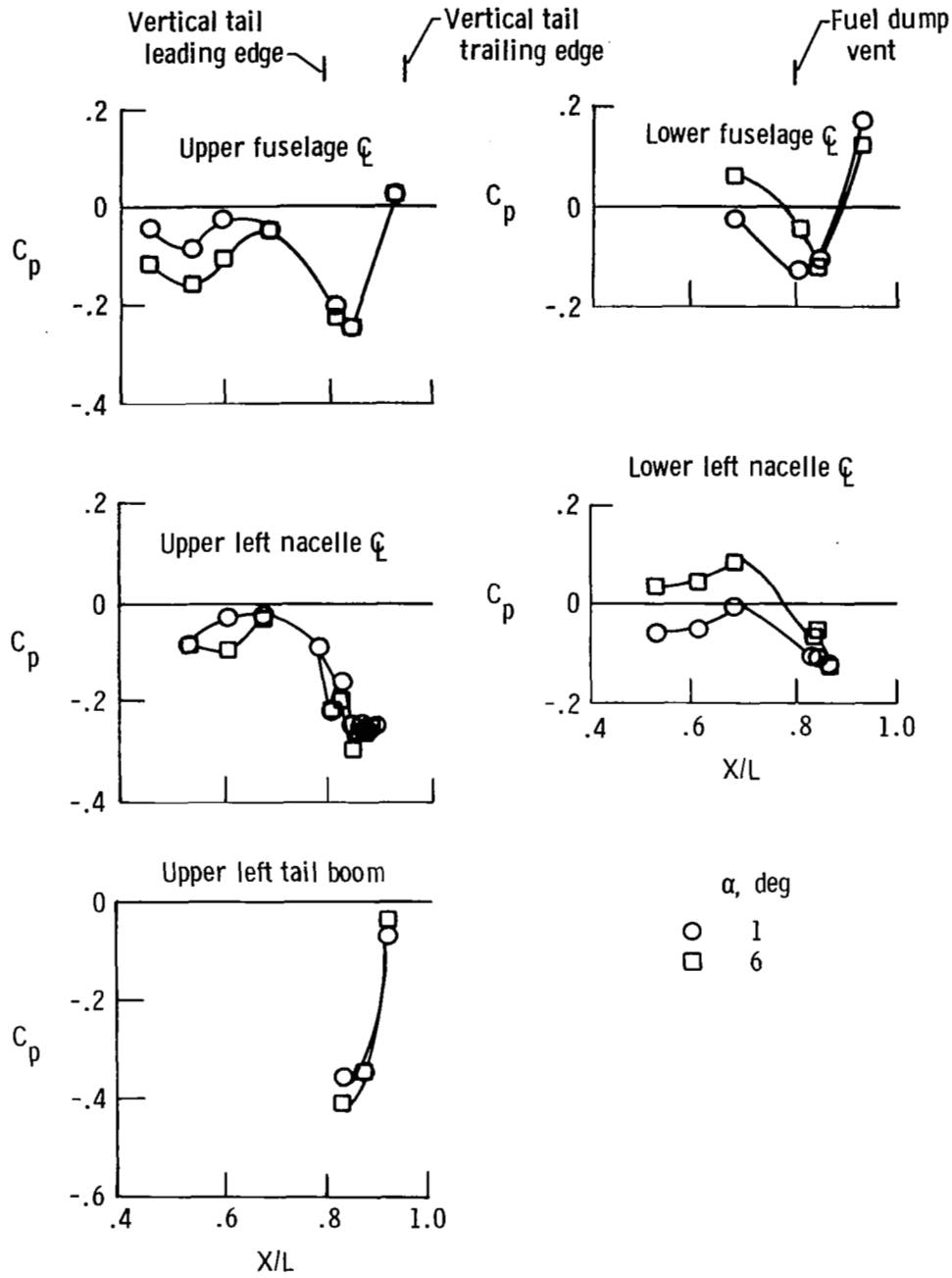

(a) Angle of attack change from 1° to 6°. $M_\infty \approx 0.60$; BTL = MIL; BTR = MIL; h_p = 10,500 m; $\beta \approx 0°$; $\rho = 0°$; bypass door closed.

Figure 20. Effect of angle of attack on aft fuselage pressure coefficients.

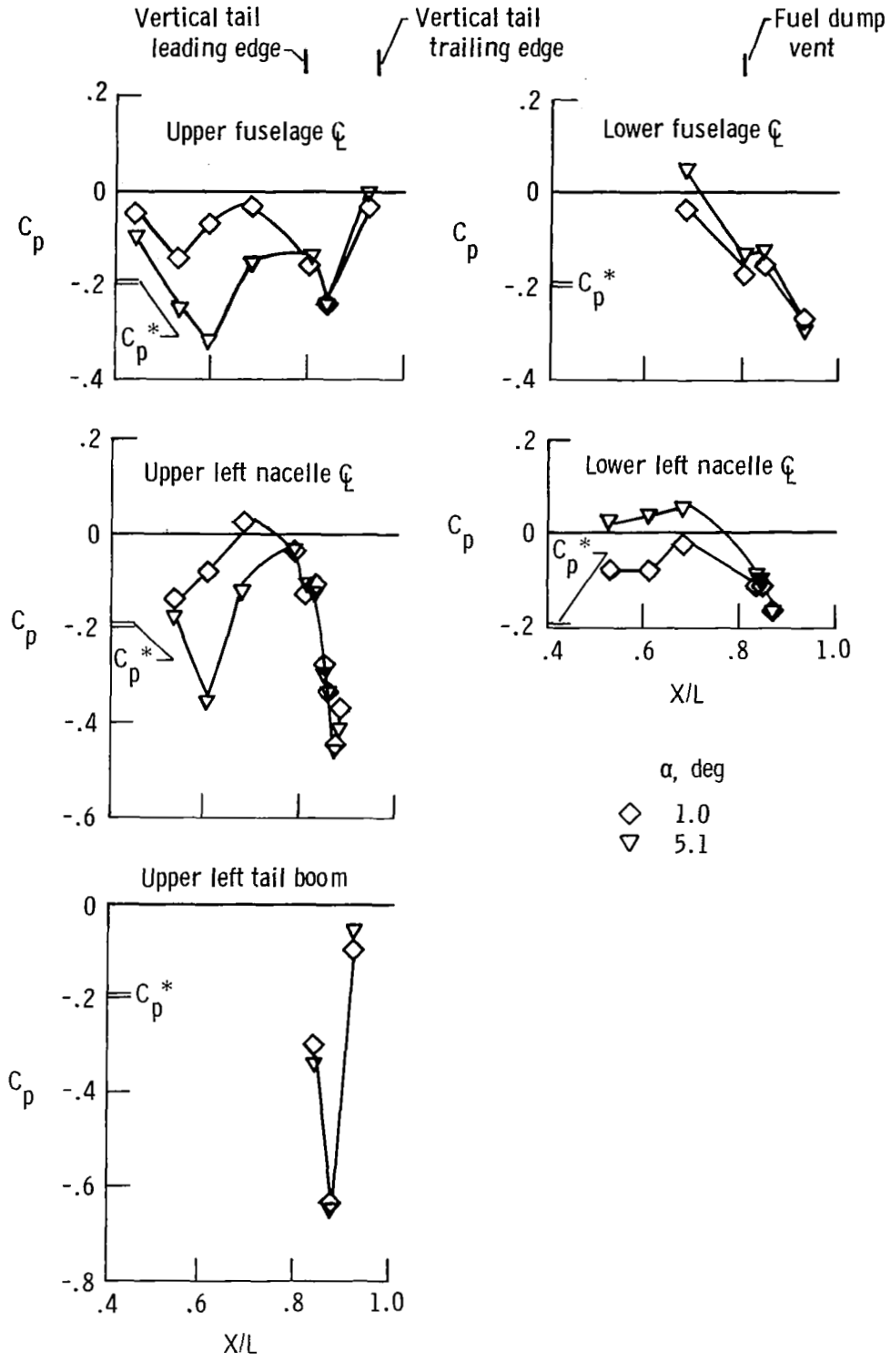

(b) Angle of attack change from 1° to 5°. $M_\infty \approx 0.90$; BTL = MIL; BTR = MIL and 10.4°; h_p = 10,700 m; β = 0°; ρ = 0°; bypass door closed.

Figure 20. Continued.

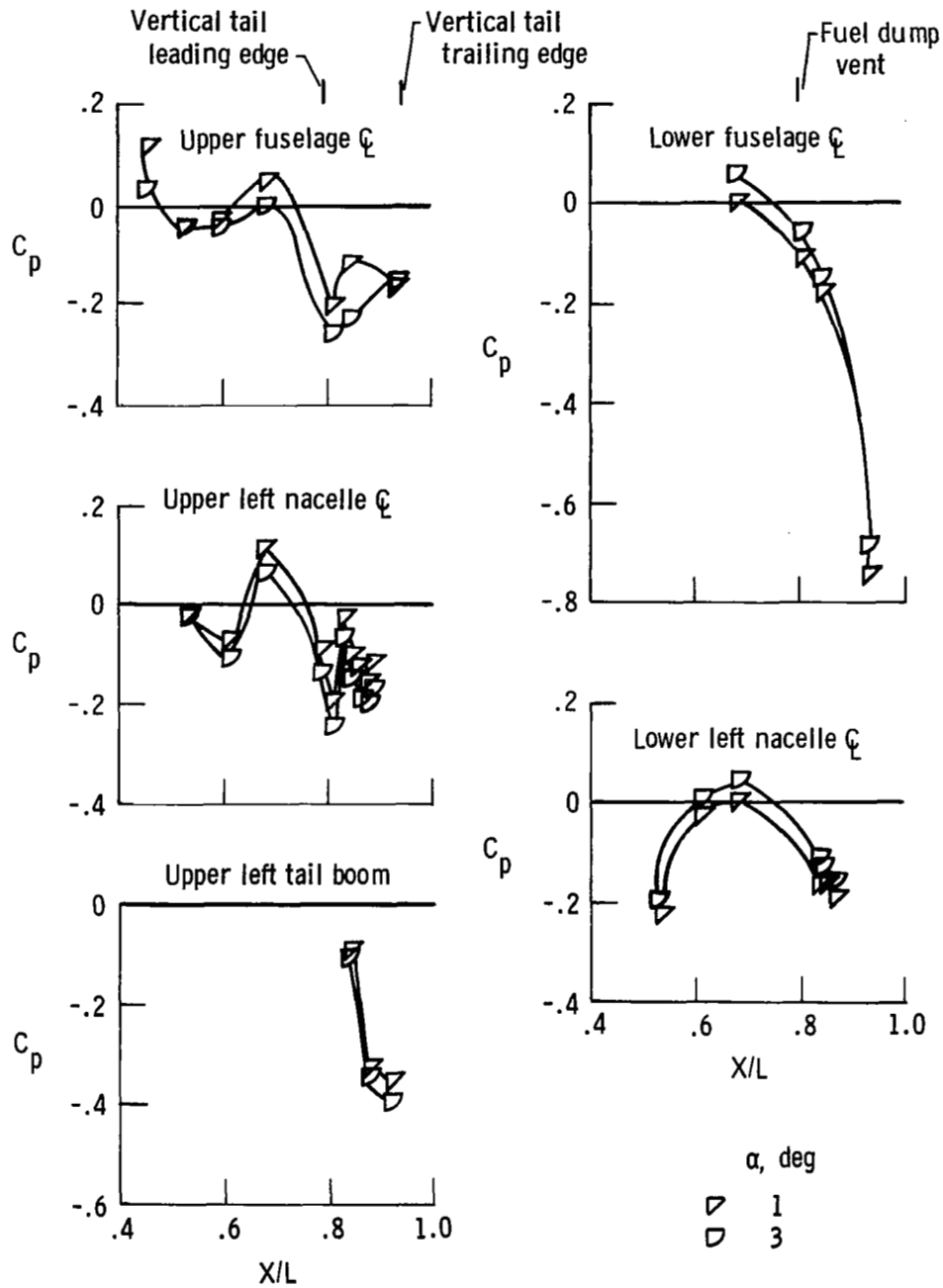

(c) Angle of attack change from 1° to 3°. M_∞ = 1.20; BTL = 9.2°; BTR ≈ 13.3°; h_p = 10,900 m; β = −0.3°; ρ = 0°; bypass door closed.

Figure 20. Concluded.

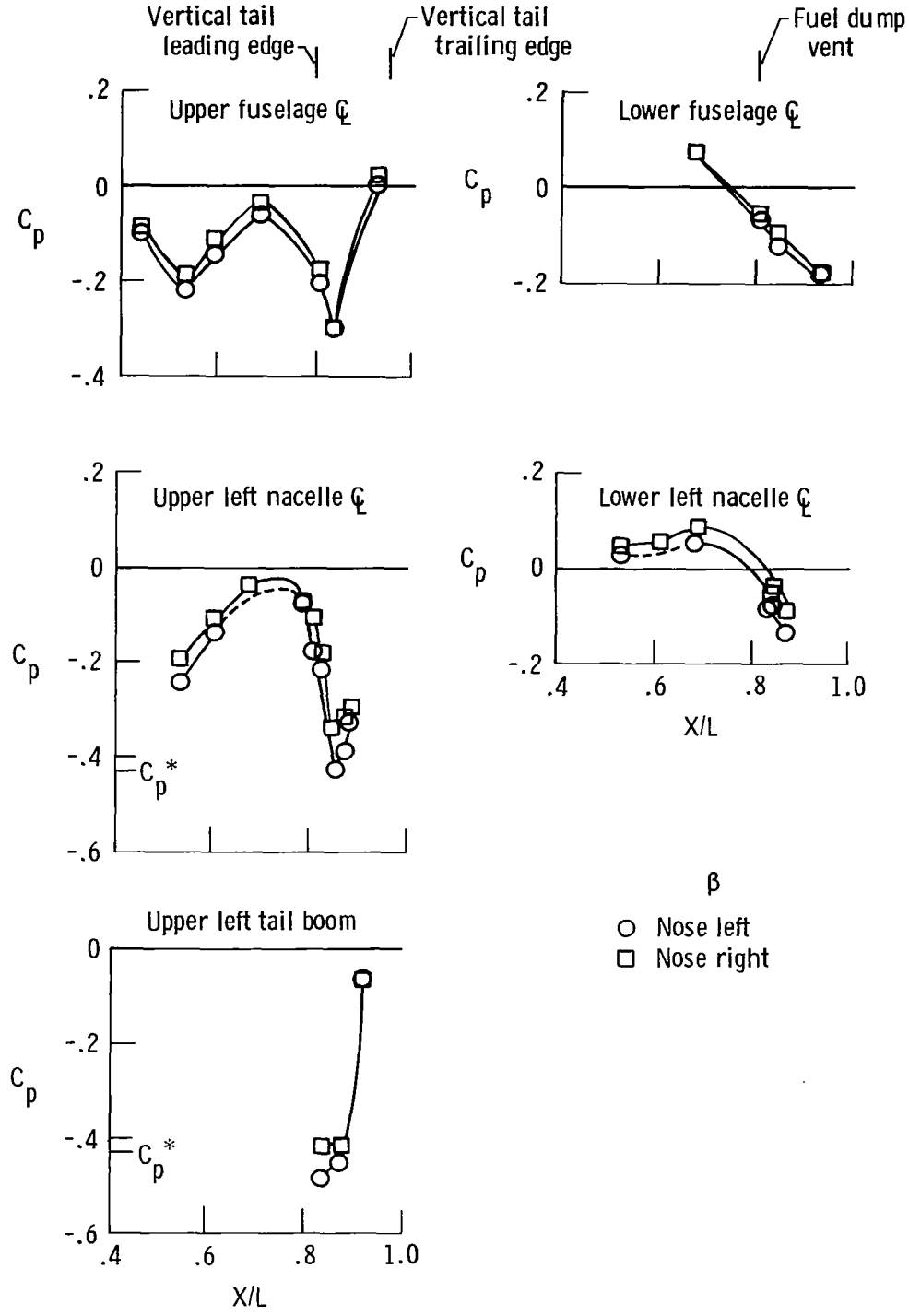

Figure 21. Effect of angle of sideslip change from 1° airplane nose left to 1° airplane nose right on aft fuselage pressure coefficients. $M_\infty = 0.80$; *BTL = MIL; BTR = MIL;* $h_p = 13{,}800$ *m;* $\alpha = 5°$; $\rho = 0°$; *bypass door closed.*

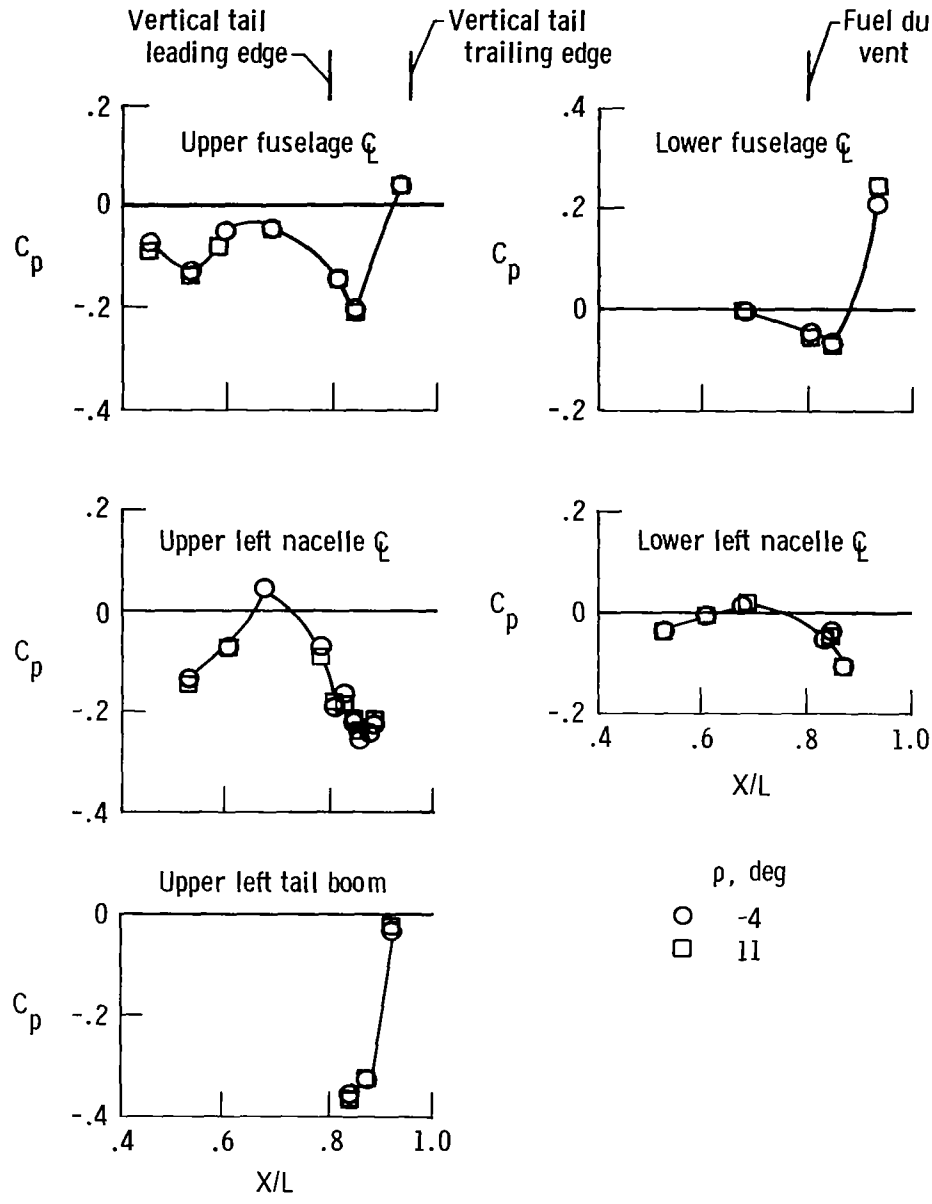

(a) $M_\infty = 0.59$; *BTL = MIL; BTR = MIL;* $h_p = 6300$ *m;* $\alpha \approx 0.3°$; $\beta \approx -0.3°$; *bypass door closed.*

Figure 22. Effect of cowl angle change on aft fuselage pressure coefficients.

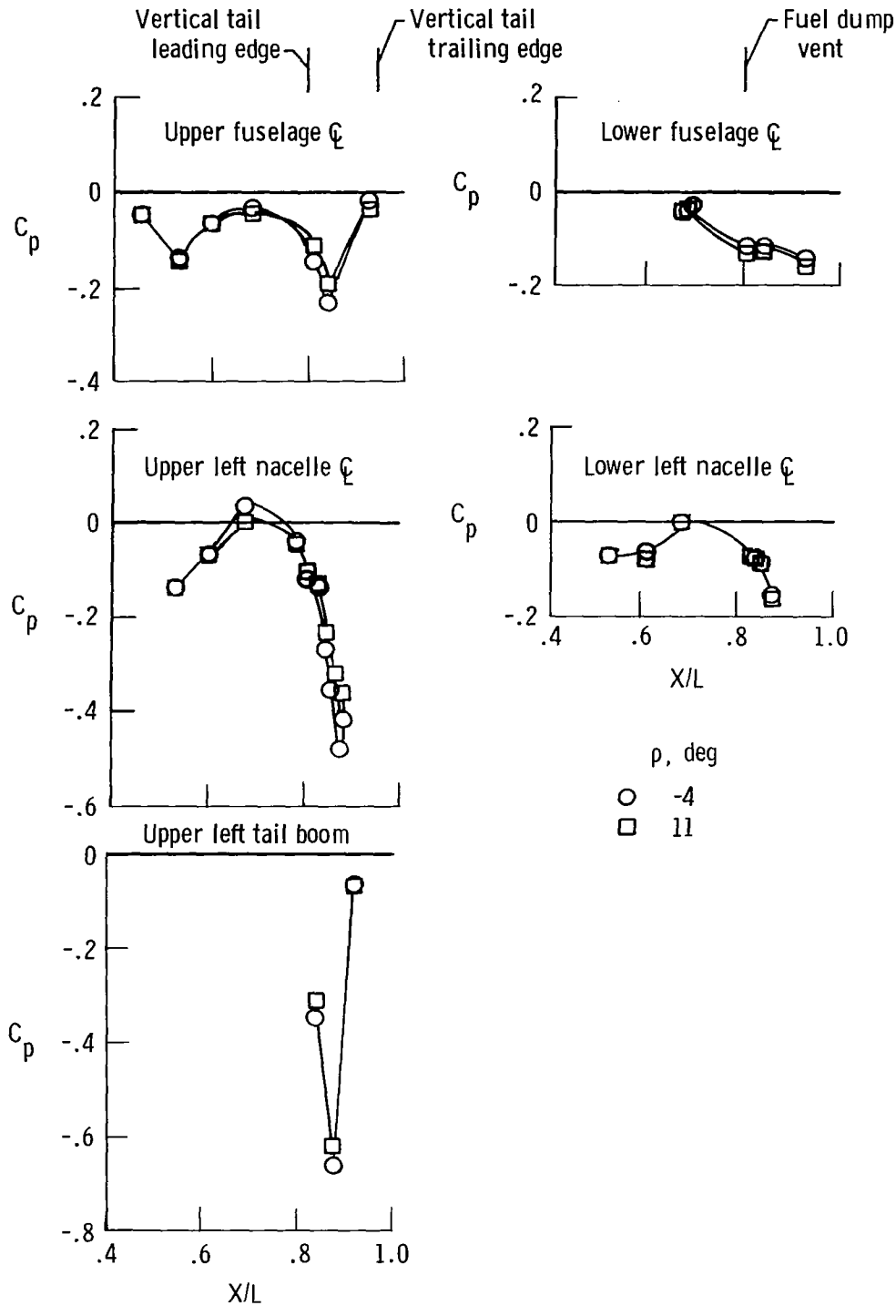

(b) M_∞ *= 0.89; BTL = MIL; BTR = MIL;* h_p *= 6400 m;* α *= 1°;* β *= -0.3°; bypass door closed.*

Figure 22. Concluded.

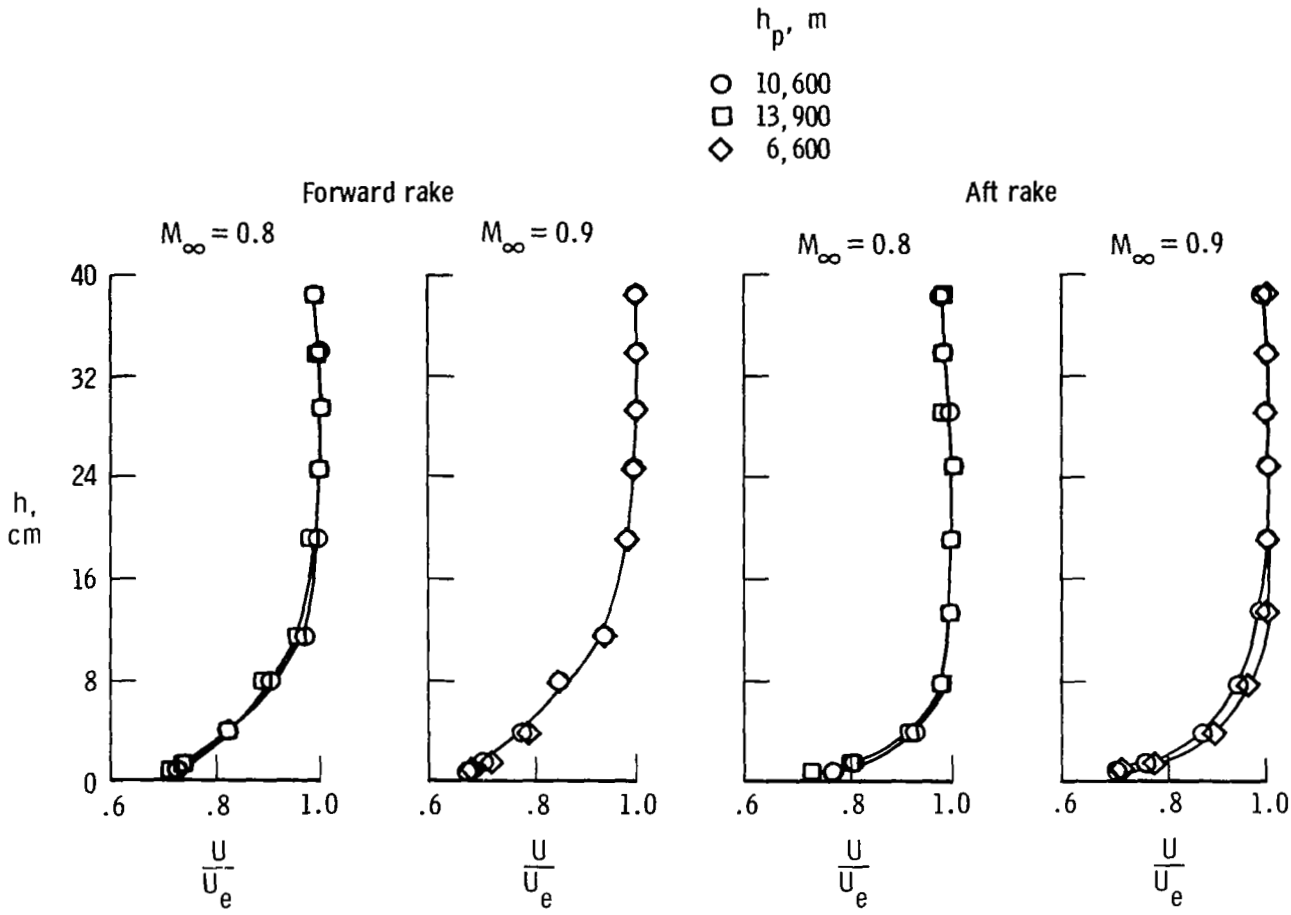

Figure 23. Effect of altitude on boundary layer velocity ratio. α = 2.1° to 3.1°.

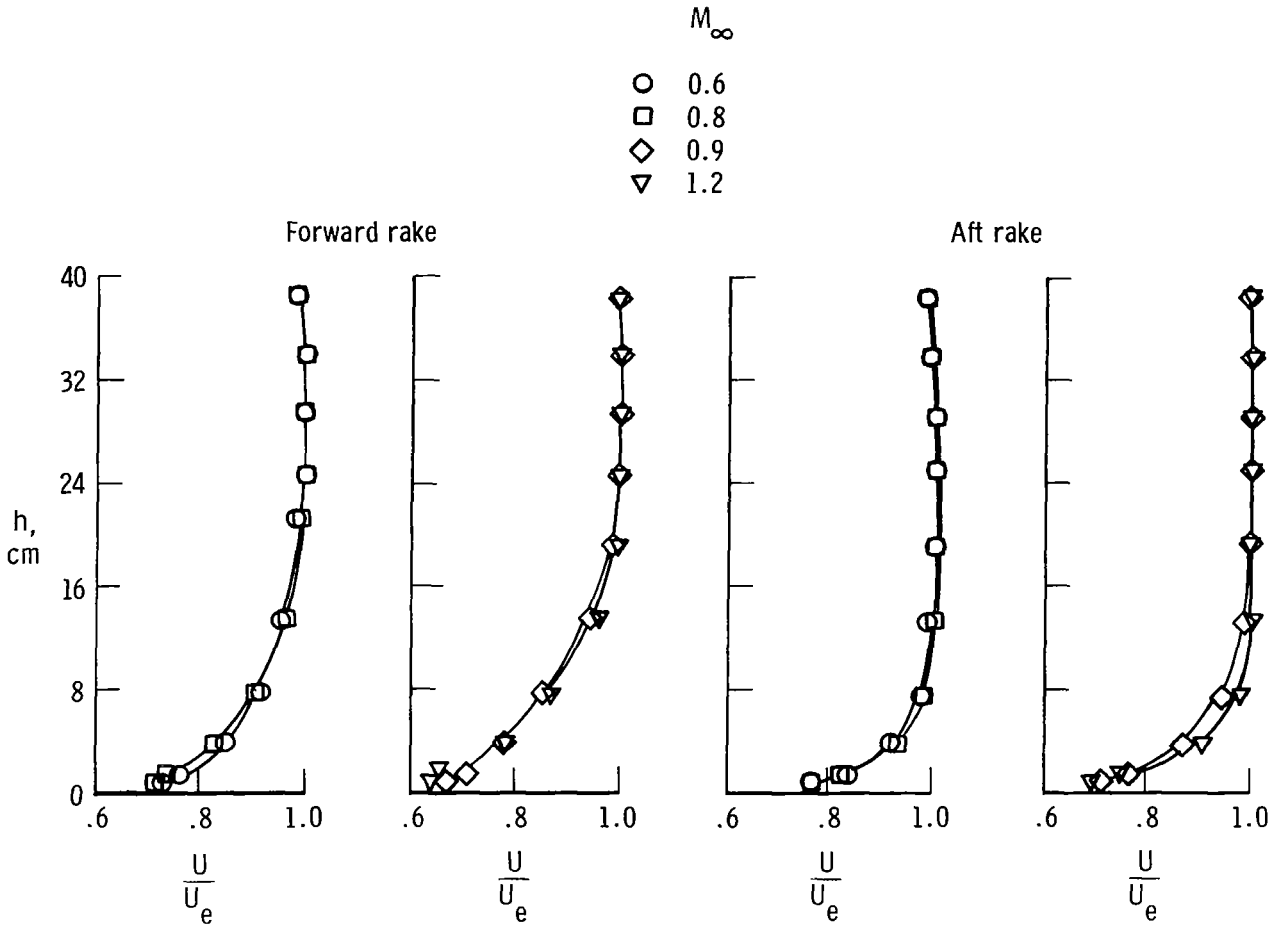

Figure 24. Effect of Mach number on boundary layer velocity ratio. h_p = 10,600 m and 13,900 m; α = 2.5° to 3.5°.

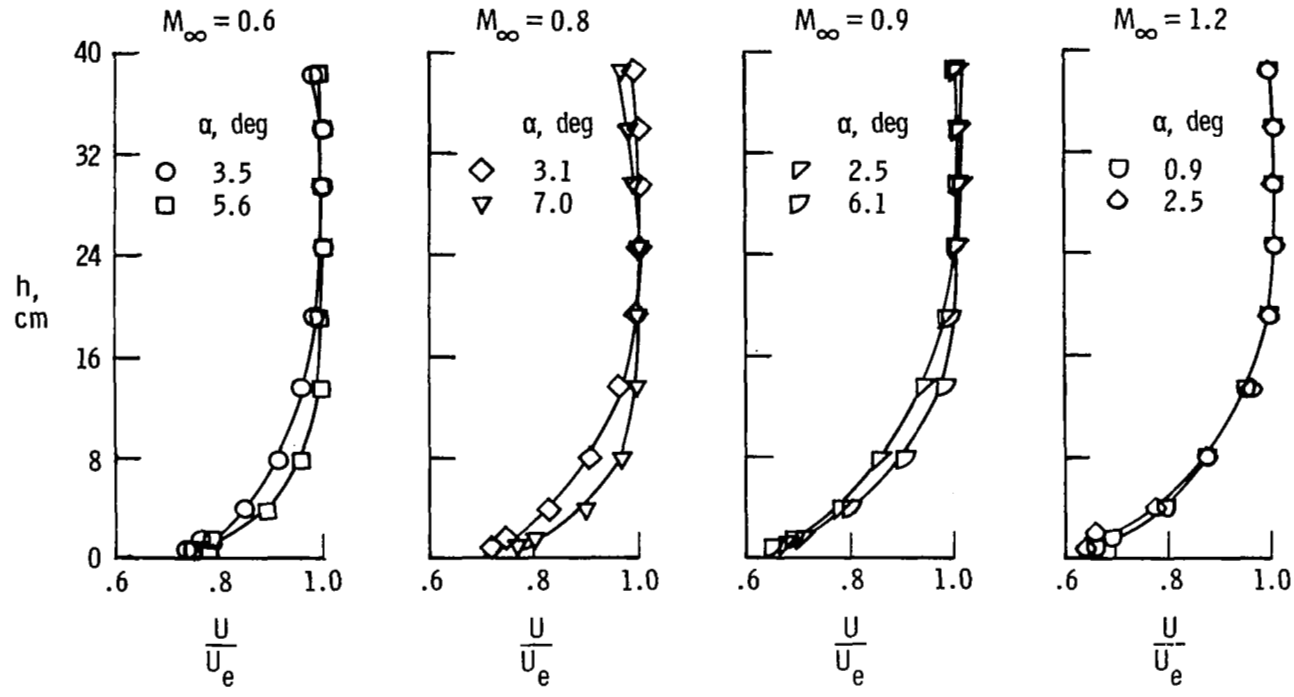

(a) Forward rake.

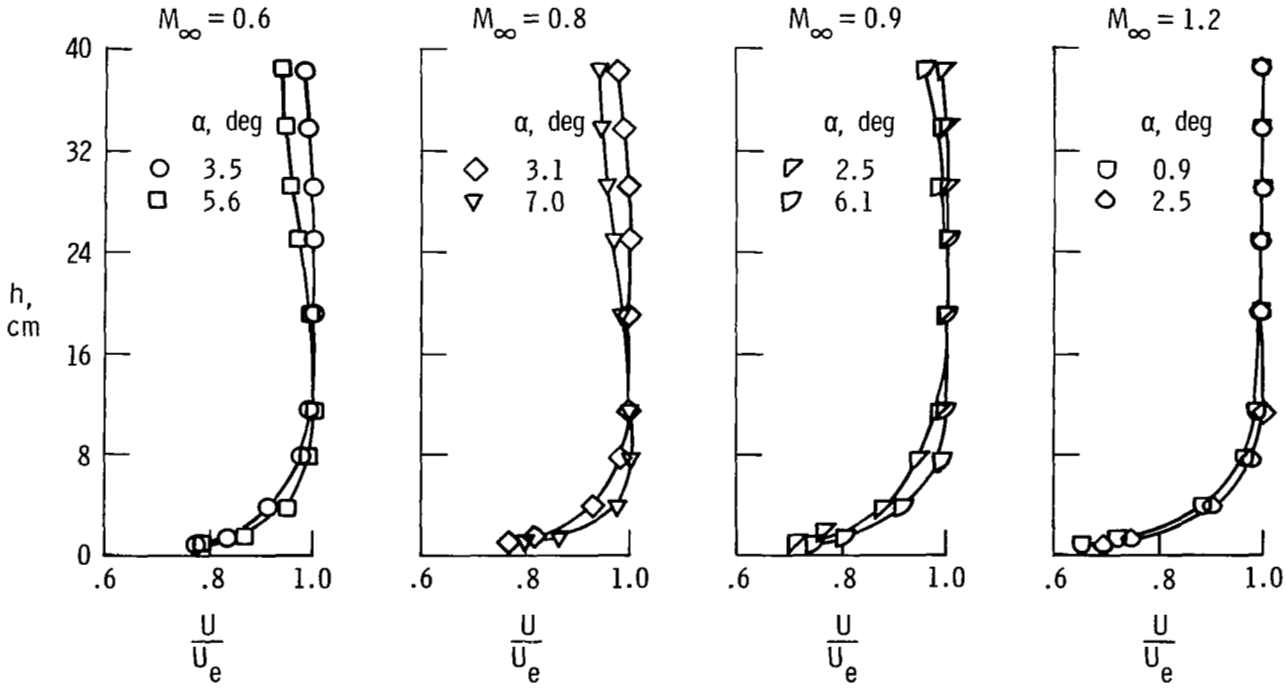

(b) Aft rake.

Figure 25. Effect of angle of attack on boundary layer velocity ratio. h_p = 10,600 m and 13,900 m.

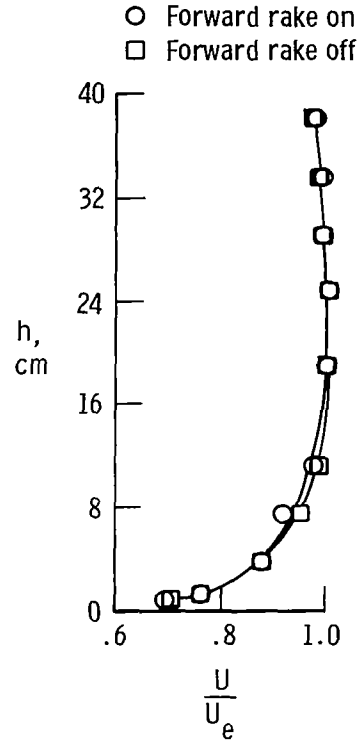

Figure 26. Effect of forward rake on aft rake velocity ratio. M_∞ = 0.90; α = 3.2° to 3.5°.

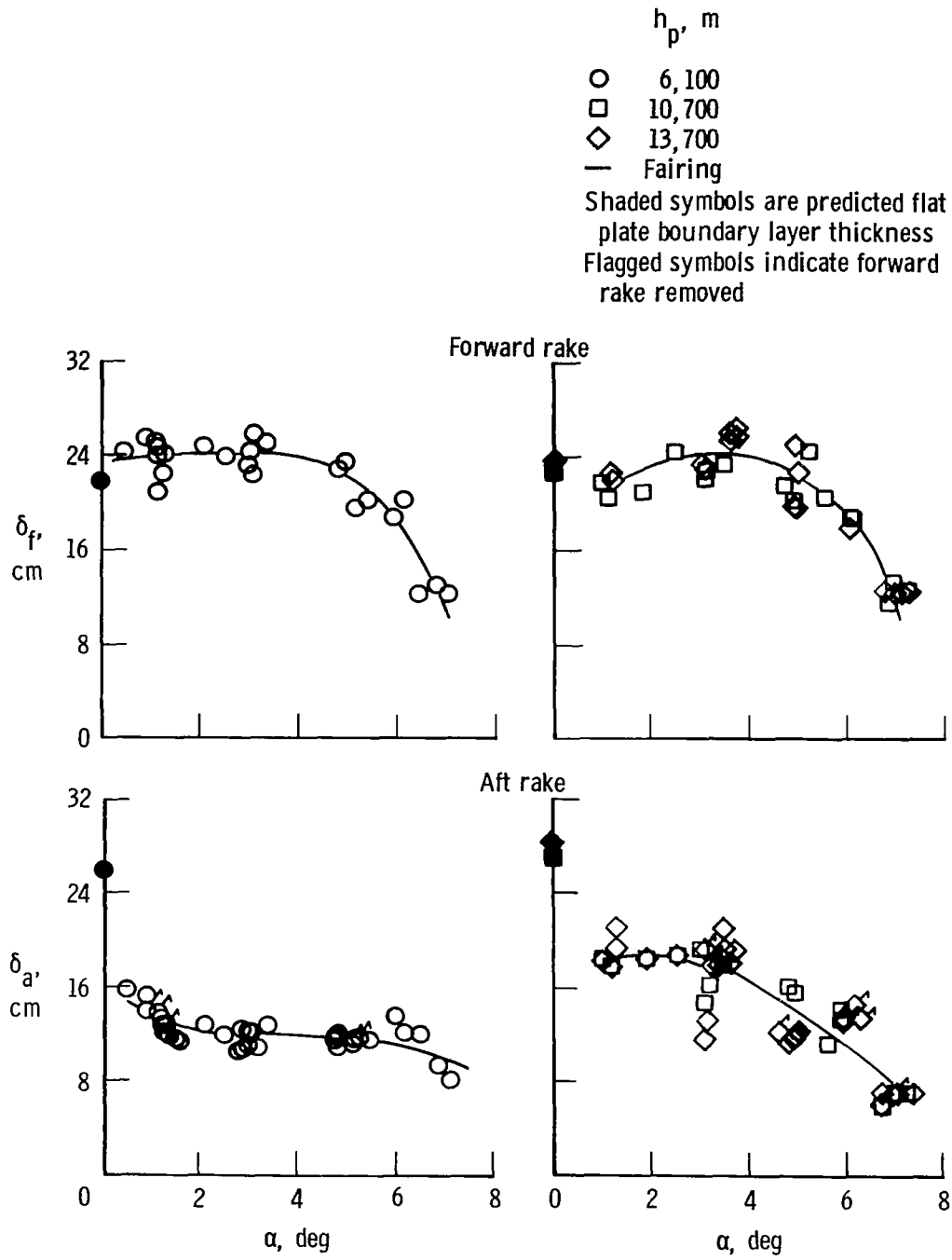

(a) Subsonic Mach numbers.

Figure 27. Variation of boundary layer thickness with Mach number, altitude, and angle of attack.

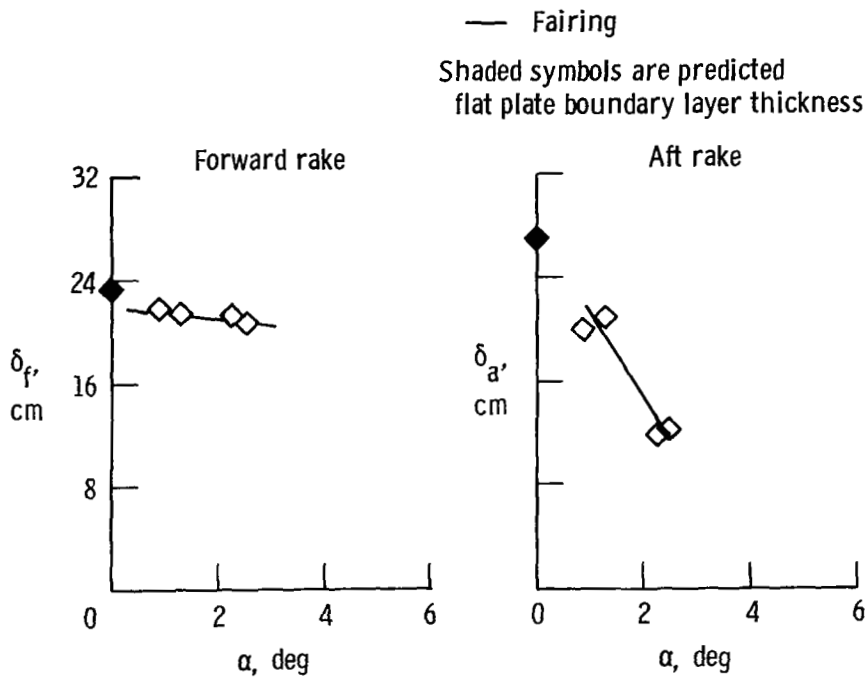

(b) $M_\infty = 1.20$; $h_p = 13,700\ m$.

Figure 27. Concluded.

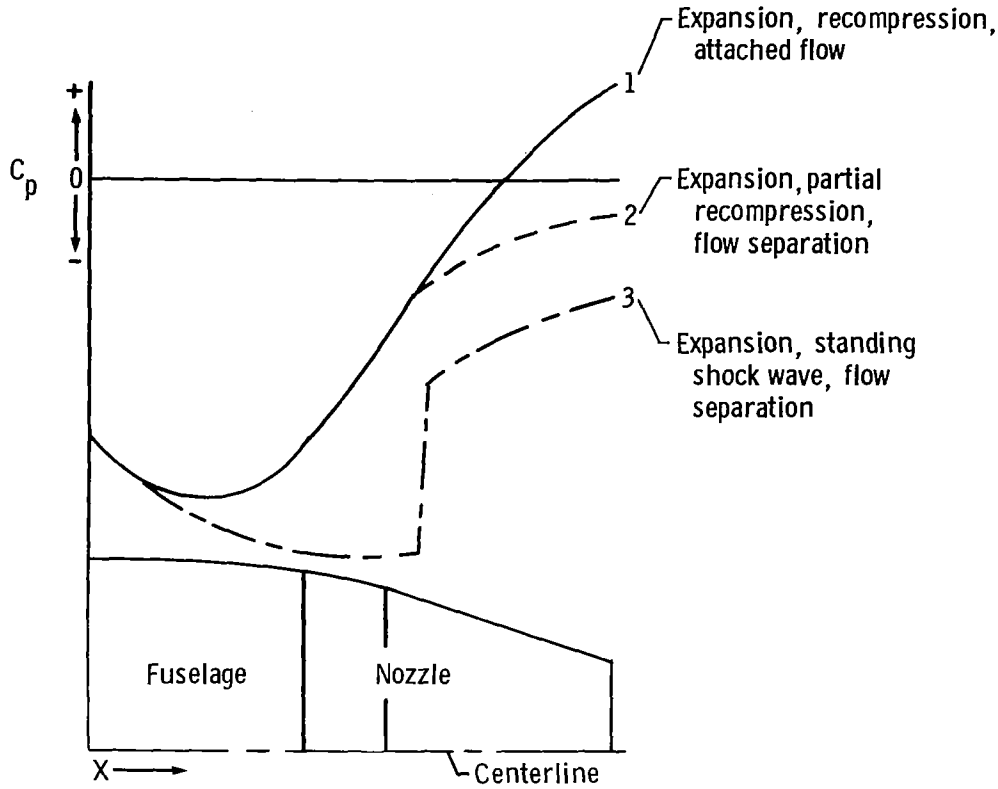

Figure 28. External pressure profiles that can occur on an isolated idealized nozzle.

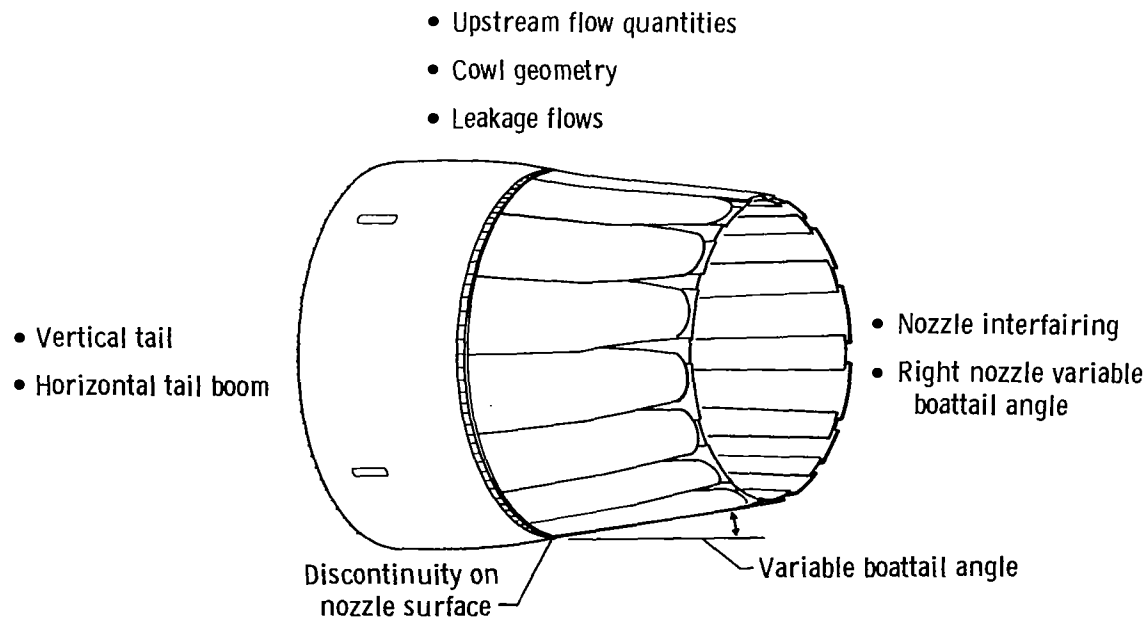

Figure 29. Factors that affect pressures on left nozzle.

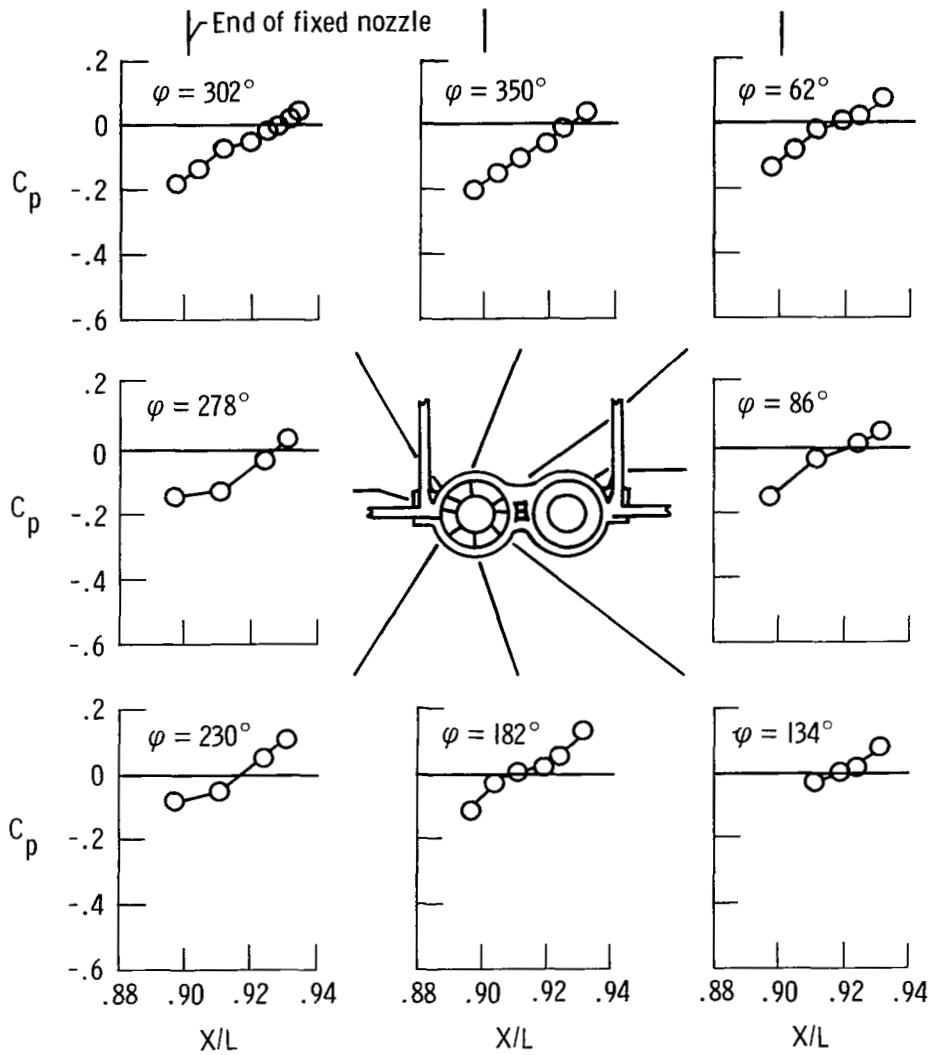

Figure 30. Nozzle pressure coefficients for M_∞ = 0.90; BTL = 10.5°; BTR = MIL; h_p = 10,600 m; α = 2°; β = -0.3°; ρ = 0°; bypass door closed.

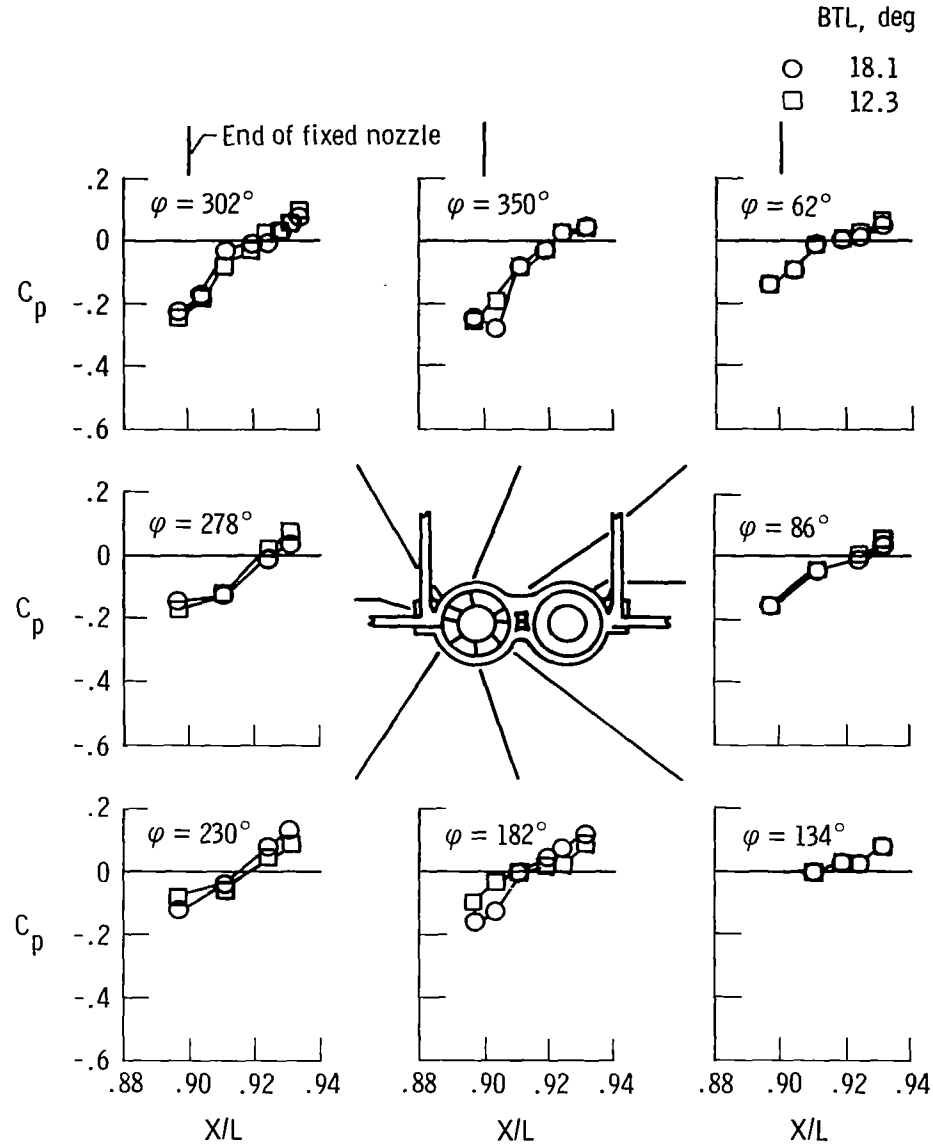

(a) *BTL change from 18.1° to 12.3°.* M_∞ *= 0.61;* h_p *= 10,600 m;* α *= 6°;* β *= −0.1°;* ρ *= 0°; bypass door closed.*

Figure 31. Effect of BTL on left nozzle pressure coefficient. BTR = MIL.

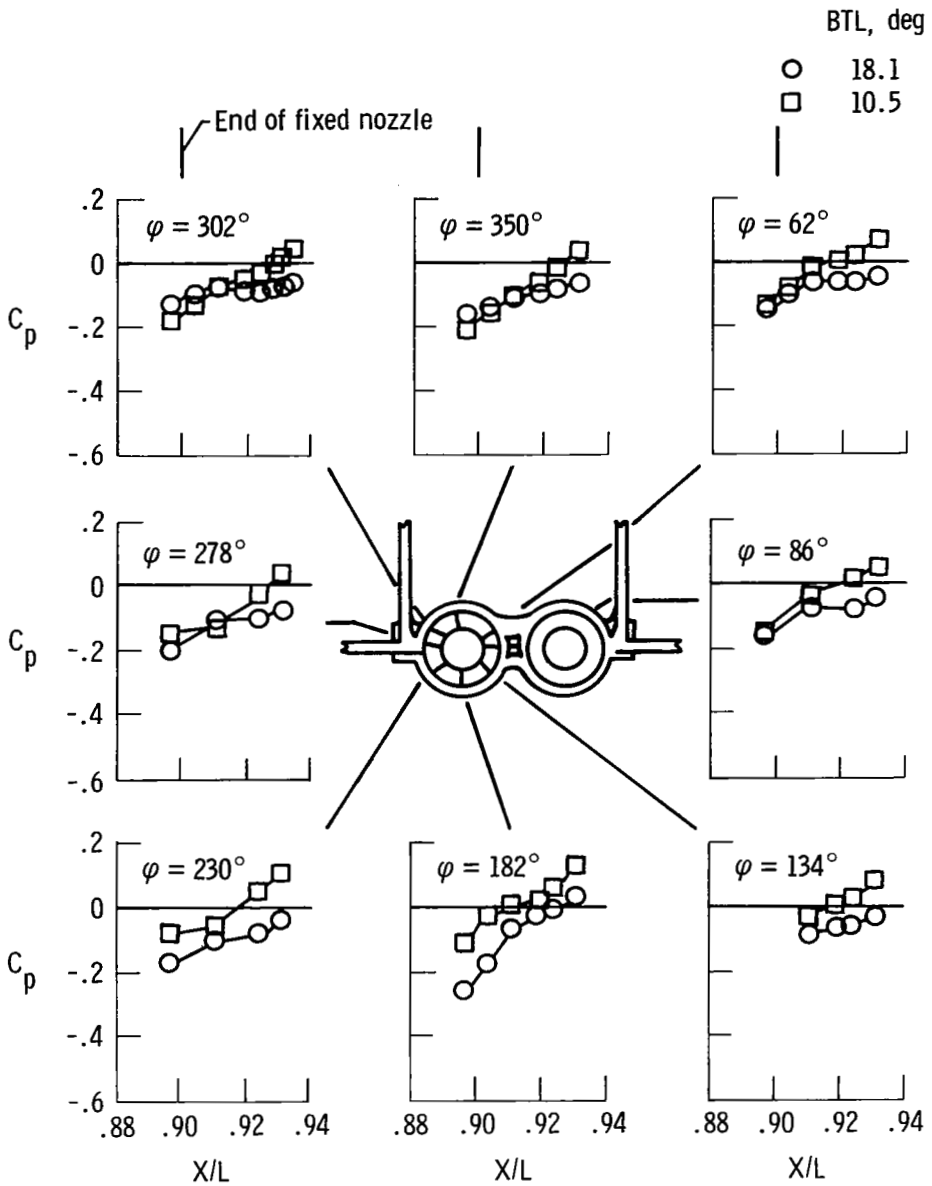

(b) BTL change from 18.1° to 10.5°; M_∞ = 0.90; h_p = 10,600 m; α = 2°; β = −0.3°; ρ = 0°; bypass door closed.

Figure 31. Continued.

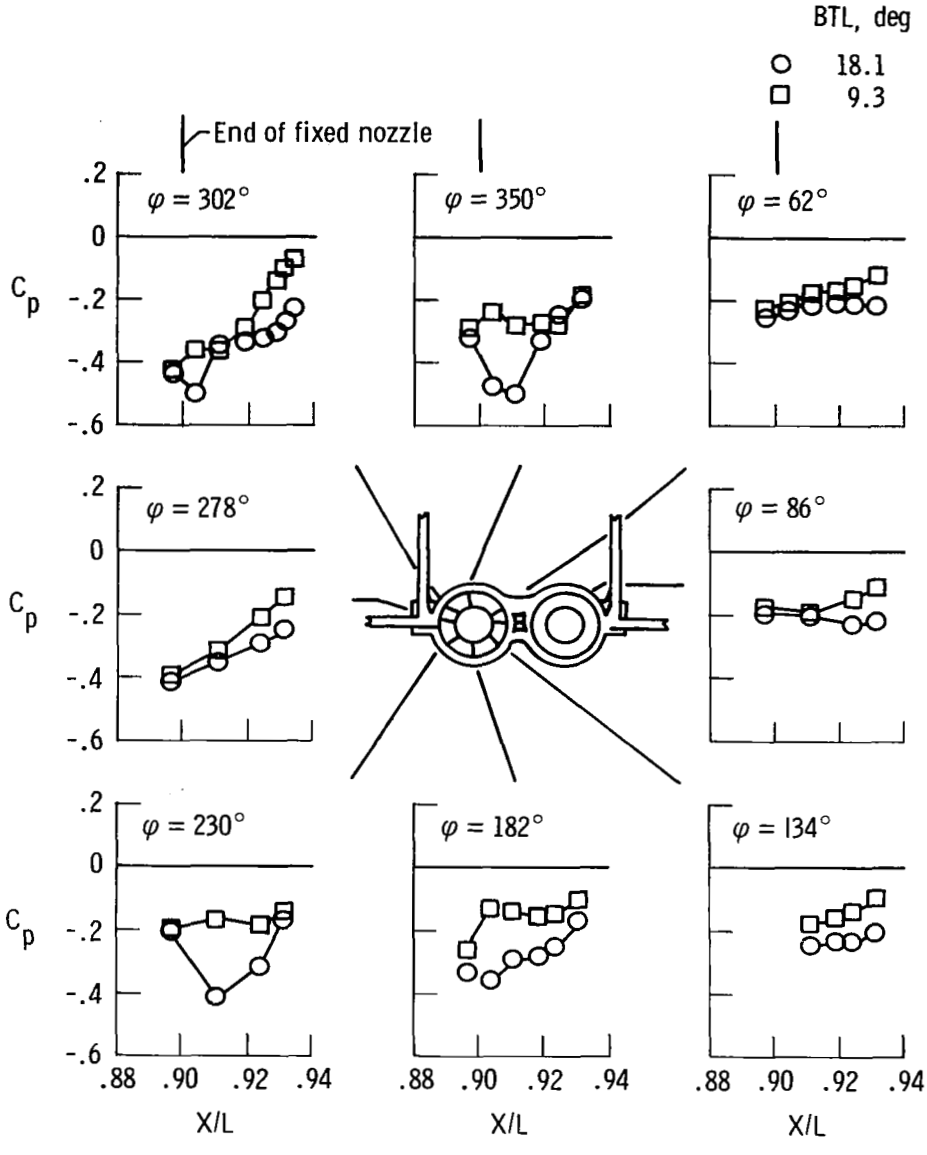

(c) BTL change from 18.1° to 9.3°; M_∞ = 1.20; h_p = 10,700 m; α = 1°; β = -0.4°; ρ = 0°; bypass door closed.

Figure 31. Concluded.

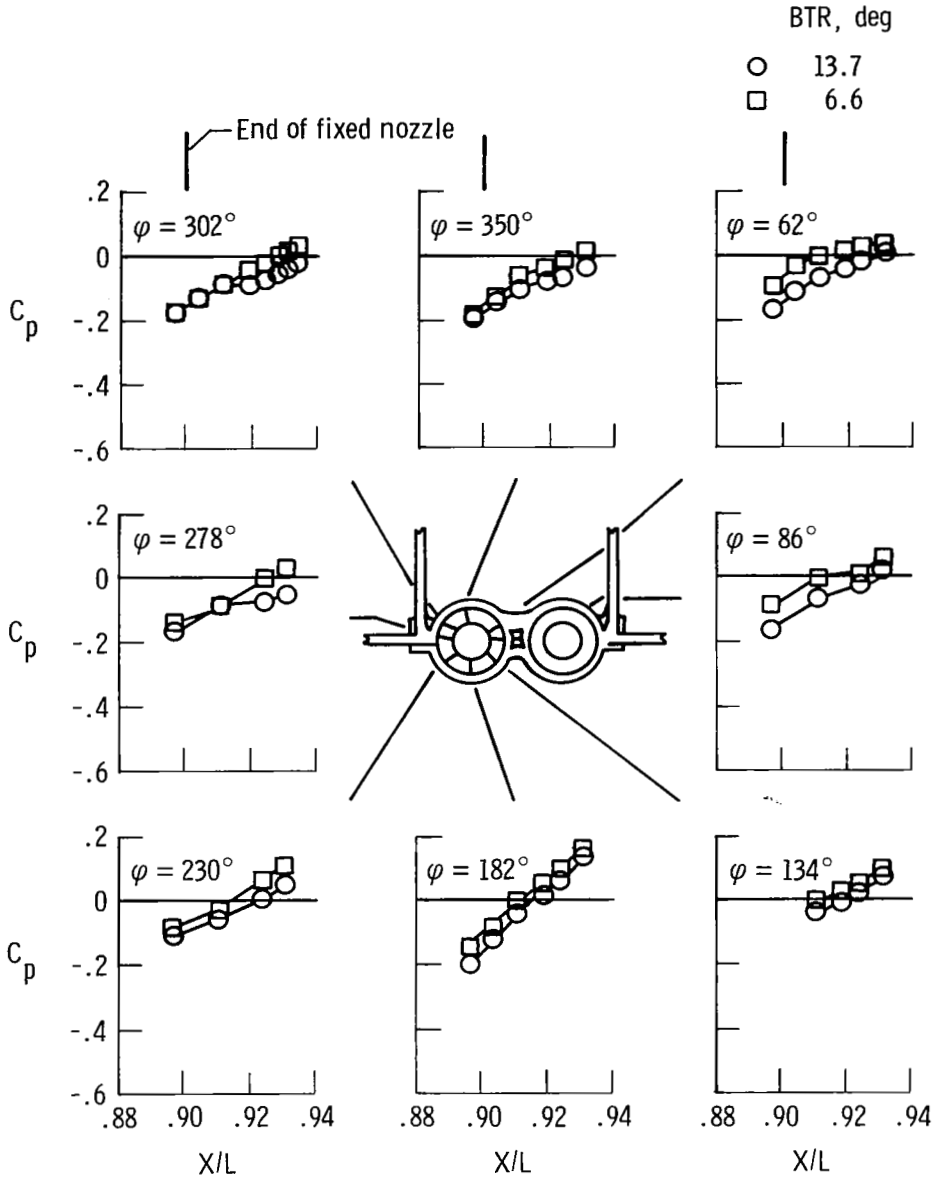

Figure 32. Effect of a BTR change from 13.7° to 6.6° on left nozzle pressure coefficient. $M_\infty = 0.88$; *BTL = 14.8°;* $h_p = 6200$ *m;* $\alpha = 6°$; $\beta = -0.2°$; $\rho = 0°$; *bypass door closed.*

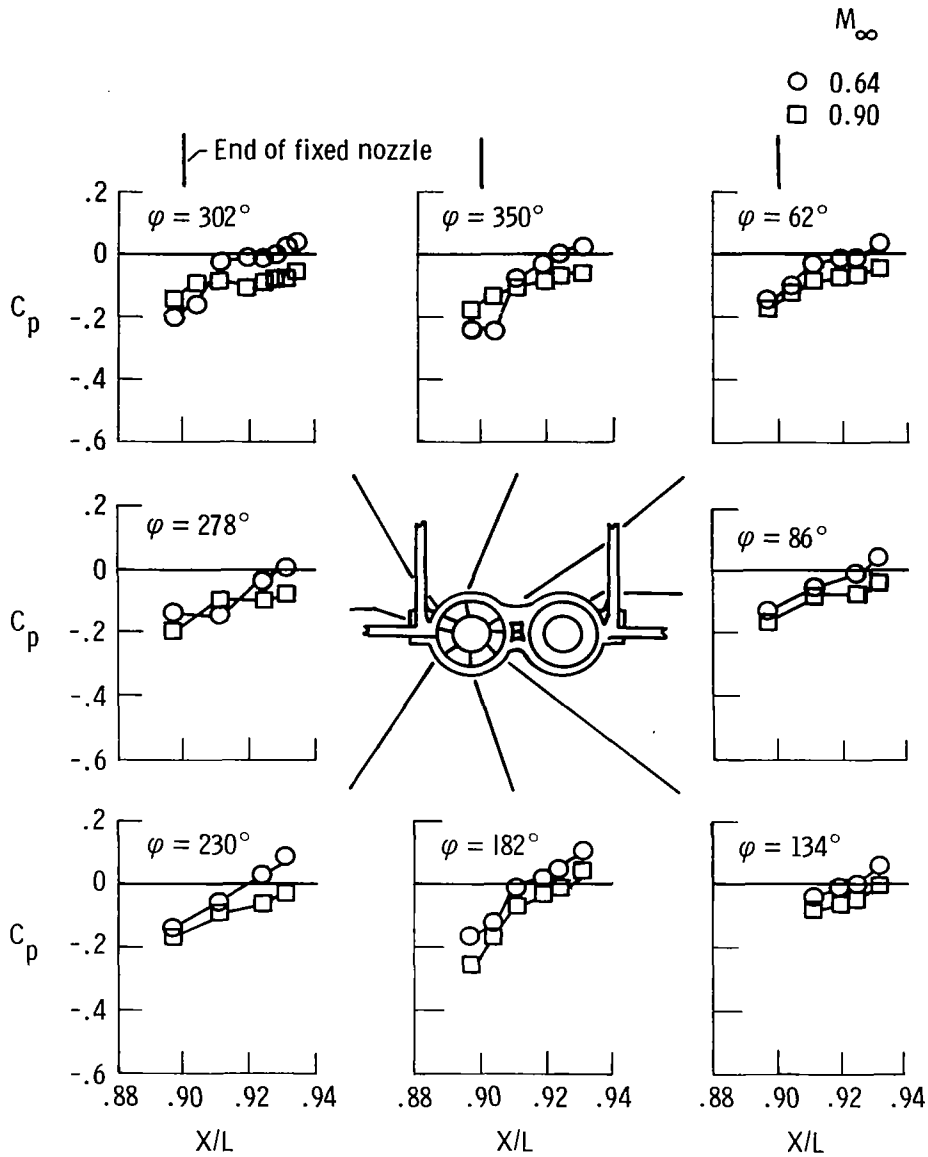

(a) M_∞ = 0.64 and 0.90.

Figure 33. Effect of Mach number on left nozzle pressure coefficient. BTL = MIL; BTR = MIL and 15.0°; h_p = 10,600 m and 13,900 m; α = 1°; β = -0.1°; ρ = 0°; bypass door closed.

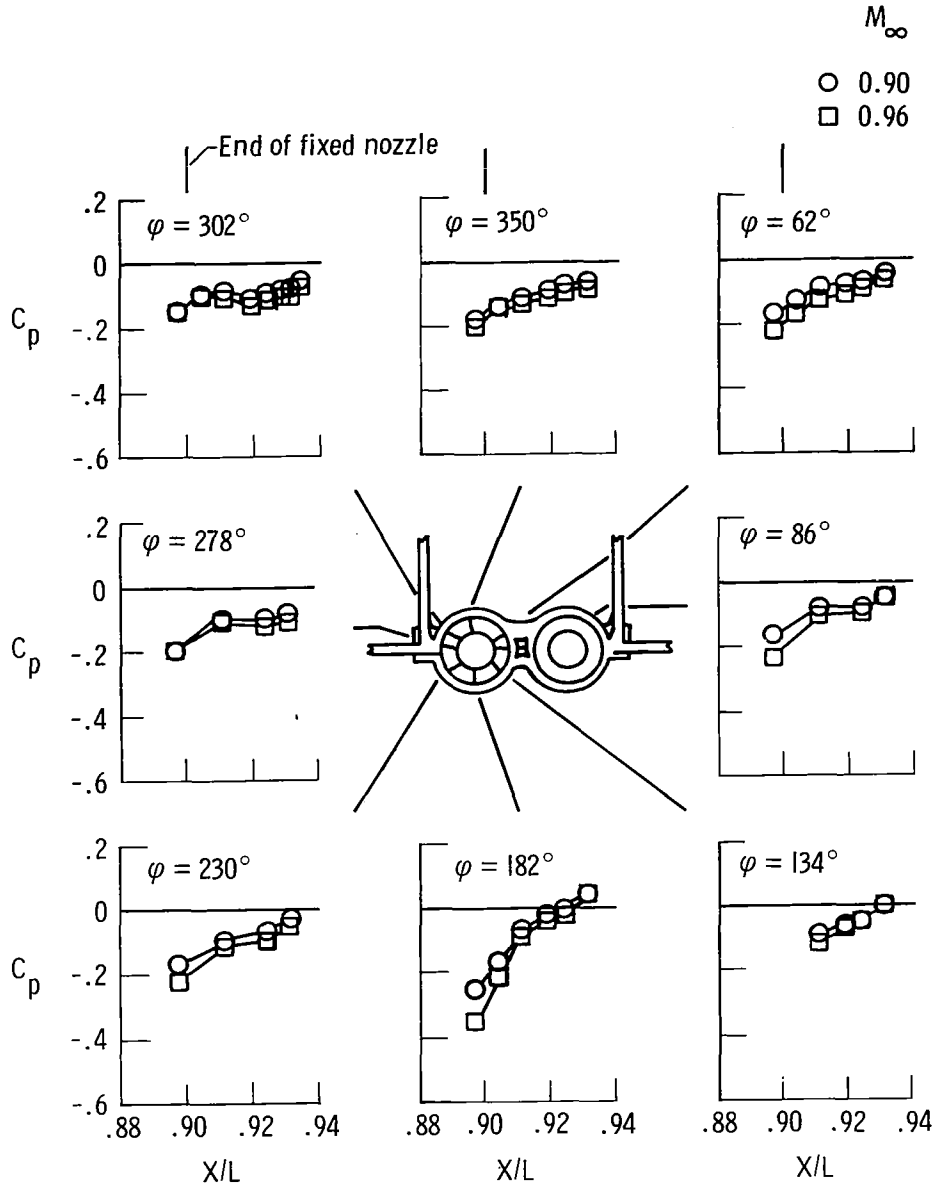

(b) M_∞ = *0.90 and 0.96.*

Figure 33. Continued.

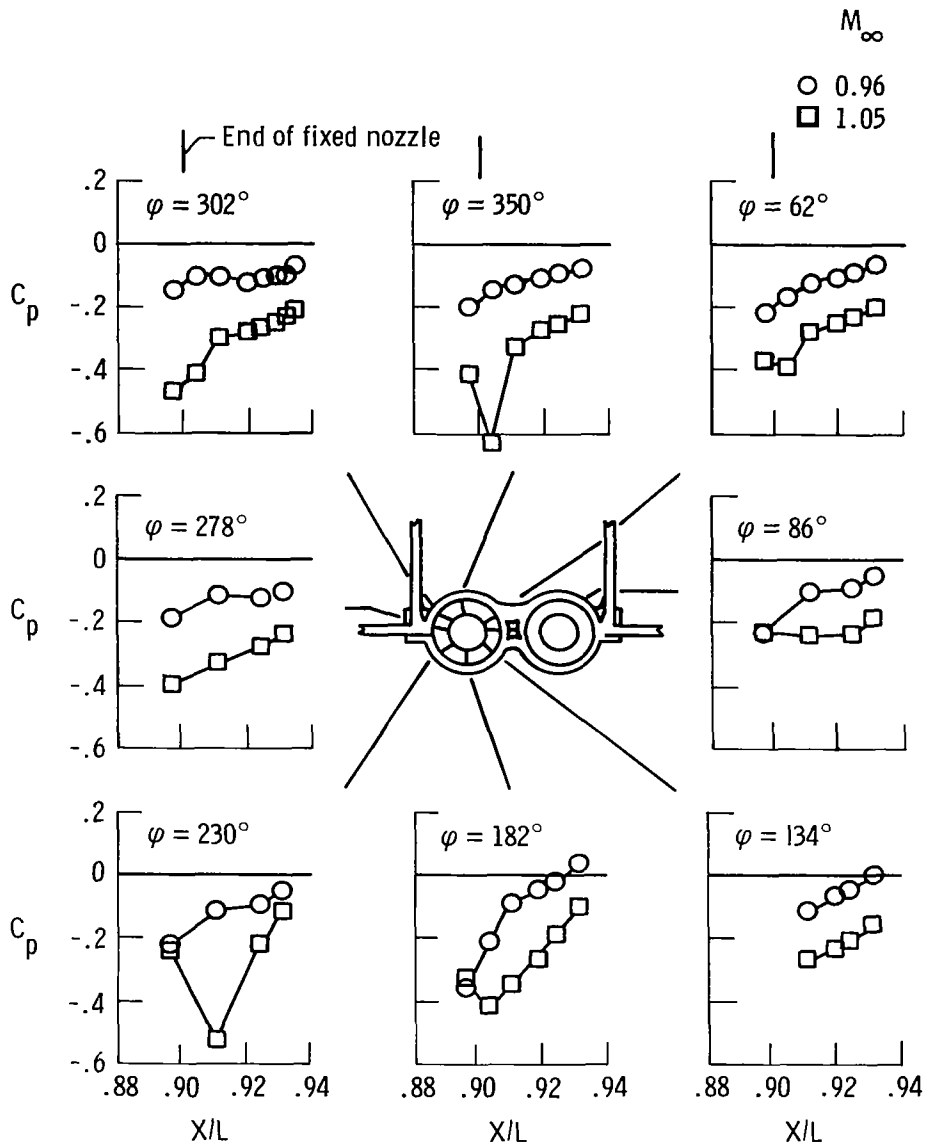

(c) M_∞ = 0.96 and 1.05.

Figure 33. Continued.

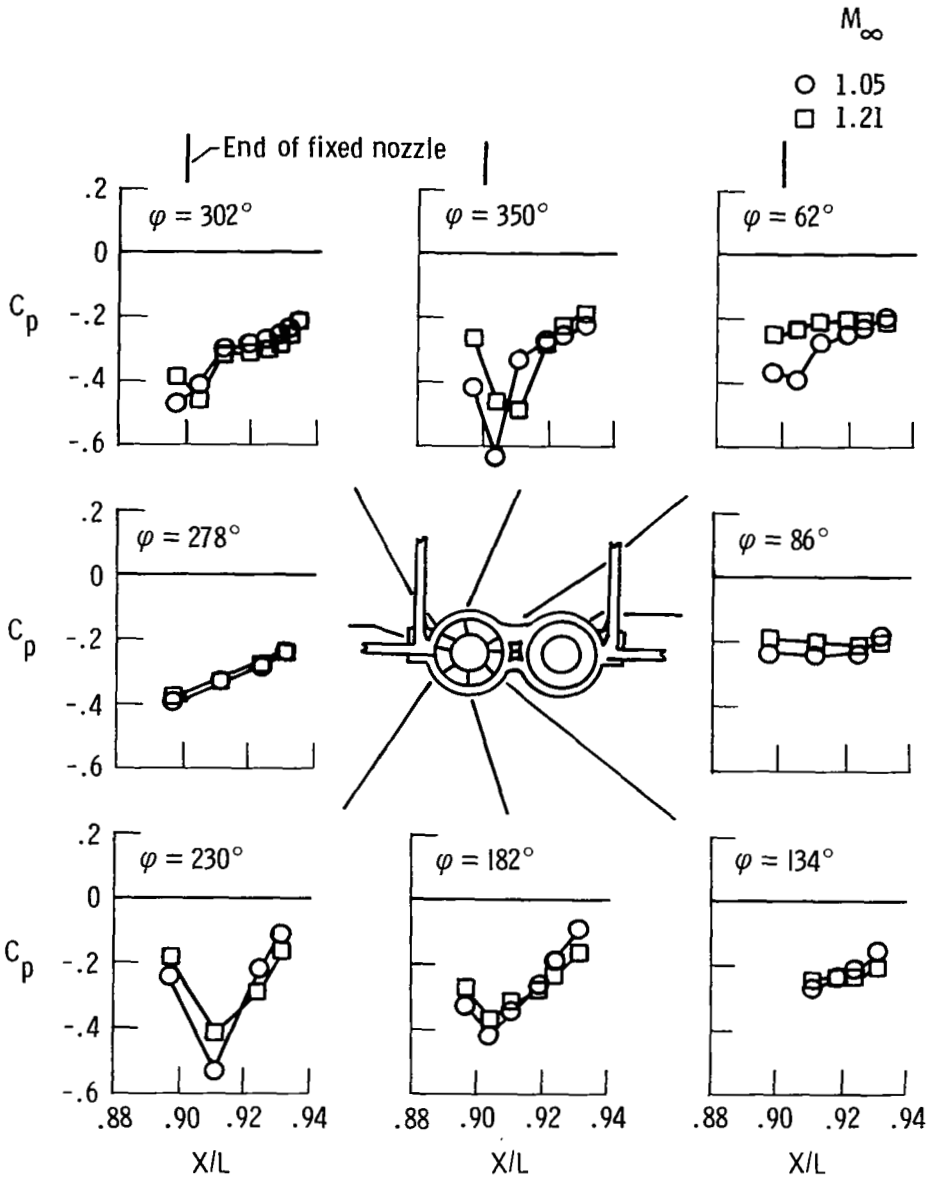

(d) M_∞ = 1.05 and 1.20.

Figure 33. Continued.

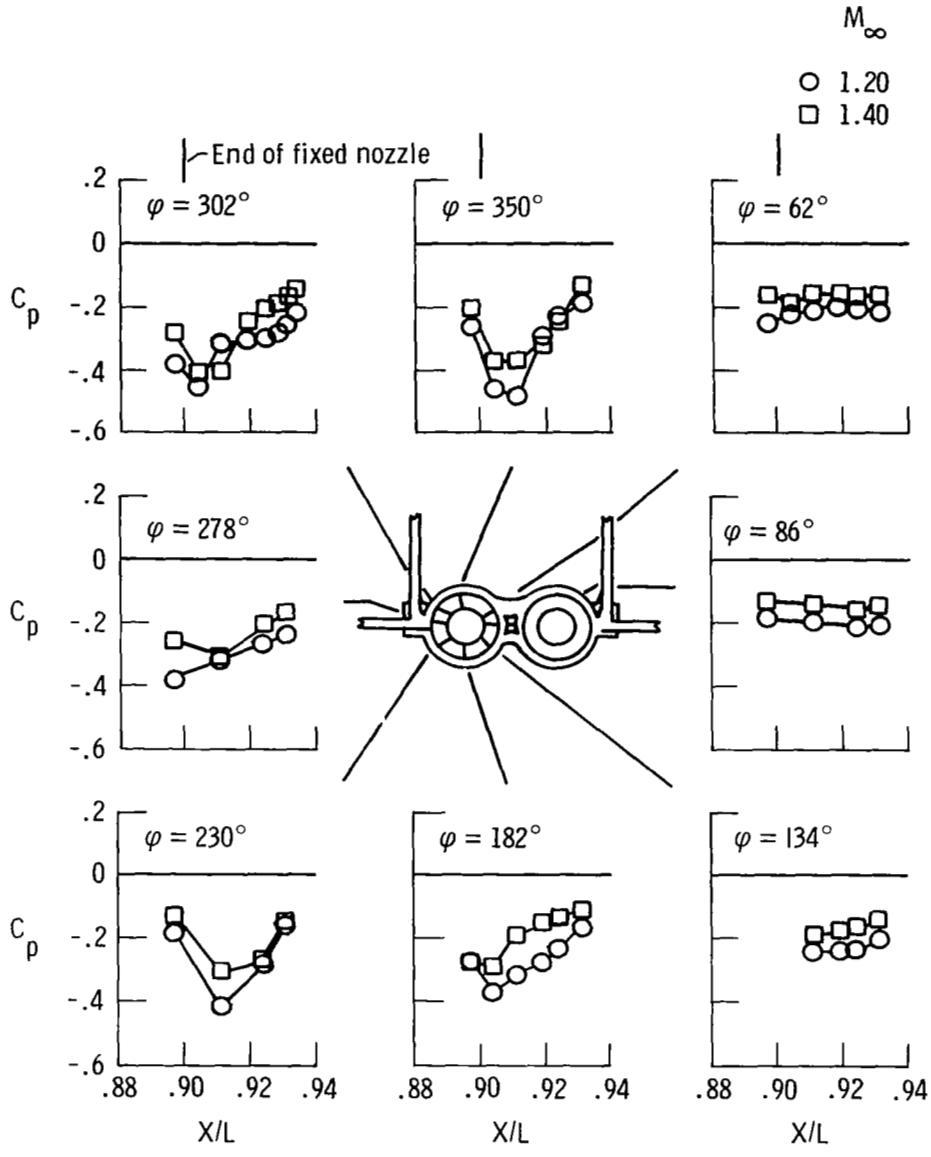

(e) M_∞ = *1.20 and 1.40.*

Figure 33. Continued.

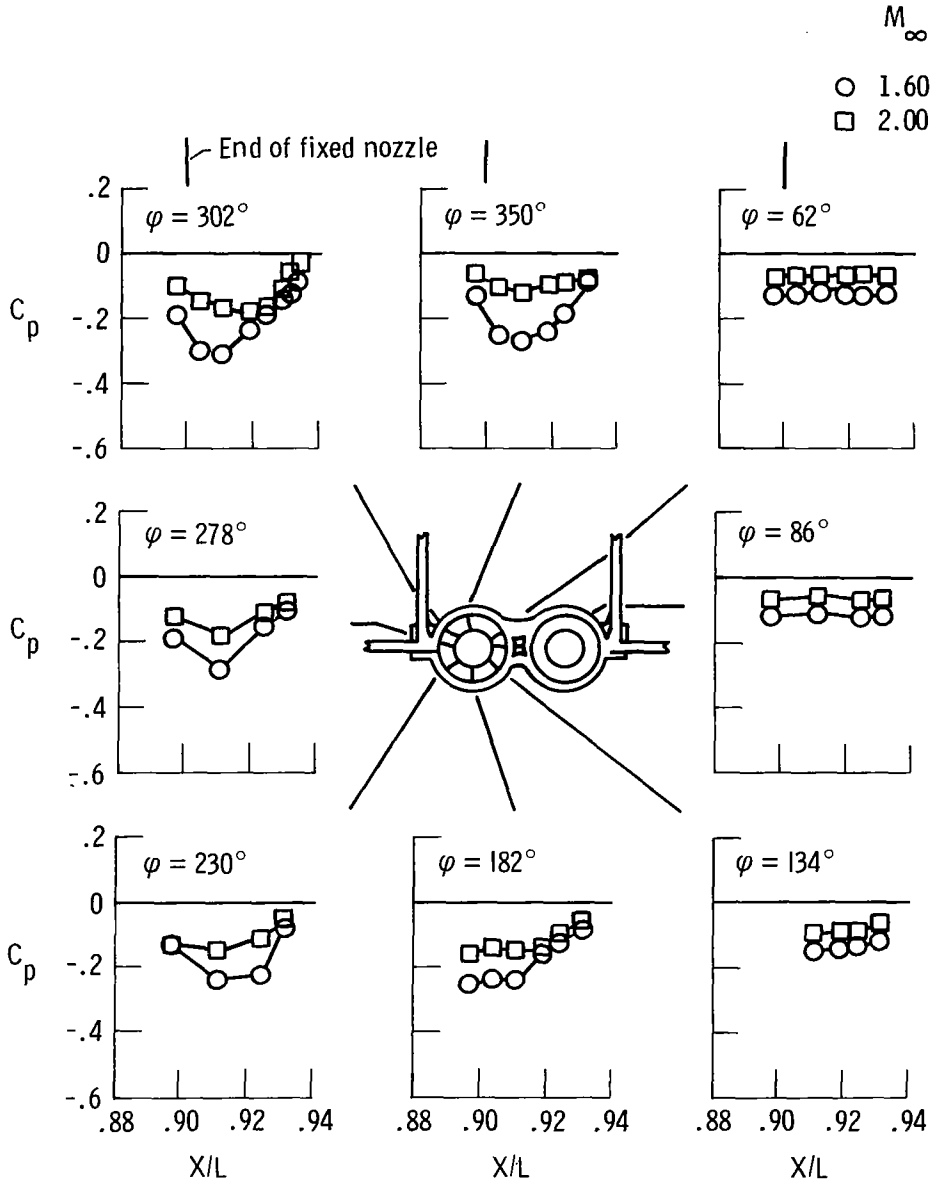

(f) M_∞ = 1.60 and 2.00.

Figure 33. Concluded.

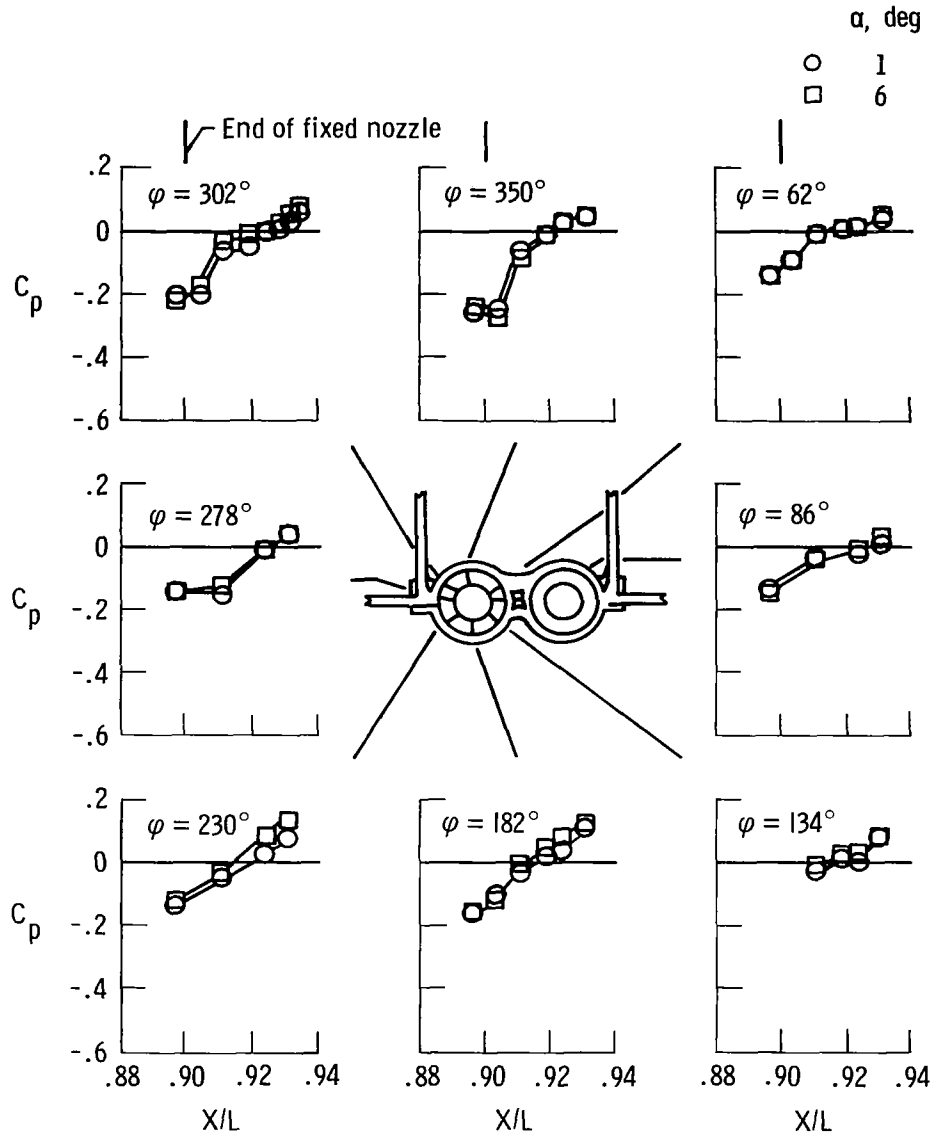

(a) Effect of angle of attack change from 1° to 6°. $M_\infty = 0.60$; BTL = MIL; BTR = MIL; $h_p = 10,500$ m; $\beta = 0°$.

Figure 34. Effect of angle of attack on left nozzle pressure coefficient. $\rho = 0°$; bypass door closed.

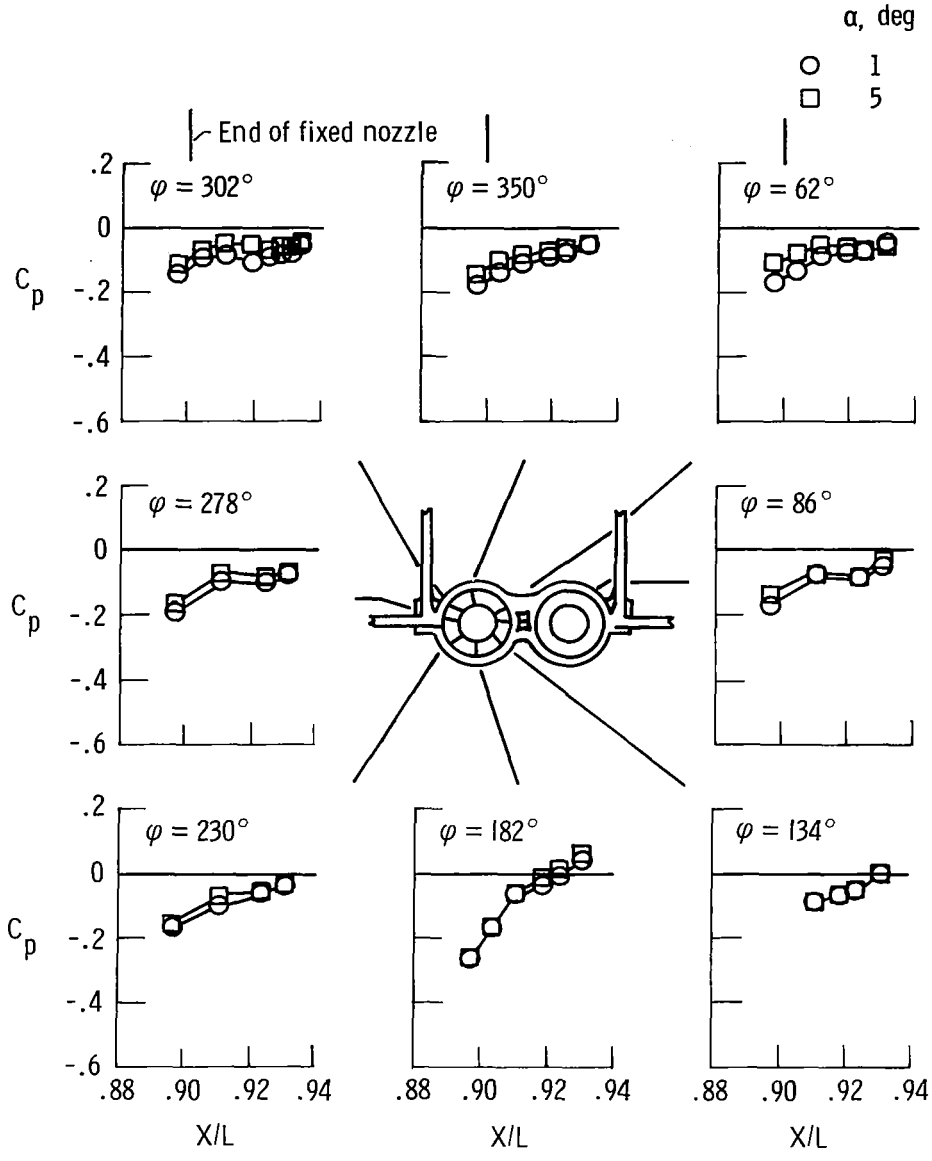

(b) Effect of angle of attack change from 1° to 5°. M_∞ = 0.90; BTL = MIL; BTR = MIL and 10.4°; h_p = 10,700 m; β = 0°.

Figure 34. Continued.

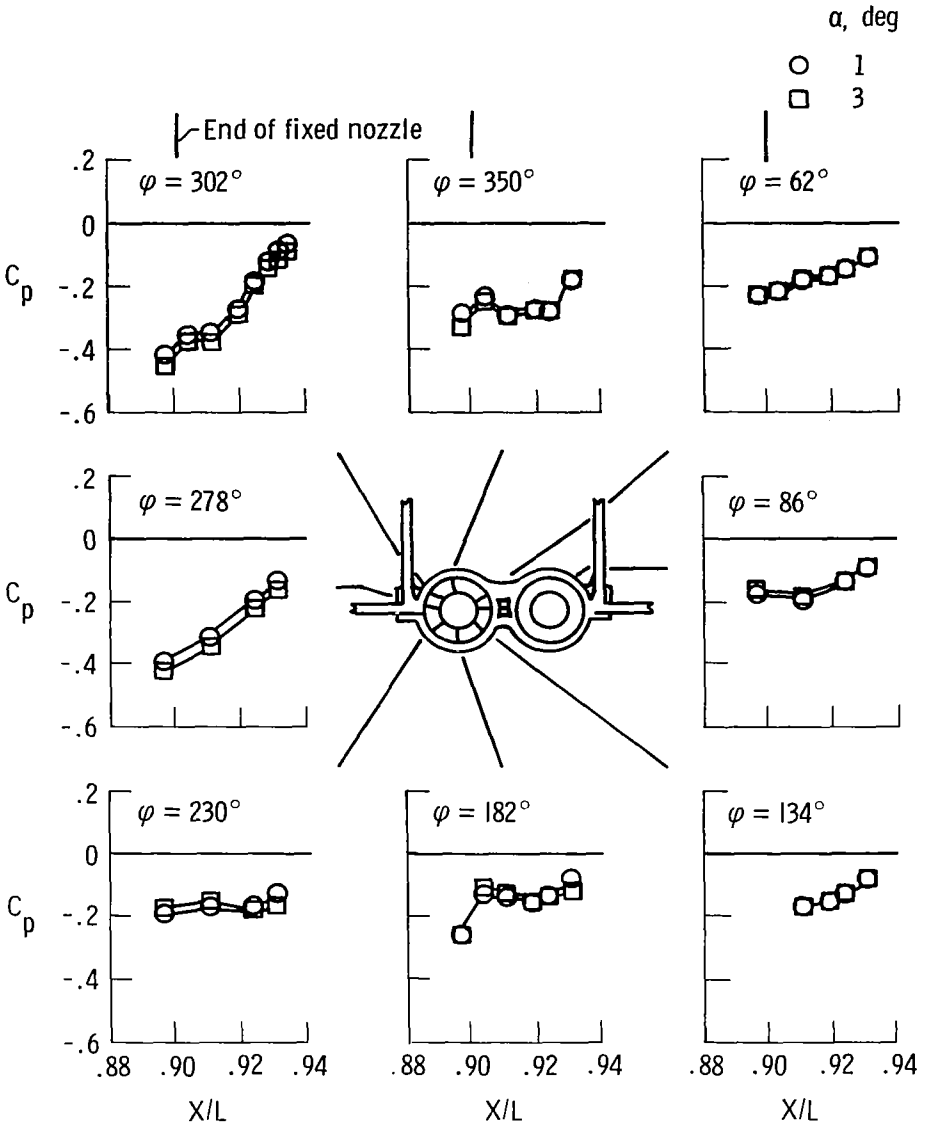

(c) Effect of angle of attack change from 1° to 3°. M_∞ = 1.20; BTL = 9.2°; BTR = 13.3°; h_p = 10,700 m; β = −0.3°.

Figure 34. Concluded.

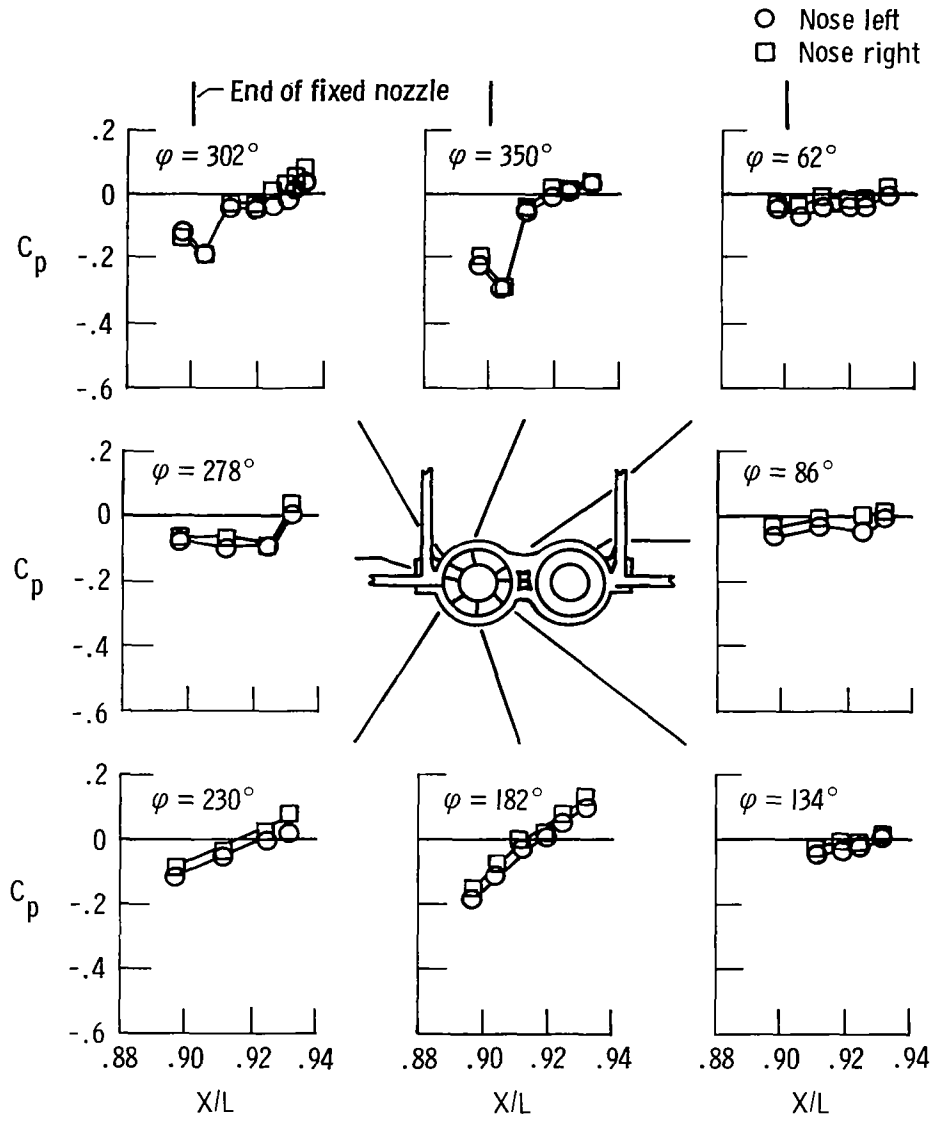

Figure 35. Effect of angle of sideslip change from 1° airplane nose left to 1° airplane nose right on left nozzle pressure coefficient. M_∞ *= 0.80; BTL = MIL; BTR = MIL;* h_p *= 13,800 m;* α *= 0.5°;* ρ *= 0°; bypass door closed.*

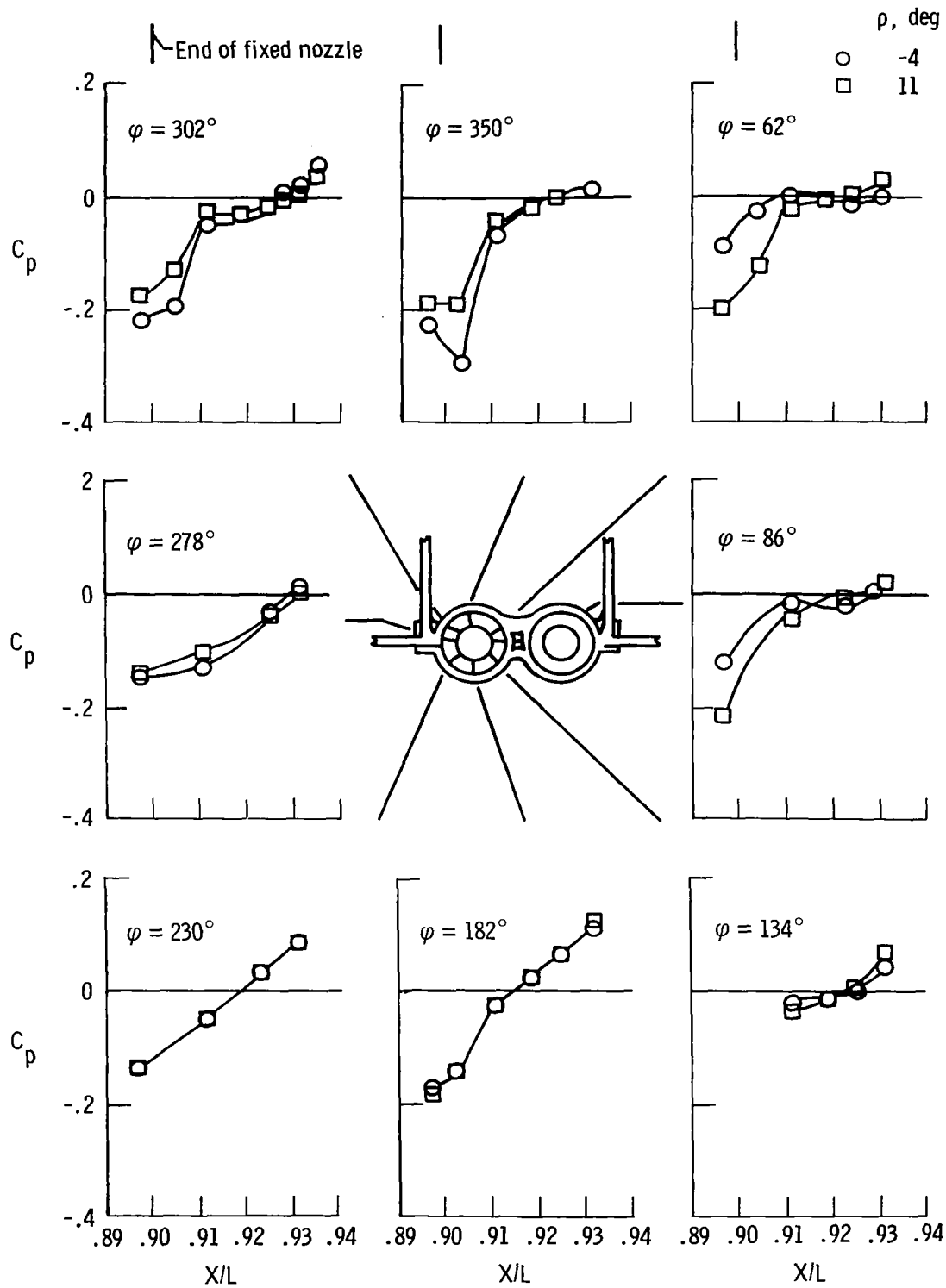

(a) M_∞ *= 0.59; BTL = MIL; BTR = MIL;* h_p *= 6300 m;* α *= 0.3°;* β *= −0.3°; bypass door closed.*

Figure 36. Effect of cowl angle change on left nozzle pressure coefficient.

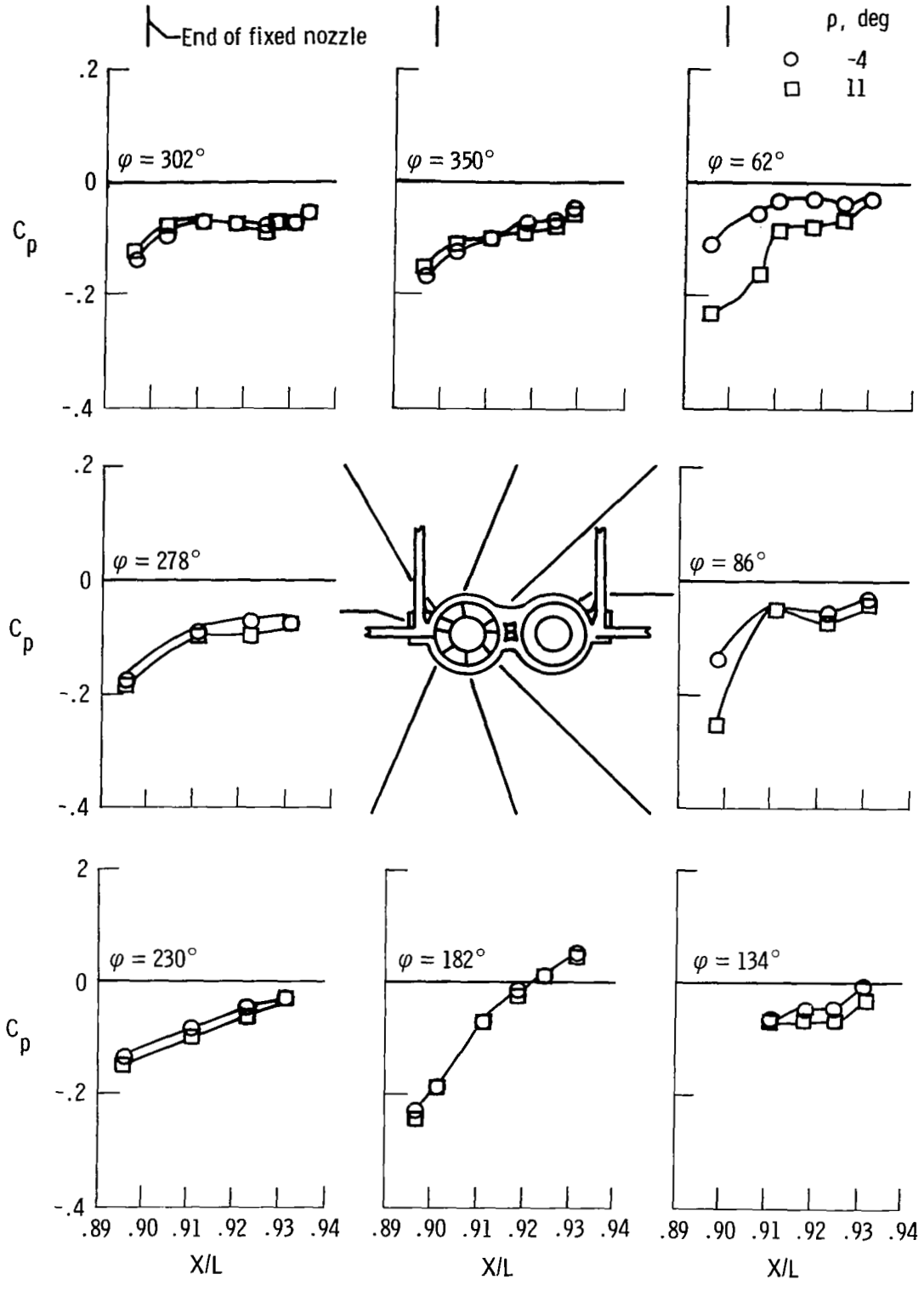

(b) $M_\infty = 0.89$; *BTL = MIL; BTR = MIL;* $h_p = 6400$ *m;* $\alpha = 1°$; $\beta = -0.3°$; *bypass door closed.*

Figure 36. Continued.

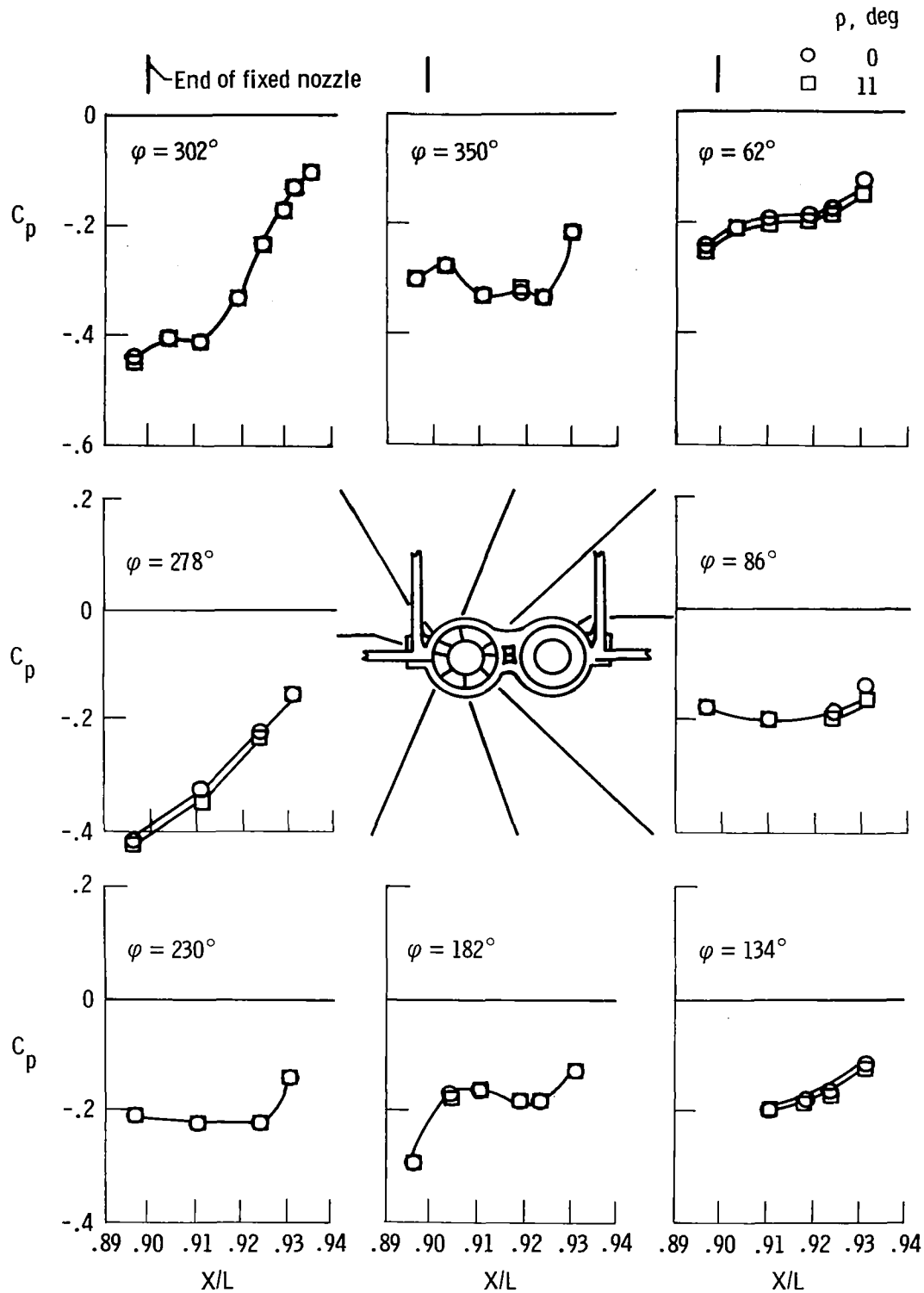

(c) M_∞ *= 1.20; BTL = 10.6°; BTR = 10.2°;* h_p *= 9300 m;* $\alpha \approx 1°$; $\beta = 0°$; *bypass door closed.*

Figure 36. Concluded.

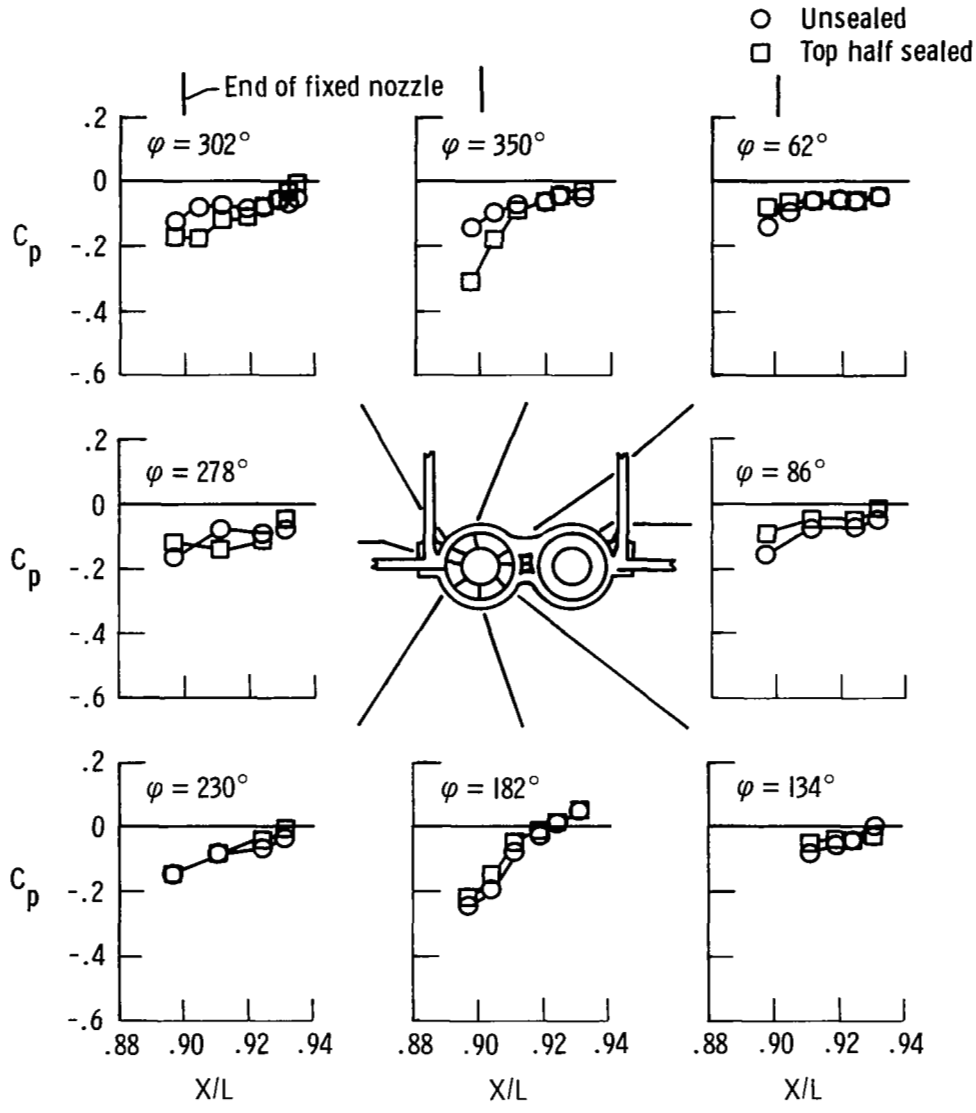

Figure 37. Effect of sealed and unsealed segmented flexible fairings on left nozzle pressure coefficient. $M_\infty = 0.90$; *BTL = MIL; BTR = MIL;* h_p *= 6000 m and 6400 m;* $\alpha = 1°$; $\beta = -0.2°$; $\rho = 0°$; *bypass door closed.*

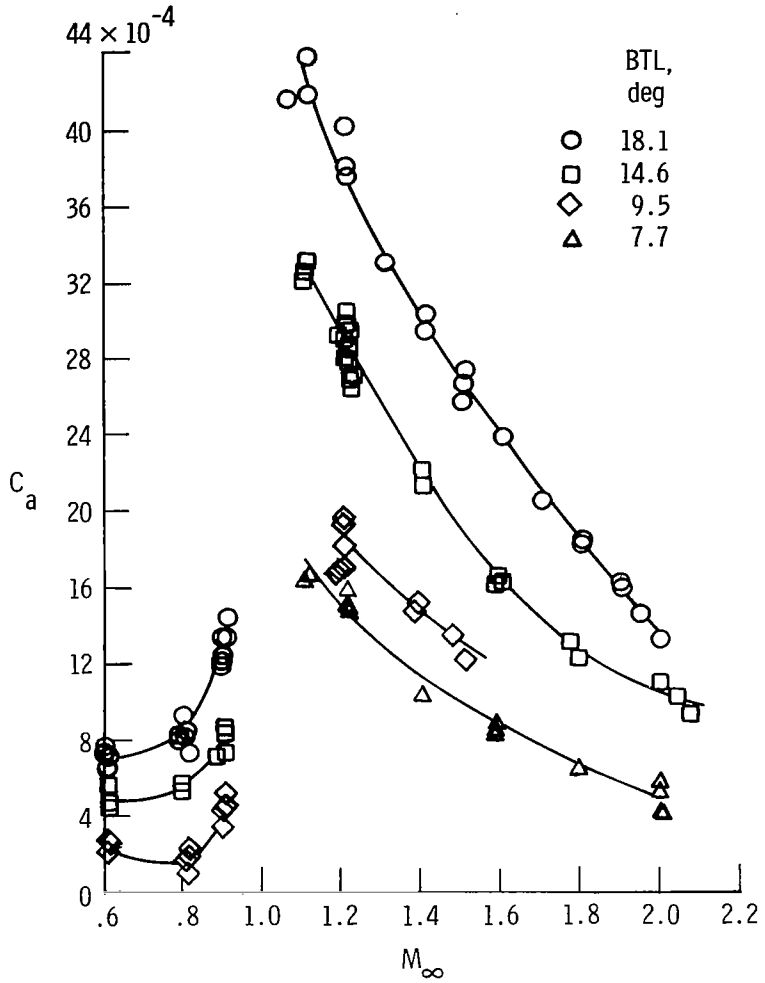

Figure 38. Variation of nozzle axial force coefficient with Mach number and left nozzle boattail angle. $0° < \alpha < 6°$; BTR = MIL to 2°.

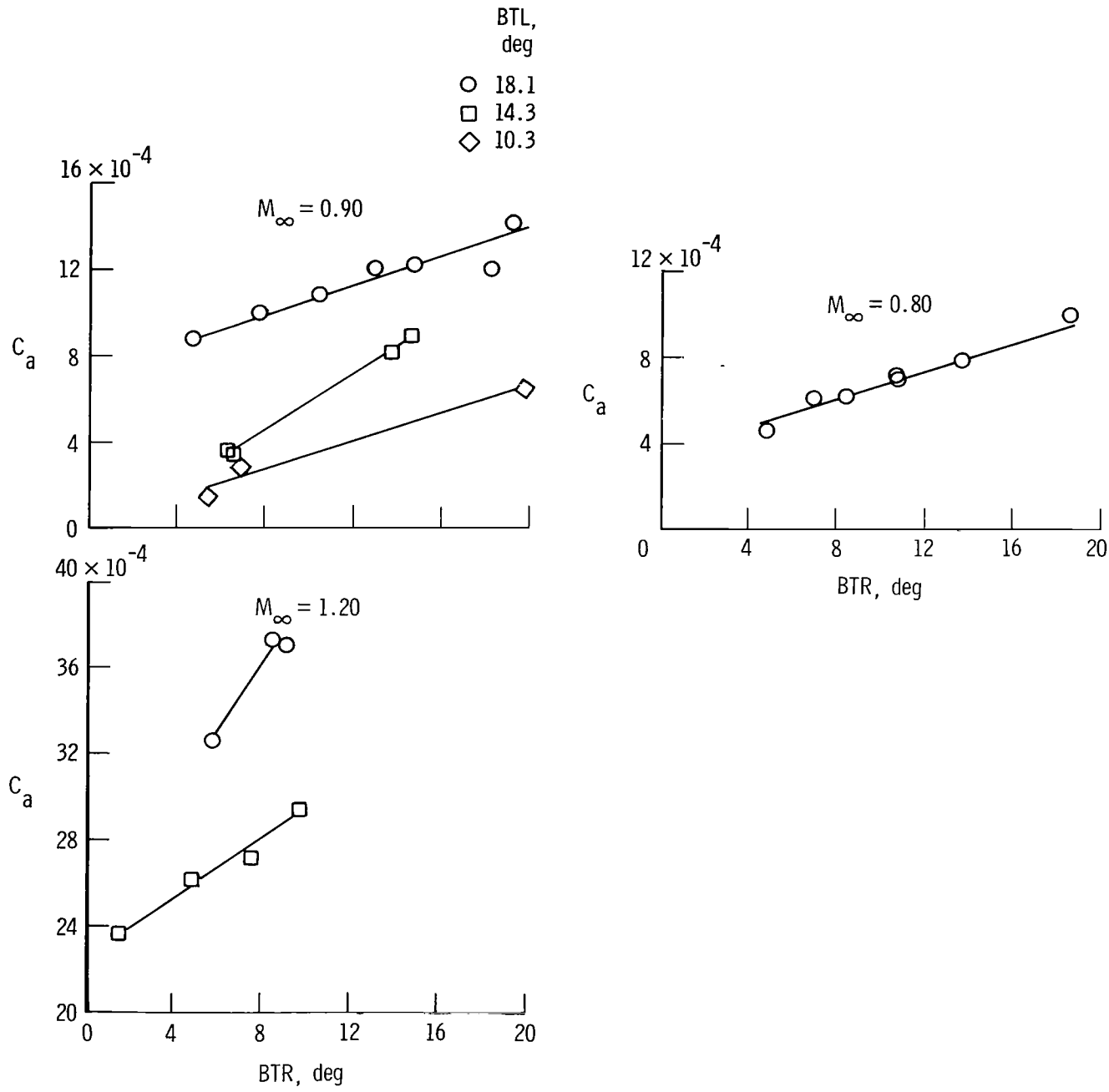

Figure 39. Effect of right nozzle boattail angle on left nozzle axial force coefficient. $h_p \approx$ 6100 m and 10,700 m; α = 1° to 7°.

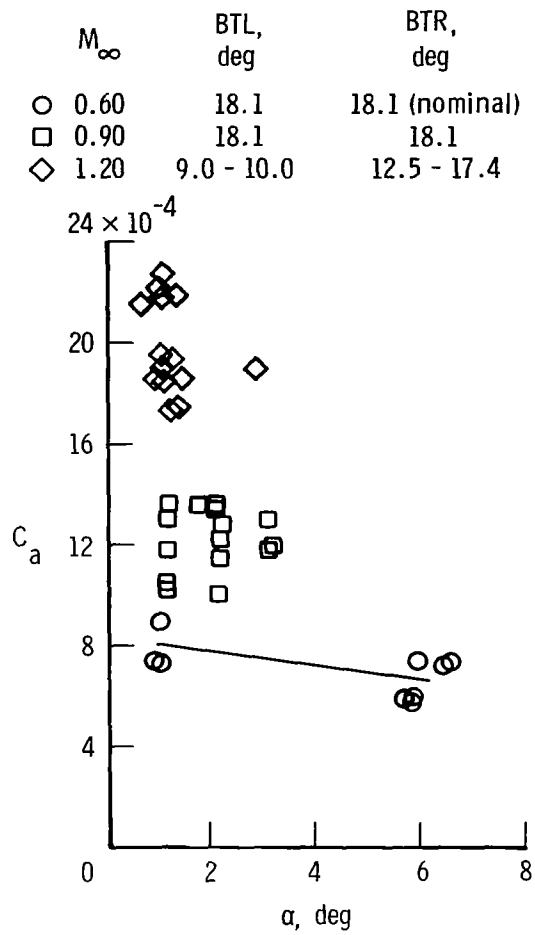

Figure 40. Effect of angle of attack on left nozzle axial force coefficient.

1. Report No. NASA TP-2017	2. Government Accession No.	3. Recipient's Catalog No.
4. Title and Subtitle PRESSURES MEASURED IN FLIGHT ON THE AFT FUSELAGE AND EXTERNAL NOZZLE OF A TWIN-JET FIGHTER		5. Report Date May 1983 6. Performing Organization Code RTOP 533-02-21
7. Author(s) Jack Nugent, Thomas J. Plant, Robert A. Davis, and Norman V. Taillon		8. Performing Organization Report No. H-1161 10. Work Unit No.
9. Performing Organization Name and Address NASA Ames Research Center Dryden Flight Research Facility P.O. Box 273 Edwards, CA 93523		11. Contract or Grant No. 13. Type of Report and Period Covered Technical Paper
12. Sponsoring Agency Name and Address National Aeronautics and Space Administration Washington, D.C. 20546		14. Sponsoring Agency Code

15. Supplementary Notes

16. Abstract

Fuselage, boundary layer, and nozzle pressures were measured in flight for a twin-jet fighter over a Mach number range from 0.60 to 2.00 at test altitudes of 6100, 10,700, and 13,700 meters for angles of attack ranging from 0° to 7°. Test data were analyzed to find the effects of the propulsion system geometry, the flight variables, and flow interference.

The aft fuselage flow field was complex and showed the influence of the vertical tail, nacelle contour, and the wing. Changes in the boattail angle of either engine affected upper fuselage and lower fuselage pressure coefficients upstream of the nozzle.

Boundary layer profiles at the forward and aft locations on the upper nacelles were relatively insensitive to Mach number and altitude. Boundary layer thickness decreased at both stations as angle of attack increased above 4°.

Nozzle pressure coefficient was influenced by the vertical tail, horizontal tail boom, and nozzle interfairing; the last two tended to separate flow over the top of the nozzle from flow over the bottom of the nozzle.

The left nozzle axial force coefficient was most affected by Mach number and left nozzle boattail angle. At Mach 0.90, the nozzle axial force coefficient was 0.0013.

17. Key Words (Suggested by Author(s))	18. Distribution Statement
Nozzle afterbody flow field Nozzle axial force Fuselage boundary layer	Unclassified—Unlimited STAR category 02

19. Security Classif. (of this report)	20. Security Classif. (of this page)	21. No. of Pages	22. Price*
Unclassified	Unclassified	90	A05

For sale by the National Technical Information Service, Springfield, Virginia 22161

NASA-Langley, 1983